INFORMATION TO USERS

This was produced from a copy of a document sent to us for microfilming. While the most advanced technological means to photograph and reproduce this document have been used, the quality is heavily dependent upon the quality of the material submitted.

The following explanation of techniques is provided to help you understand markings or notations which may appear on this reproduction.

1. The sign or "target" for pages apparently lacking from the document photographed is "Missing Page(s)". If it was possible to obtain the missing page(s) or section, they are spliced into the film along with adjacent pages. This may have necessitated cutting through an image and duplicating adjacent pages to assure you of complete continuity.
2. When an image on the film is obliterated with a round black mark it is an indication that the film inspector noticed either blurred copy because of movement during exposure, or duplicate copy. Unless we meant to delete copyrighted materials that should not have been filmed, you will find a good image of the page in the adjacent frame.
3. When a map, drawing or chart, etc., is part of the material being photographed the photographer has followed a definite method in "sectioning" the material. It is customary to begin filming at the upper left hand corner of a large sheet and to continue from left to right in equal sections with small overlaps. If necessary, sectioning is continued again—beginning below the first row and continuing on until complete.
4. For any illustrations that cannot be reproduced satisfactorily by xerography, photographic prints can be purchased at additional cost and tipped into your xerographic copy. Requests can be made to our Dissertations Customer Services Department.
5. Some pages in any document may have indistinct print. In all cases we have filmed the best available copy.

University
Microfilms
International

300 N. ZEEB ROAD, ANN ARBOR, MI 48106
18 BEDFORD ROW, LONDON WC1R 4EJ, ENGLAND

Reproduced with permission of the copyright owner. Further reproduction prohibited without permission.

7923777

WATERS, ROBERT GEORGE
EFFECTS OF UNIAXIAL STRESS ON EXCITONS IN
CUPROUS OXIDE.

CITY UNIVERSITY OF NEW YORK, PH.D., 1979

University
Microfilms
International 300 N. ZEEB ROAD, ANN ARBOR, MI 48106

PLEASE NOTE:

In all cases this material has been filmed in the best possible way from the available copy. Problems encountered with this document have been identified here with a check mark ✓.

1. Glossy photographs _______
2. Colored illustrations _______
3. Photographs with dark background _______
4. Illustrations are poor copy _______
5. Print shows through as there is text on both sides of page _______
6. Indistinct, broken or small print on several pages ✓ throughout _______
7. Tightly bound copy with print lost in spine _______
8. Computer printout pages with indistinct print _______
9. Page(s) _______ lacking when material received, and not available from school or author _______
10. Page(s) _______ seem to be missing in numbering only as text follows _______
11. Poor carbon copy _______
12. Not original copy, several pages with blurred type _______
13. Appendix pages are poor copy _______
14. Original copy with light type _______
15. Curling and wrinkled pages ✓
16. Other _______

University Microfilms International
300 N. ZEEB RD., ANN ARBOR, MI 48106 (313) 761-4700

EFFECTS OF UNIAXIAL STRESS ON EXCITONS IN CUPROUS OXIDE

by

ROBERT G. WATERS

A dissertation submitted to the Graduate Faculty in Physics in partial fulfillment of the requirements for the degree of Doctor of Philosophy, The City University of New York.

1979

This manuscript has been read and accepted for the Graduate Faculty in Physics in satisfaction of the dissertation requirement for the degree of Doctor of Philosophy.

18 May 1979
date

Chairman of Examining Committee

22 May 1979
date

Executive Officer

Joseph L Birman

Fred H Pollak

A C Damask

Supervisory Committee

The City University of New York

Abstract .

EFFECTS OF UNIAXIAL STRESS ON EXCITONS IN CUPROUS OXIDE

by

Robert G. Waters

Adviser: Professor Herman Z. Cummins

The effects of uniaxial stress on several exciton states in cuprous oxide have been studied. The experiments, which were performed using oriented single-crystal samples, utilized the resonant Raman scattering spectroscopic technique. This method identifies quadrupole-allowed (but dipole-forbidden) exciton states by the enhancement in the Raman cross-section for normally forbidden scattering from odd-parity phonons which occurs as a cw dye laser is frequency-tuned through such states.

Three S (L=0) exciton states and one D (L=2) state were studied using stresses of two different symmetries. The effect of the stress was to split the S states. While the D state experienced no splitting, a stress-induced shift was observed.

The results of the experiments have been analyzed and compared with theoretical predictions. The theory treats twelve S exciton states (for each principle quantum number) built from electrons in the lowest conduction band and holes in one or the other of the two highest, spin-orbit valence bands. On this theory, the interesting stress behavior for

exciton states of the yellow series in Cu_2O results from the coupling between the two spin-orbit split valence bands produced by the stress and by the electron-hole exchange interaction. The parameters which determine the stress behavior of exciton states in this treatment are: the magnitude of the spin-orbit splitting between the two valence bands already mentioned; the difference between the exciton Rydbergs for the yellow exciton series and the green series (deriving from the higher and lower valence bands, respectively); the electron-hole exchange integral; two or three deformation potentials depending on the direction of the stress. Comparison of the theory with the experimental data has resulted in several interesting conclusions which are enumerated below.

The important results of this research are now given.

1. The first piezooptic study of exciton states in Cu_2O in the absence of external perturbing fields has been conducted. The research, made possible through the use of resonant Raman scattering, has allowed the stress to act as the only perturbing effect extrinsic to the crystal and has permitted, through a polarization study, identification of the symmetries and degeneracies of stress-split exciton levels.

2. Nonlinearities in the energy shift of exciton levels as a function of stress have been observed for the first time, owing to the application of stress in excess of 2 Kbar.

3. A detailed analysis of the data has been made on the basis of an effective Hamiltonian formalism. This treatment has led to reasonable agreement between experiment and theory for the 1S state of the yellow series. The observed stress behavior of the excited exciton states, however, could not not be explained.

ACKNOWLEDGEMENTS

I am indebted to Professor Herman Z. Cummins for his guidance, support and encouragement throughout the course of this research.

I am grateful to Professor Fred H. Pollak for many hours of discussion and assistance.

I acknowledge the collaboration of Dr. R. H. Bruce, to whom I am very grateful for advice and assistance given over a period of many months.

I thank Professors J. L. Birman and R. Berenson and Dr. H.R. Trebin for many helpful discussions relating to the theory of excitons.

I am pleased to thank all members of the light scattering group at City College for their kind cooperation and assistance. A special debt is owed to Dr. M. Gorman, Mr. J. Wicksted and Mr. S. C. Hung.

I thank Dr. R. A. Forman, W. S. Brower and H. S. Parker for providing single crystals of Cu_2O and for many hours of instruction on the techniques of crystal growth specific to Cu_2O.

TO BARBARA

TABLE OF CONTENTS

LIST OF TABLES

LIST OF TABLES (Continued)

LIST OF FIGURES

LIST OF FIGURES (Continued)

CHAPTER I.

INTRODUCTION

The exciton spectrum of cuprous oxide has been studied extensively since the first observations by Hayashi and Katsuki[1]. The spectrum is characteristic of direct-forbidden-bandgap semiconductors in which P states are electric-dipole allowed and produce well-resolved absorption lines which can be observed in good crystals.

The S states are strictly dipole-forbidden and although the 1S state of the yellow series has been observed in weak electric-quadrupole absorption[7], the excited S states are normally too weak to be observed directly because of phonon-assisted transitions to the 1S state of the yellow excitons. D states are strongly forbidden. These higher, normally inaccessible states have been studied by means of symmetry-breaking perturbations which may render the states weakly dipole-allowed due to mixing with P states[23,28,30]. The mixing, however, has made interpretation difficult.

In recent years, it has become possible to investigate the excited states in the unperturbed Cu_2O crystal[41]. The technique, which requires a tunable laser, exploits the resonant Raman scattering that occurs from normally-forbidden odd-parity phonons when the laser is tuned to resonance with electric-dipole forbidden (but electric-quadrupole or magnetic-dipole allowed) states. It is thus possible to selectively detect S exciton states (and perhaps D states, if mixing is significant as will be discussed in Chapter III).

Several exciton level classification schemes have been proposed[23,30] but none of these are entirely satisfactory. The energy of the 2S state of the yellow exciton series, for example, has not been determined.

The assignments have been difficult to make for several reasons. In the first place effects such as the central cell correction and departure of energy bands from spherical symmetry can result in S-P splitting in the exciton series which, to a first approximation, is hydrogen-like. Also, in addition to the fundamental (yellow) exciton series, a second series (the green series) has been identified. The two series differ in that they involve hole states in two different (spin-orbit split) valence bands. The resultant splitting in the exciton series is roughly equal to the binding energy of the 1S state of the green exciton series so that its possible occurence in the same energy region as the excited yellow states cannot be ignored.

The present research was motivated in part by the prospect of resolving some of the assignment difficulties that exist. The resonant Raman scattering associated with several exciton states has been reexamined for crystals subjected to uniaxial stress. The magnitude and multiplicity of the splitting of exciton levels and the symmetry of the split levels which result from the lowered crystal symmetry have provided a wealth of experimental information.

The experiments described herein represent the first comprehensive study of the excited states of the yellow exciton using uniaxial stress and resonant Raman scattering simultaneously. In contrast to previous stress work[15,40], the use of the present technique has allowed symmetry assignment of the stress-split states. In addition, it has been possible, for the first time, to apply stress of sufficient magnitude to produce nonlinear stress dependence of the energy levels.

CHAPTER II

Cu_2O: PROPERTIES AND EXPERIMENTAL SURVEY

A. Properties

Cuprous oxide crystallizes in the cuprite structure which belongs to the O_h^4 space group[63]. As shown in Fig.2-1, the unit cell contains six ions, two of which are oxygen ions O^{--} arranged in a body-centered configuration and four of which are copper ions Cu^+ at the corners of a regular tetrahedron centered on the central oxygen ion. The lattice parameter $|\vec{a}|$ is 4.27Å. The O^{--} and Cu^+ ions have site symmetries T_d and D_{3d}, respectively.

The symmetries of normal modes in the long wavelength limit as well as the symmetries of electronic levels at the zone-center can be determined by neglecting the translations and considering only the symmetry operations of the macroscopic point group O_h. This group is the direct product of O, the group of proper rotations which take a cube into itself, and I, the inversion group. The effects of spin are described by the crystal double group which may be generated from the crystal point group. The results of group theory presented in this chapter will be stated without proof. Detailed analysis will be reserved for Chapter III.

B. Normal Vibrational Modes

A group-theoretical analysis using the O_h character table predicts Brillouin zone-center vibrational modes with the following symmetries: $3\Gamma_4^- + \Gamma_5^- + \Gamma_3^- + \Gamma_2^- + \Gamma_5^+$. One

Γ_4^- representation accounts for all three acoustic modes and the other two are infrared-active optic modes (since they transform like a vector). The triply degenerate Γ_5^+ mode is the only mode that transforms like the polarizability tensor and is thus the only Raman active mode. In centrosymmetric crystals, such as Cu_2O, a mode may be either Raman or infrared-active but not both. The other optic modes, a triply degenerate Γ_5^- mode, a doubly degenerate Γ_3^- mode, and a nondegenerate Γ_2^- mode, are all Raman and infrared-inactive but are of central importance to the theory of resonant-Raman scattering in Cu_2O. The frequencies of the normal modes have been measured experimentally by infrared absorption[64], phonon-assisted absorption[9], photoluminescence[65], neutron scattering[66], and Raman scattering[21,67]. The results of the Raman scattering experiments are shown in Table 2-1.

C. Energy Bands

The presently accepted band symmetries at the center of the Brillouin zone of the two highest valence bands and the two lowest conduction bands are shown in Fig. 2-2. The lowest conduction band has symmetry Γ_1^+ being formed from combinations of Cu 4S and/or O 3S orbitals. The highest valence band derives from Cu 3D wavefunctions and has Γ_5^+ symmetry. With spin-orbit coupling the symmetry of the Γ_1^+ conduction band becomes Γ_6^+ and the Γ_5^+ highest valence band is split into Γ_7^+ and Γ_8^+ bands with the Γ_7^+ lying higher in energy. An electron in the Γ_6^+ conduction band and a hole in the Γ_7^+ valence band combine to form the yellow exciton series (the hydrogen-like energy levels of the Coulomb-bound electron-hole system). The S states have overall symmetry ${}^2\Gamma_7^+ \otimes {}^2\Gamma_6^+ = {}^3\Gamma_5^+ + {}^1\Gamma_2^+$. These states are the triply degenerate orthoexciton and the singlet paraexciton. Optical transitions to the singlet are strictly forbidden while transitions to the triplet are electric quadrupole (but not dipole) allowed. A hole in the Γ_8^+ valence band and an electron in the Γ_6^+ conduction band form the green exciton series. In this case the S states have symmetry ${}^4\Gamma_8^+ \otimes {}^2\Gamma_6^+ = {}^2\Gamma_3^+ + {}^3\Gamma_4^+ + {}^3\Gamma_5^+$. Transitions to these states are also parity (electric-dipole) forbidden; however the ${}^3\Gamma_4^+$ triplet has magnetic dipole symmetry (and is thus magnetic-dipole allowed) while the ${}^2\Gamma_3^+$ and ${}^3\Gamma_5^+$ components are electric-quadrupole allowed.

The band symmetries shown in Fig. 2-2 are due to Elliott[9] who used symmetry arguments based on the anisotropy of optical absorption near the quadrupole 1S state of the yellow exciton series[7]. Analysis of magnetoabsorption data[16] and the consistency of experiments with calculated normal mode frequencies[69] based on this model have substantiated the Elliott proposal.

D. Exciton Series

The excitons formed in Cu_2O are probably the best-known examples of Wannier excitons. Grossman[2], Nikitine[12,17], and Elliott[14] have written excellent review articles on the subject.

FIG. 2-1. Unit cell of Cu_2O

Structure: cuprite (cubic)

Space Group: O_h^4

Lattice Parameter: $|\tilde{a}| = 4.27$ Å

Ions		Positions	Site Symmetries
2 Oxygen	●	$(0,0,0)a$	T_d
		$\frac{1}{2}(1,1,1)a$	
4 Copper	○	$\frac{1}{4}(1,1,1)a$	D_{3d}
		$\frac{1}{4}(3,3,1)a$	
		$\frac{1}{4}(1,3,3)a$	
		$\frac{1}{4}(3,1,3)a$	

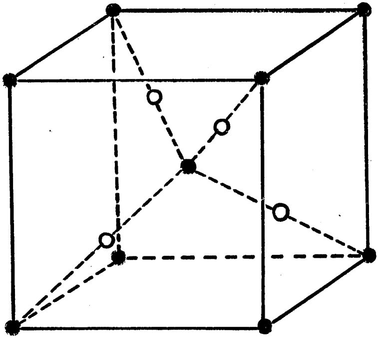

TABLE 2-1. Phonon energies (cm^{-1}) of Cu_2O

Phonon	Energy
Γ_5^-	88
Γ_3^-	109
Γ_4^- (TO)	152
Γ_4^- (LO)	154.5
Γ_2^-	350
Γ_5^+	515
Γ_4^- (TO)	630
Γ_4^- (LO)	660

FIG. 2-2. The presently accepted symmetry assignments of the two highest valence bands and the two lowest conduction bands of Cu_2O at the Brillouin zone center. Symmetry assignments to the right include spin-orbit coupling (except for the deep Γ_4^- valence band). In the first column the atomic orbitals responsible for the bands are shown. The band energies in wavenumbers are shown on the right. Interaction between an electron in a conduction band and a hole in a valence band gives rise to several exciton series as indicated in the figure.

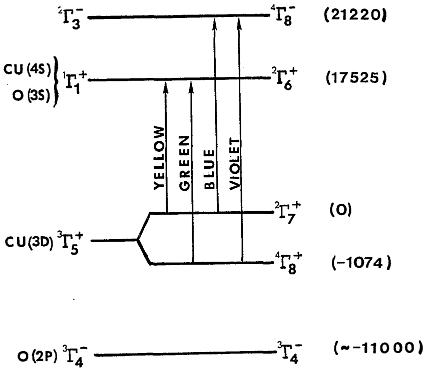

$^2\Gamma_3^-$
$^4\Gamma_8^-$
(21220)
CU (4S)
O (3S)
$^1\Gamma_1^+$
$^2\Gamma_6^+$
(17525)
YELLOW
GREEN
BLUE
VIOLET
$^2\Gamma_7^+$
(0)
CU(3D) $^3\Gamma_5^+$
$^4\Gamma_8^+$
(-1074)
O(2P) $^3\Gamma_4^-$
$^3\Gamma_4^-$
(~-11000)

Early absorption experiments[1-5,7,12] revealed fine structure which could be associated with exciton formation[6]. The absorption spectrum in the visible region is shown in Fig. 2-3. Transitions associated with the fundamental gap are dipole-forbidden since the relevant bands all have even parity. The related exciton states derived from electrons in the Γ_6^+ conduction band and a hole in the Γ_7^+ (yellow series) or Γ_8^+ (green series) band, have long lifetimes giving rise to narrow spectral lines.

The intensity of optical absorption to exciton states also depends upon the angular momentum of relative electron-hole motion. Elliott[6] has shown that P states of the yellow and green exciton series are weakly dipole-allowed due to finite wavevector effects. S states, however, are strictly dipole forbidden. Absorption lines due to the P states of the yellow and green exciton series are labelled Y and G in Fig. 2-3, respectively. The spectra are hydrogen-like and the energies of the P states are described quite well by the Rydberg formulae[2]

$$E^Y_{np} = 17523 - \frac{795}{n^2} \qquad \text{Yellow}$$

$$E^G_{np} = 18588 - \frac{1242}{n^2} \qquad \text{Green} \qquad (2\text{-}1)$$

where n can take on any integral value greater than one. The energies are in wavenumbers.

The 1S state of the yellow series is seen as a weak electric-quadrupole absorption feature. The quadrupole nature of the line was established by Gross and Kaplyanskii in 1960[7]. The 1S line is shown in Fig. 2-3. The absorption edges near the 1S are due to phonon-assisted absorption involving the Γ_3^- (109 cm^{-1}) phonon. Excited S and D states are not normally observed as they are masked by phonon-assisted absorption to the 1S state.

A weak absorption line has been observed about 200 cm^{-1} to the low energy side of the 2P state of the yellow series[19]. Diess et.al.[19] have attributed it to transitions to the 1S state of the green exciton series. This assignment, based on the ($\Gamma_3^+ + \Gamma_4^+$) symmetry of the absorption has been questioned by Denisov and Makarov[31] who argue that the 1S green state also comprises an exchange-split component of Γ_5^+ symmetry which should produce a strong absorption line in view of calculated oscillator strengths.

The excited S and D states of the yellow series have been studied using the electroabsorption technique wherein an applied electric field imparts some weak dipole character to these normally-forbidden states due to mixing with P exciton states. The experiments have been done by workers in Leningrad[30] and in Strasbourg[20,22,23,28,29]. The assignments of the excited states are due to the Strasbourg group and are shown in Fig. 2-4.

The S states that have been studied using electroabsorption are the ${}^3\Gamma_5^+$ triplet states. Each triplet is accompanied by an exchange-split ${}^1\Gamma_2^+$ singlet level, optical transitions to which are forbidden in both the electric dipole and electric quadrupole approximations.

FIG. 2-3. Absorption spectrum of Cu_2O in the visible region showing exciton fine structure. (After Ref. 2)

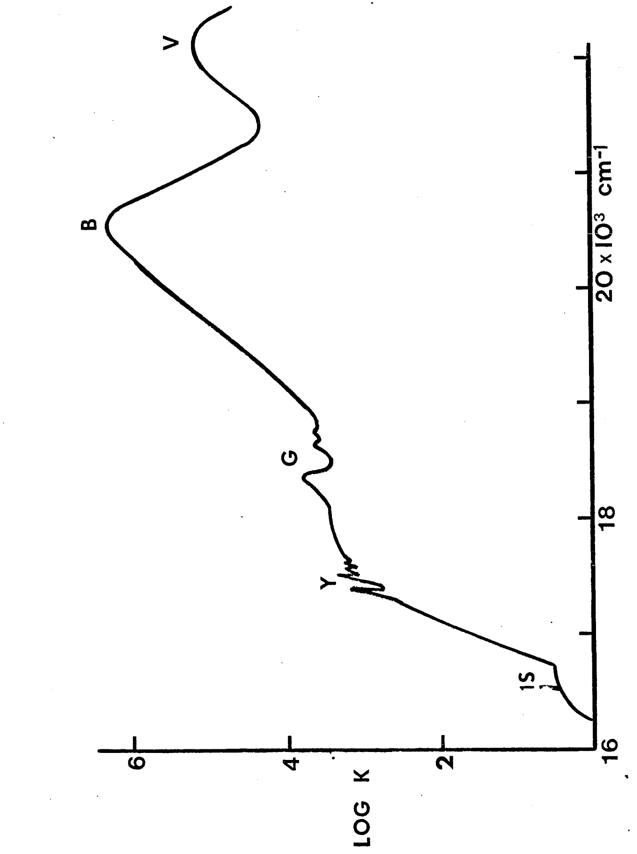
LOG K
6
4
2
16
18
20 x 10³ cm⁻¹
1S
Y
G
B
V

Several recent experiments have placed the 1S singlet approximately 100 cm^{-1} below the 1S triplet[38,39,43,70]. In these experiments, transitions to the singlet became less strongly-forbidden as a result of applied stress or magnetic field perturbations.

In 1973, Compaan and Cummins[27] observed intense Raman scattering from normally Raman-forbidden odd-parity phonons when the incident laser frequency was tuned to resonance with the 1S (triplet) state of the yellow exciton series. This resonant quadrupole-dipole Raman scattering process[26,32] differs from normal (dipole-dipole) Raman scattering in several respects. In the first place, it involves a dipole forbidden transition. Secondly, the odd-parity phonons that participate are normally Raman-forbidden in centrosymmetric crystals. Finally, the Raman cross section depends on the frequency of the incident light, there being an enhancement in the cross-section as the laser is scanned through quadrupole (but not dipole) exciton states. The effect has been exploited as a quadrupole spectrometer in a series of experiments in which a dye laser was scanned through the spectral range of the yellow excited states[41,67]. Resonant enhancement in the Raman cross-section (for non polar phonons) was observed when the incident laser light was resonant with states of ${}^3\Gamma_5^+$ symmetry (triplet S states and the states previously labelled D, and thought to be the ${}^3\Gamma_5^+$ component of exciton D states). The resonant Raman scattering spectroscopy allowed the excited exciton states to be studied for the first time in the unperturbed Cu_2O crystal.

E. Stress Experiments

Uniaxial stress measurements have played an important role in the study of excitons in Cu_2O. In the early 1960's, Gross and Kaplyanskii[8,10] observed a stress-splitting of the 1S yellow state. The results underlined the influence of the exchange interaction on the stress-splitting of exciton states built from simple Kramers doublets (which themselves cannot be split by a uniform stress). Splittings of multiplicity 2,3, and 2 were observed for tetragonal, rhombohedral and trigonal stress, respectively. The applied stress in these experiments did not exceed 1 Kbar and the splittings were observed to be linear in the stress.

Several years later, Agekyan, Gross and Kaplyanskii[15] observed a stress-splitting of some weak absorption features. Although the weakness of the absorption precluded detailed analysis, one feature was reported to exhibit the same multiplicities as the 1S state.

In 1974, Agekyan and Stepanov[40] again investigated the stress-splitting of excited S states, but with the addition of a static electric field. The observed dependence of the stress-splitting on principal quantum number led them to question the accepted energy level assignments and to propose a new classification scheme for the yellow exciton states. However, they were unable to establish the symmetries of the stress-split excited states because of the admixture of P states produced by the electric field.

FIG. 2-4. Energy level diagram of the yellow exciton series of Cu_2O. Energies of the 1S and all P exciton states are from Ref. 67. Other exciton energies are from Refs. 23 and 28. Numbers in parentheses are estimated widths.

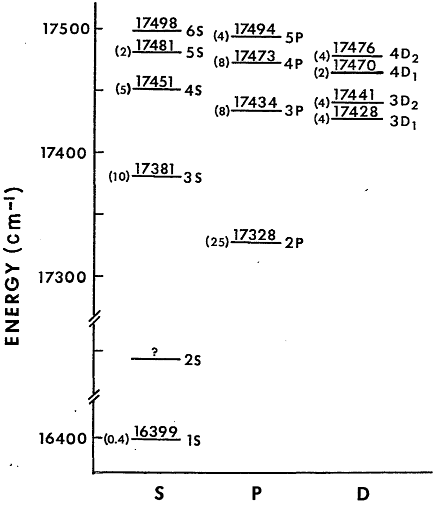
ENERGY (cm⁻¹)
17500
17400
17300
16400
17498 6S
(2) 17481 5S
(5) 17451 4S
(10) 17381 3S
? 2S
(0.4) 16399 1S
(4) 17494 5P
(8) 17473 4P
(8) 17434 3P
(25) 17328 2P
(4) 17476 4D2
(2) 17470 4D1
(4) 17441 3D2
(4) 17428 3D1
S
P
D

In the chapters that follow, the results of forbidden resonant Raman scattering spectroscopy of Cu_2O subjected to uniaxial stress will be presented. Splittings of several exciton states have been measured for stresses of two different symmetries. It has been possible to apply stress in excess of 2 Kbar. The resulting nonlinear stress dependence had not been observed previously. In addition, the symmetries of the stress-split components has been established.

CHAPTER III

THEORY

A. Introduction

This chapter contains reviews of Raman scattering and exciton theory as well as a treatment of the effects of uniaxial stress on exciton spectra. Sections B and C review exciton theory and Raman scattering respectively. In Section D, the results of the previous two sections are applied to the Cu_2O exciton spectrum. A discussion of past optical work is presented. In Section F the effects of stress on the one-electron bands and on the exciton spectrum are discussed. In Section G, calculations specific to the exciton spectrum of Cu_2O are presented.

B. Exciton Theory

1. Exciton Wave Function[14]

In the one-electron approximation, each electron is assumed to move in an average potential V due to the other electrons and the atomic cores. The electronic wavefunctions are solutions of

$$\left(p^2/2m + V \right) \Psi = E \Psi \tag{3-1}$$

and in consequence of the translational symmetry of the lattice have the Bloch form

$$\Psi_{n\vec{k}}(\vec{r}) = \frac{1}{\sqrt{NB}}\, u_{n\vec{k}}(\vec{r})\, e^{i\vec{k}\cdot\vec{r}} \tag{3-2}$$

where n is the band index, $\vec{k}$ is the wavevector, N is the number of cells and B is the volume of each cell. The Bloch functions $u_{n\vec{k}}$ have the periodicity of the lattice. The ground state wavefunction with the valence band completely filled and the conduction band empty can be written as

$$\Psi_0 = \frac{1}{\sqrt{N}} P\, \psi_{v\vec{k}_1}(\vec{r}_1)\cdots\cdots\psi_{v\vec{k}_j}(\vec{r}_j)\cdots\cdots\psi_{v\vec{k}_N}(\vec{r}_N) \tag{3-3}$$

where P denotes the antisymmetric combination. An excited state, one that has one electron taken from a valence band and placed in a conduction band is given by

$$\Psi_0 = \frac{1}{\sqrt{N}} P\, \psi_{v\vec{k}_1}(\vec{r}_1)\cdots\psi_{c\vec{k}_{j'}}(\vec{r}_{j'})\cdots\psi_{v\vec{k}_N}(\vec{r}_N) \tag{3-4}$$

or, using the concept of a hole state, by

$$\Psi = \psi_{c\vec{k}_e}(\vec{r}_e)\, \psi_{v\vec{k}_h}(\vec{r}_h) \tag{3-5}$$

where $\psi_{c\vec{k}_e}(\vec{r}_e)$ represents the electron in the conduction band and $\psi_{v\vec{k}_h}(\vec{r}_h)$ represents the antisymmetrized product of the remaining one-electron states in the valence band.

The wavefunctions $\psi_{n\vec{k}}$ at a specific value of $\vec{k}$ for all n form a complete set. Substitution of Eq. (3-2) into Eq. (3-1) gives the result that near $\vec{k}=0$

$$u_{n\vec{k}} = u_{n0} + \sum_{n'\neq n} u_{n'0}\, \frac{\hbar\vec{k}}{m}\, \frac{\langle n'|\vec{p}|n\rangle}{E_n - E_{n'}} \tag{3-6}$$

At small finite $\vec{k}$, therefore, the wavefunctions may be written as a linear combination of the wavefunctions from all bands at $\vec{k}=0$.

An exciton is a bound electron-hole pair in which the binding arises from an effective Coulomb interaction

$$U = \frac{-e^2}{\epsilon|\vec{r}_e - \vec{r}_h|} \qquad (3\text{-}7)$$

where ϵ is the dielectric constant. The exciton wavefunction can be written as a linear combination of the unperturbed one-electron pair states (3-5) in the presence of the perturbation Eq. (3-7):

$$\psi_{ex} = \sum_{\vec{k}_e \vec{k}_h} A(\vec{k}_e, \vec{k}_h)\, \psi_{c\vec{k}_e}(\vec{r}_e)\, \psi_{v\vec{k}_h}(\vec{r}_h) \qquad (3\text{-}8)$$

An alternate wavefunction for the exciton may be obtained through the effective mass approximation. Let $\phi(\vec{r}_e, \vec{r}_h)$ represent the motion of the electron and hole on a large scale compared with atomic dimensions. $\phi(\vec{r}_e, \vec{r}_h)$ satisfies the equation of the effective mass approximation

$$\left[E_c(-i\nabla_e) - E_v(-i\nabla_h) - \frac{e}{\epsilon r}\right]\phi(\vec{r}_e, \vec{r}_h) = E\,\phi(\vec{r}_e, \vec{r}_h) \qquad (3\text{-}9)$$

and is related to the coefficients $A(\vec{k}_e, \vec{k}_h)$ of Eq. (3-8) by

$$\phi(\vec{r}_e, \vec{r}_h) = \frac{1}{NB} \sum_{\vec{k}_e, \vec{k}_h} A(\vec{k}_e, \vec{k}_h)\, e^{i\vec{k}_e \cdot \vec{r}_e}\, e^{i\vec{k}_h \cdot \vec{r}_h} \qquad (3\text{-}10)$$

Near $\vec{k}_e, \vec{k}_h = 0$ we have

$$\psi_{ex} = \phi(\vec{r}_e, \vec{r}_h)\, u_{co}(\vec{r}_e)\, u_{vo}(\vec{r}_h) \qquad (3\text{-}11)$$

For spherical conduction and valence bands near $\vec{k}=0$, Eq. (3-9) reduces to the hydrogen atom equation and

$$\phi(\vec{r}_e,\vec{r}_h) = \frac{1}{\sqrt{NB}} \varphi(\vec{r}_e-\vec{r}_h)\, e^{i\vec{K}\cdot\vec{\rho}}$$

(3-12)

where $\hbar\vec{K} = \hbar(\vec{K}_e+\vec{K}_h)$ is the total exciton momentum, $(\vec{r}_e-\vec{r}_h)$ is the relative coordinate of the electron and hole, $\varphi(\vec{r}_e-\vec{r}_h)$ is the exciton envelope function of relative motion, and the exciton center of mass coordinate is given by

$$\vec{\rho} = \frac{m_e\vec{r}_e + m_h\vec{r}_h}{m_e+m_h}$$

(3-13)

where m_e and m_h are the effective masses of the electron and hole, respectively.

2. Exciton Spectrum[6,14]

In the effective mass approximation, Eq. (3-9) has hydrogenlike solutions and a hydrogenlike spectrum of energy eigenvalues

$$E = E_g + \frac{\hbar^2 K^2}{2(m_e+m_h)} - \frac{R}{n^2}$$

(3-14)

where E_g is the band gap energy and

$$R = \frac{\mu e^4}{2\hbar^2\epsilon^2}$$

(3-15)

is the exciton Rydberg. The exciton reduced mass is given by

$$\frac{1}{\mu} = \frac{1}{m_e} + \frac{1}{m_h}$$

(3-16)

The second term in Eq. (3-14) is the kinetic energy of the center-of-mass motion and is responsible for an exciton band for each type of relative electron-hole motion.

3. Electron-Hole Exchange Interaction[14,60,61]

An important effect heretofore ignored is the so-called electron-hole exchange interaction. Although the electron and hole are not identical particles, an exchange interaction arises from exchange between identical electrons in the multiparticle problem and may be formally treated as electron-hole exchange.

Consider two arbitrary exciton states (see Eq. (3-8)) specified by their total wavevector and their quantum numbers. For simplicity assume that each state involves only two bands and that the two states considered share a common conduction band but derive from different valence bands with indices n and m. The eigenstates are

$$|\lambda, \vec{K}\rangle = \sum_{\vec{q}} A_{\lambda \vec{K}}(m, \vec{q})\, U_{\vec{K}+\vec{q}}\, V_{m,-\vec{q}}$$
$$|\nu, \vec{K}\rangle = \sum_{\vec{q}} A_{\nu \vec{K}}(n, \vec{q})\, U_{\vec{K}+\vec{q}}\, V_{n,-\vec{q}} \qquad (3\text{-}17)$$

Here the Bloch functions are

$$U_{\vec{K}+\vec{q}} = e^{i(\vec{K}+\vec{q})\cdot\vec{r}}\, u_{\vec{K}+\vec{q}}(\vec{r})$$
$$V_{m,-\vec{q}} = e^{-i\vec{q}\cdot\vec{r}}\, v_{-\vec{q}}(\vec{r}) \qquad (3\text{-}18)$$

and the summations are over electron-hole relative wavevector. The exchange part of the Coulomb matrix element between the two exciton states can be written

$$J_{ex_{\lambda\nu}} = e^2 \sum_{\vec{q}\vec{q}'} A_{\lambda\vec{K}}(m,\vec{q})\, A_{\nu\vec{K}}(n,\vec{q}')$$

$$\times \iint d\tau_1\, d\tau_2 \frac{e^{i\vec{K}\cdot(\vec{r}_2-\vec{r}_1)}}{|\vec{r}_1-\vec{r}_2|} u^*_{\vec{K}+\vec{q}}(\vec{r}_1) V_{m,-\vec{q}}(\vec{r}_1) u_{\vec{K}+\vec{q}'}(\vec{r}_2) V^*_{n,-\vec{q}'}(\vec{r}_2)$$

$$= \sum_{\vec{R}} e^{i\vec{K}\cdot\vec{R}} \iint_{\text{CELL}} dr_1\, dr_2 \frac{\rho_{\lambda o}(\vec{r}_1)\rho_{\nu o}(\vec{r}_2)}{|\vec{r}_1-\vec{r}_2-\vec{R}|} \qquad (3\text{-}19)$$

where $\vec{R}$ is a lattice vector. The quantity

$$\rho_{\nu\vec{K}}(\vec{r}) = \frac{e}{\sqrt{N}} \sum_{\vec{q}'} A_{\nu\vec{K}}(n,\vec{q}') \sum u_{\vec{K}+\vec{q}}(\vec{r}) V^*_{m,-\vec{q}}(\vec{r}) \qquad (3\text{-}20)$$

is called the spin singlet charge density. One can often neglect the $\vec{K}$-dependence of the Bloch functions so that

$$\rho_{\mu o}(\vec{r}) = -e\, \phi_{\mu o}(m,o) \sum_{\text{SPINS}} u(\vec{r}) V_m(\vec{r})^* \qquad (3\text{-}21)$$

where

$$\phi_{\mu\vec{R}}(m,\vec{R}) = \frac{1}{\sqrt{N}} \sum_{\vec{q}} A_{\mu\vec{K}}(m,\vec{q})\, e^{i\vec{q}\cdot\vec{R}} \qquad (3\text{-}22)$$

i.e. the exciton envelope function in analogy with Eq. (3-10). The exchange integral becomes

$$J_{ex_{\lambda\nu}} = \frac{e^2}{N} \sum_{\vec{R}} e^{i\vec{K}\cdot\vec{R}} \phi_{\lambda o}(m,0)\phi_{\nu o}(n,0) \iint_{\text{CELL}} dr_1\, dr_2\, u^*(\vec{r}_1) V_m(\vec{r}_1) u(r_2) V_n^*(\vec{r}_2) \qquad (3\text{-}23)$$

The exchange interaction can be divided into a short-range (or analytic) part and a long-range (nonanalytic) part[60]. For dipole-inactive excitons such as those relevant to this research, only the short-range part is important. It is given by the $\vec{R} = 0$ term in Eq. (3-23) so that the final expression becomes

$$J_{ex_{\lambda\nu}} = \frac{e^2}{N} \phi^*_{\lambda o}(m,o)\, \phi_{\nu c}(n,o) \iint \frac{d\vec{r}_1\, d\vec{r}_2\, u^*(\vec{r}_1) v_m(\vec{r}_1) u(\vec{r}_2) v_n^*(\vec{r}_2)}{|\vec{r}_1 - \vec{r}_2|} \tag{3-24}$$

The $\phi_{\mu o}(m,o)$ are nonvanishing only for S states of electron-hole relative motion.

The discussion of the exchange interaction will be taken up again in Section G.

4. Optical Transitions[6,14]

The probability for optical transitions between the ground state and an exciton state is proportional to

$$|\langle \Psi_{ex} | H_{ER} | \Psi_o \rangle|^2 \tag{3-25}$$

where the electron-radiation interaction H_{ER} is given by

$$H_{ER} = \sum_j A_o \hat{e}_\lambda \cdot \vec{p}_j e^{i\vec{k}_\lambda \cdot \vec{r}_j} = \sum_j A_o (\hat{e}_\lambda \cdot \vec{p}_j + i\vec{k}_\lambda \cdot \vec{r}_j\, \hat{e}_\lambda \cdot \vec{p}_j + \cdots) \tag{3-26}$$

The first term in the expansion is the usual electric dipole term. The second term can be resolved into electric quadrupole and magnetic dipole terms. A_o is the amplitude of the external vector potential of the field, $\vec{k}$ is the wavevector for incident or scattered light, and $\vec{r}_j$ and $\vec{p}_j$ are the position and momentum vectors for the j^{th} electron. $\hat{e}_\lambda$ is the unit polarization vector of the electromagnetic field. The two leading terms in the expansion lead to four possible matrix elements of Eq. (3-25).

a. Strongly-Allowed Dipole Transitions

Using the dipole term of H_{ER} in Eq. (3-25) with exciton representation Eq. (3-8) leads to

$$\langle \Psi_{ex} | H_{ER}^{ED} | \Psi_0 \rangle \propto \sum_{\vec{K}_e \vec{K}_h} A(\vec{K}_e, \vec{K}_h) \langle c, \vec{K}_e + \vec{K}_\lambda | \hat{e}_\lambda \cdot \vec{p}_j | v, -\vec{K}_h \rangle \tag{3-27}$$

For a strongly-allowed dipole transition, the matrix element $\langle c | \hat{e}_\lambda \cdot \vec{p} | v \rangle$ exists at the center of the Brillouin zone and may be taken out of the summation giving

$$\langle \Psi_{ex} | H_{ER}^{ED} | \Psi_0 \rangle \propto \langle u_{co} | \hat{e}_\lambda \cdot \vec{p} | u_{vo} \rangle \, \phi(0) \tag{3-28}$$

where $\langle u_{co} | \hat{e}_\lambda \cdot \vec{p} | u_{vo} \rangle$ is the zone center matrix element. For the case of spherical bands with extrema at $\vec{k}=0$ where ϕ has the hydrogenic form we have (with $\vec{r}_e - \vec{r}_h = 0$)

$$\phi(0) = \frac{1}{\sqrt{NB}} \frac{1}{\sqrt{\pi a^3 n^3}} \tag{3-29}$$

for S states of electron-hole relative motion and zero otherwise. Thus strongly-allowed dipole transitions from the ground state will occur only to S exciton states with a transition probability falling off as n^{-3}. These are the direct allowed transitions occurring at direct allowed bandgaps.

b. Weakly-Allowed Dipole Transitions

It may happen that the matrix element in Eq. (3-28) vanishes at the zone center because the valence and conduction bands have the same parity or for other symmetry reasons. This is not sufficient to preclude dipole transitions. The dipole matrix elements need not vanish since the electron and hole states of finite wavevector included in the overall exciton wavefunction Eq. (3-8) contains admixtures of other Bloch functions as shown in Eq. (3-6). Using Eqs. (3-6) and (3-27) we obtain a matrix element for a weakly-allowed dipole transition:

$$\langle \Psi_{eX} | H_{ER}^{ED} | \Psi_0 \rangle \propto \left| \sum_i \frac{\langle c|\vec{p}|i\rangle\langle i|\hat{e}_\lambda\cdot\vec{p}|v\rangle}{E_c - E_i} + \frac{\langle c|e_\lambda\cdot p|i\rangle\langle i|\vec{p}|v\rangle}{E_v - E_i} \right| \cdot \nabla\phi(0) \qquad (3\text{-}30)$$

For the hydrogenic case,

$$\nabla\phi(0) = \left(\frac{n^2-1}{\pi a^5 n^5}\right)^{1/2} \qquad (3\text{-}31)$$

for P states only and zero otherwise. Thus, there will be weakly-allowed dipole transitions from the ground state to P exciton states with a probability which falls off with increasing n. These are the direct forbidden transitions.

c. Electric Quadrupole and Magnetic Dipole Transitions

The second term in the expansion for H_{ER} can be decomposed into electric quadrupole and magnetic dipole terms:[26,32]

$$\vec{k}_\lambda \cdot \vec{r}\,\hat{e}_\lambda \cdot \vec{p} = \frac{1}{2}\vec{k}_\lambda \cdot (\vec{r}\vec{p} + \vec{p}\vec{r}) \cdot \hat{e}_\lambda + \frac{1}{2}(\vec{k}_\lambda \times \hat{e}_\lambda) \cdot (\vec{r} \times \vec{p}) \qquad (3\text{-}32)$$

These terms lead to electric quadrupole and magnetic dipole transitions:

$$\langle \Psi_{ex} | H_{ER}^{EQ} | \Psi_0 \rangle \propto \sum_{\vec{k}_e \vec{k}_h} i A(\vec{k}_e, \vec{k}_h) \langle c, \vec{k}_e + \vec{k}_\lambda | \vec{k}_\lambda \cdot (\vec{r}\vec{p} + \vec{p}\vec{r}) \cdot \hat{e}_\lambda | v, -\vec{k}_h \rangle \tag{3-33}$$

$$\langle \Psi_{ex} | H_{ER}^{MD} | \Psi_0 \rangle \propto \sum_{\vec{k}_e \vec{k}_h} i A(\vec{k}_e, \vec{k}_h) \langle c, \vec{k}_e + \vec{k}_\lambda | (\vec{k}_\lambda \times \hat{e}_\lambda) \cdot (\vec{r} \times \vec{p}) | v, -\vec{k}_h \rangle \tag{3-34}$$

If these matrix elements are allowed at the zone center, we obtain

$$\langle \Psi_{ex} | H_{ER}^{EQ} | \Psi_0 \rangle \propto \langle u_{c0} | \vec{k}_\lambda \cdot (\vec{r}\vec{p} + \vec{p}\vec{r}) \cdot \hat{e}_\lambda | u_{v0} \rangle \phi(0) \tag{3-35}$$

$$\langle \Psi_{ex} | H_{ER}^{MD} | \Psi_0 \rangle \propto \langle u_{c0} | (\vec{k}_\lambda \times \hat{e}_\lambda) \cdot (\vec{r} \times \vec{p}) | u_{v0} \rangle \phi(0) \tag{3-36}$$

Just as for strongly-allowed dipole transitions, Eqs. (3-35) and (3-36) give non-zero values only for S states.

5. Exciton-Lattice Interaction

A non-polar phonon produces a disturbance of the lattice which perturbs the periodic potential acting on the electrons and leads to an exciton-lattice interaction energy which is known as the deformation potential. For a phonon of wavevector q on branch j, the deformation potential interaction is given by

$$H_{EL} = D_j^e(\vec{r}_e) e^{i\vec{q}_j \cdot \vec{r}_e} + D_j^h(\vec{r}_h) e^{i\vec{q}_j \cdot \vec{r}_h} \tag{3-37}$$

where the electron and hole functions $D_j^e(\vec{r}_e)$ and $D_j^h(\vec{r}_h)$ have the symmetry of the phonon.

The dominant matrix elements of Eq. (3-37) involve an interband transition of either the electron or the hole. Thus, for an electron transition using Eq. (3-11) we obtain

$$\langle \Psi'_{ex} | H_{EL} | \Psi_{ex} \rangle = \delta(\vec{K}+\vec{q}-\vec{K}') \iint |u_{vo}(\vec{r}_h)|^2 \phi'(\vec{r}_e-\vec{r}_h) u'_{co}(\vec{r}_e)$$

$$\times D_j^e(\vec{r}_e) e^{i\vec{q}\cdot(\vec{r}_e-\vec{\rho})} u_{cc}(\vec{r}_e) d\vec{r}_e d\vec{r}_h d(\vec{r}_e-\vec{r}_h) \qquad (3\text{-}38)$$

Retaining only the leading term in $e^{i\vec{q}\cdot(\vec{r}_e-\vec{\rho})}$ and adding contributions from both electron and hole give

$$\langle \Psi'_{ex} | H_{EL} | \Psi_{ex} \rangle \propto \delta(\vec{K}+\vec{q}-\vec{K}')[\langle u'_{cc} | D_j^e(\vec{r}_e) | u_{co} \rangle \delta_{vv'} + \langle u'_{vo} | D_j^h(\vec{r}_h) u_{vc} \rangle \delta_{cc'}]$$

$$\times \iint \phi'(\vec{r}_e-\vec{r}_h) \phi(\vec{r}_e-\vec{r}_h) d(\vec{r}_e-\vec{r}_h) \qquad (3\text{-}39)$$

which is the product of the zone center interband matrix element of $D_j^e(\vec{r}_e)$ or $D_j^h(\vec{r}_h)$ multiplied by an overlap integral of the exciton envelope functions.[46]

C. Raman Scattering

The Raman effect has been an important source of information for studies of lattice dynamics since its first observations by Raman[47] and by Landsberg and Mandelshtam[48]. Light of frequency ω_i interacts with the crystal to create or destroy one or more lattice vibrational phonons having energy $\hbar\omega_o$. Energy conservation requires that the frequencies of the incident and scattered light and the phonon be related by

$$\omega_s = \omega_i \pm \omega_o \qquad (3\text{-}40)$$

Before a scattering event, it is assumed that the crystal is in the ground electronic state with all valence bands full and all conduction bands empty, and that it returns to the ground state after each scattering event. The electron-radiation and electron-lattice interactions H_{ER} and H_{EL} mediate transitions between eigenstates of the crystal. In all electronic virtual intermediate states, there is an electron in a conduction band and a hole in a valence band.

One possible Raman process involves absorption of a photon with frequency ω_i, wavevector $\vec{k}_i$, and unit polarization vector $\hat{e}_i$ which excites the crystal from the electronic ground state $|i\rangle$ to a virtual intermediate state $|a\rangle$ via the electron-radiation interaction. With the crystal in this state, a phonon of wavevector $\vec{q}$ and frequency ω_o is either created (Stokes) or destroyed (anti-Stokes) by the electron-lattice interaction. The system thereby undergoes a transition to another intermediate state $|b\rangle$. The system then returns to the final state $|f\rangle$ through emission of a photon with frequency $\omega_s=\omega_i \pm \omega_o$, wavevector $\vec{k}_s=\vec{k}_i-\vec{q}$ and polarization vector $\hat{e}_s$. As will be discussed, of the several Raman processes that can occur the above one is dominant near resonance.

The scattering probability per unit time for the first-order Raman (Stokes) process is given in third-order time-dependent perturbation theory by[49]

$$W=\frac{2\pi}{\hbar^6}\sum_{\vec{q},k_s}\sum_{a,b}\left|\frac{\langle f|H_I|b\rangle\langle b|H_I|a\rangle\langle a|H_I|i\rangle}{(\omega_s-\omega_b)(\omega_i-\omega_a)}\right|\delta(\omega_i-\omega_s-\omega_o) \qquad (3\text{-}41)$$

Here $\vec{k}_s$ is the wavevector of the scattered photon, $\vec{q}=\vec{k}_i-\vec{k}_s$

is the phonon wavevector and δ is the Dirac delta function. In two of the H_I matrix elements, the electron-radiation interaction contributes while the electron-lattice interaction contributes to the remaining one. These may occur in any time order, and by permuting the order in which they occur, the following expression for the first-order Raman scattering intensity may be obtained:

$$I(\omega_i,\omega_s,\omega_o) \propto \sum_{\vec{q}\,\vec{k}_s} \frac{(n+1)}{\omega_i\omega_s\omega_o} \left|\hat{\xi}_{o\vec{q}}\, P(-\omega_i,+\omega_s,+\omega_o)\right|^2 \delta(\vec{k}_i-\vec{k}_s-\vec{q})\,\delta(\omega_i-\omega_s-\omega_o) \tag{3-42}$$

where n is the number of optic phonons, $\hat{\xi}_{o\vec{q}}$ is the phonon polarization vector and $P(-\omega_i,+\omega_s,+\omega_o)$ has the form

$$\begin{aligned} P(-\omega_i,+\omega_s,+\omega_o) = \sum_{ab} \Bigg\{ & \frac{\langle f|H_{ER}(\omega_s)|b\rangle\langle b|H_{EL}|a\rangle\langle a|H_{ER}(\omega_i)|i\rangle}{(\omega_b+\omega_o-\omega_i)(\omega_a-\omega_i)} \\ & + \frac{\langle f|H_{ER}(\omega_i)|b\rangle\langle b|H_{EL}|a\rangle\langle a|H_{ER}(\omega_s)|i\rangle}{(\omega_b+\omega_o+\omega_s)(\omega_a+\omega_s)} \\ & + \frac{\langle f|H_{EL}|b\rangle\langle b|H_{ER}(\omega_s)|a\rangle\langle a|H_{ER}(\omega_i)|i\rangle}{(\omega_b+\omega_s-\omega_i)(\omega_a-\omega_i)} \\ & + \frac{\langle f|H_{ER}(\omega_s)|b\rangle\langle b|H_{ER}(\omega_i)|a\rangle\langle a|H_{EL}|i\rangle}{(\omega_b+\omega_o-\omega_i)(\omega_a+\omega_o)} \\ & + \frac{\langle f|H_{EL}|b\rangle\langle b|H_{ER}(\omega_i)|a\rangle\langle a|H_{ER}(\omega_s)|i\rangle}{(\omega_b+\omega_s-\omega_i)(\omega_a+\omega_s)} \\ & + \frac{\langle f|H_{ER}(\omega_i)|b\rangle\langle b|H_{ER}(\omega_s)|a\rangle\langle a|H_{EL}|i\rangle}{(\omega_b+\omega_o+\omega_s)(\omega_a+\omega_o)} \Bigg\} \end{aligned} \tag{3-43}$$

This is known as the Raman scattering tensor. The sign convention is such that P $(-\omega_i+\omega_s,+\omega_o)$ represents a Stokes process while P $(+\omega_i,-\omega_s,-\omega_o)$ represents an anti-Stokes process.

The intensity of Raman-scattered light generally depends upon the polarization of the incident and scattered light. This may be expressed in terms of the Raman scattering tensor given by Eq. (3-43). The unit polarization vector of the incident light is denoted $\hat{e}_i$, with Cartesian components $e_{i\beta}$. Similarly, the Cartesian components of the scattered light are denoted $e_{s\alpha}$. In the usual dipole approximation for H_{ER}, the intensity of first-order scattered light polarized in the direction α for incident light polarized in the direction β is given by

$$I \propto | e_{s\alpha} P_{\alpha\beta} e_{i\beta} |^2 \qquad (3\text{-}44)$$

The Raman tensor elements may be found using group theoretical arguments and have been tabulated by Loudon.[50]

The above discussion applies to normal Raman scattering in which both electron-radiation interaction matrix elements in each term of Eq. (3-43) are taken in the dipole approximation. Among its consequences is the requirement that the participating phonons have even parity (in centrosymmetric crystals). In addition, the scattering intensity is independent of the wavevector of the incident light.

If it happens that one of the dipole matrix elements in Eq. (3-43) vanishes, but the matrix element involving the quadrupole term, $\langle | i\vec{k}_\lambda \cdot \vec{r}\hat{e}_\lambda \cdot \vec{p} | \rangle$, fails to vanish, Raman scattering can proceed via the multipole-dipole mechanism.[26,32] Scattering due to this mechanism is usually not observed since its intensity is reduced from normal Raman scattering by a factor of $\sim 10^{-3}$. However, when the energy of the incident or scattered light equals the energy of an electronic state of the crystal (e.g. an exciton state), a resonance enhancement of the intensity may be observed due to very small energy denominators in Eq. (3-43). (Damping terms, representing the finite widths of the states involved, have not been included in the equation). The first term in Eq. (3-43) gives the strongest contribution to scattering near resonance, and the other terms are nearly independent of frequency over this range. The process described above is forbidden resonant Raman scattering. Symmetry-breaking Raman scattering can occur at resonance due to finite wavevector effects of the photon or phonon.

In centrosymmetric crystals the operator $H_{ER}^{EQ}(H_{ER}^{ED})$ has even (odd) parity. Therefore, H_{EL} must have odd parity in order to participate in the electric quadrupole-electric dipole (or magnetic dipole-electric dipole)process. This is complementary to ordinary Raman scattering in which only even parity phonons are allowed. Specifically, the representation to which the phonon belongs must be contained in the reduction of the representation of the direct product $\Gamma(H_{ER}^{ED}) \otimes \Gamma(H_{ER}^{EQ}) = \Gamma_2^- + \Gamma_3^- + \Gamma_4^- + \Gamma_5^-$. In Cu_2O, this includes all of the odd-parity phonons.

Another feature which distinguishes the multipole-dipole mechanism from ordinary dipole-dipole Raman scattering is its dependence on the wavevector of the photon that couples to the multipole state.

The scattering intensity for the multipole-dipole process may be expressed in terms of the third-rank scattering tensor $P_{\alpha\beta\gamma}(j\sigma)$ which has been derived and tabulated by Birman.[26,32] This tensor describes scattering processes involving a phonon of polarization σ belonging to the j^{th} irreducible representation. The subscripted indices refer to the unit vectors for the incident polarization (β) the scattered polarization (α) and the wavevector of the incident light (γ). In terms of the third-rank scattering tensor, the scattering intensity becomes

$$I(j) = C \sum_{\sigma} \Big| \sum_{\alpha\beta\gamma} e_{s\alpha} P_{\alpha\beta\gamma}(j\sigma)\, e_{i\beta}\, k_{i\gamma} \Big|^2 \qquad (3\text{-}45)$$

It should be mentioned that there are other mechanisms that may give rise to forbidden resonant Raman scattering. These involve the Frohlich electron-lattice interaction which is specific to LO phonons and is therefore not relevant to the present research involving non-polar phonons.

D. Resonant Raman Scattering and Excitons in Cu_2O

In this section we discuss the exciton spectrum of Cu_2O and the associated transitions within the framework of the preceding theoretical introduction.

Fig. 1-3 shows the presently accepted band scheme.

The yellow and green exciton series are formed by transitions between bands that have the same parity.[9] Dipole transitions between these bands are, therefore, forbidden at zone center. However, because the band wavefunctions at finite wavevector contain admixtures of wavefunctions of other bands, weakly-allowed dipole transitions are permitted between the ground state and the P states of the yellow and green series. At zone center a quadrupole-allowed transition between bands having symmetry Γ_7^+ and Γ_6^+ forms the yellow exciton states with S envelopes. The P-state features and the 1S feature are shown in the absorption curve of Fig. 1-2. Higher S states are masked by phonon-assisted transitions to the 1S.

The quadrupole nature of the 1S state was discovered by Gross and Kaplyanskii[8] and provided the basis for Elliott's band assignments.[9]

Optical studies of the yellow exciton series performed during the intervening years were reviewed in Chapter 2. The more recent resonant Raman scattering studies require further discussion.

Yu, Shen, Petroff and Falicov have extensively studied allowed multiphonon Raman scattering in the region of the yellow exciton series of Cu_2O and have reported the resonant enhancement of a number of multiphonon Raman features.[73-76] The strongest resonant enhancement in this region occurs for the $2\Gamma_3^-$ process. Resonant enhancement was also observed for several other two-phonon, three-phonon and four-phonon processes all of which involved a Γ_3^- mode.

In a series of experiments[27,36,41] Cummins, Compaan and coworkers used a dye laser to tune through the frequency range of yellow exciton states. Raman scattering intensity for all of the odd-parity phonons in Cu_2O exhibited a dramatic resonant enhancement whenever the laser was tuned to an S or D_1 yellow exciton state. Scattering with the laser tuned to these states, which are the subject of the present study, was shown to be consistent with the quadrupole-dipole Raman-scattering mechanism described in section C. Polarization ratios were found to be in agreement with the third-rank scattering tensors derived by Birman. A schematic of this process is shown in Fig. 3-1.

The experiments described above established the resonant Raman scattering technique as a quadrupole spectrometer since there is a strong enhancement of the Raman cross-section as the laser is tuned through quadrupole (but not dipole) exciton states. In particular, the technique identifies states of Γ_5^+ symmetry.

As discussed in Chapter 2 assignments of excited yellow exciton states are controversial. The electroabsorption work was inconclusive since the applied perturbation could mix P states with S and D states. This problem is avoided by using resonant Raman scattering since experiments are performed on the unperturbed crystal. Nevertheless, interpretation has still been difficult. In the first place mixing may occur between S and D exciton states.

FIG. 3-1. Schematic representation of the multipole-dipole Raman-scattering mechanism. Electric quadrupole absorption is to one of the S states of the yellow exciton series. There is then a transition to a state of a dipole-allowed exciton series via the electron-lattice interaction. The system returns to the ground state through dipole emission.

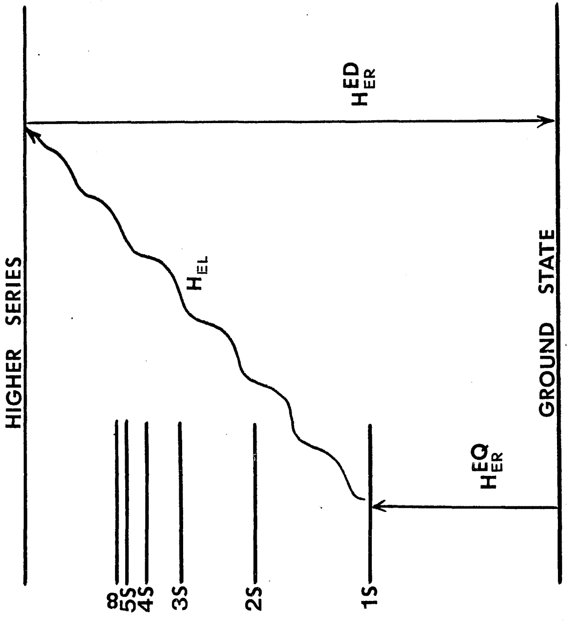
HIGHER SERIES
GROUND STATE
∞
5S
4S
3S
2S
1S
H_{EL}
H_{ER}^{ED}
H_{ER}^{EQ}

Since D states have some Γ_5^+ character, this admits the possibility of resonant enhancement at D states which should otherwise give no enhancement since the envelope function at the origin (which determines the transition probability for quadrupole transitions) vanishes for D states. Secondly, the n = 1 member of the green exciton series (derived from a Γ_8^+ valence band and a Γ_6^+ conduction band) has a Γ_5^+ component and could occur in the region of the yellow excited states. Incidentally, the 1S state of the green series also has components of Γ_4^+ symmetry (magnetic dipole) which can give rise to resonant enhancement as in the electric quadrupole case. Finally the 2S state of the yellow series has never been located. The present research was motivated in part by the desirability of resolving the controversy over assignments.

E. Exciton Basis Functions

In the effective mass approximation, exciton wavefunctions are given by

$$\Psi = \phi_n(\vec{r}_e - \vec{r}_h)\,\Psi_v(\vec{r}_h)\,\Psi_c(\vec{r}_e) \tag{3-46}$$

i.e., an envelope function ϕ of the relative electron hole motion multiplying a pair of zone center Bloch band functions.

Since the conduction band is an orbital singlet (Γ_1^+) times a spin doublet (Γ_6), there are two possible conduction states $\Psi_c = \alpha_c$ or β_c, (spin up or down) multiplying a totally symmetric spatial part which we will not explicitly include.

The valence band is an orbital triplet Γ_5^+ transforming like xz, yz or xy times a spin doublet (α or β) giving 6 valence states and thus, when combined with the 2 conduction states, 12 pair states of the form

$$\psi_v \psi_c = [xy(\alpha)][\beta_c] \tag{3-47}$$

The 12 basis functions to be used in the calculation are linear combinations of the simple product functions of Eq. (3-47) chosen both to diagonalize the major part of the perturbation in the unstrained crystal and to exhibit the appropriate symmetries of the yellow and green excitons.

The transformation is accomplished in two steps. First, the 6 valence functions $\psi_v = xy\alpha$ etc. are combined to form two Γ_7^+ and four Γ_8^+ basis functions using the coefficients (coupling constants) given in Koster et al.[51]. Since these functions transform as representations of the appropriate double group, they automatically diagonalize the spin-orbit interaction. The 6 valence functions are given in Table 3-1 both in Cartesian coordinates and in spherical harmonics. Next, the four "yellow" product functions formed from the two valence states and the conduction α_c or β_c are combined into four new product functions, one transforming as Γ_2' and three as Γ_5 which are then the appropriate functions for the exchange-split para and ortho yellow excitons. Similarly, the eight "green" product functions formed from the four Γ_8^+ valence states and the conduction α_c or β_c are combined into eight

TABLE 3-1

ZONE CENTER BLOCH FUNCTIONS (VALENCE BAND)

From Koster et al - Table 83

$$\psi^{\Gamma_7}_{1/2} = -\frac{i}{\sqrt{3}}\left[xy\alpha + (yz + ixz)\beta\right] = -\frac{1}{\sqrt{6}}\left[Y''\alpha + 2Y_2^{-1}\beta\right]$$

$$\psi^{\Gamma_7}_{-1/2} = -\frac{i}{\sqrt{3}}\left[-xy\beta + (yz - ixz)\alpha\right] = \frac{1}{\sqrt{6}}\left[Y''\beta - 2Y_2^{1}\alpha\right]$$

$$\psi^{\Gamma_8}_{3/2} = \frac{i}{\sqrt{6}}\left[2xy\beta + (yz - ixz)\alpha\right] = \frac{1}{\sqrt{3}}\left[Y''\beta + Y_2^{1}\alpha\right]$$

$$\psi^{\Gamma_8}_{1/2} = -\frac{i}{\sqrt{2}}\left[(yz - ixz)\beta\right] = -Y_2^{1}\beta$$

$$\psi^{\Gamma_8}_{-1/2} = \frac{i}{\sqrt{2}}\left[(yz + ixz)\alpha\right] = Y_2^{-1}\alpha$$

$$\psi^{\Gamma_8}_{-3/2} = \frac{i}{\sqrt{6}}\left[2xy\alpha - (yz + ixz)\beta\right] = \frac{1}{\sqrt{3}}\left[Y''\alpha - Y_2^{-1}\beta\right]$$

$$Y'' = Y_2^{-2} - Y_2^{2}$$

new functions transforming as a doublet Γ_3^+, a triplet Γ_4^+ and a triplet Γ_5^+ . The appropriate coefficients are again taken from Koster et al.[51]

These 12 product basis functions are diagonal in the spin orbit interaction, and the 4 yellow and 8 green functions are separately diagonal in the exchange interaction as well although inter-series exchange terms will remain. The 12 functions including envelope functions ϕ are listed in Table 3-2.

The ortho and para yellow excitons are not triplet and singlet spin states, as may be seen from the eigenfunctions in Table 3-2. The singlet Γ_2^+ paraexciton is pure spin triplet while the triplet Γ_5^+ orthoexciton is mixed spin singlet and triplet, as noted by Kuwabara et al.[43]

For a given orbital quantum state n (e.g., n = 1S) there will be two distinct envelope functions ϕ_{ny} and ϕ_{ng} for the yellow and green excitions, respectively, as indicated in the table.

The initial Hamiltonian (to be discussed in Section G) includes the spin-orbit interaction $H_{so} = (2/3)(\Delta \vec{L}\cdot\vec{\sigma})$ which splits the valence band into Γ_7^+ and Γ_8^+ (with Γ_8^+ lying below Γ_7^+ by the spin-orbit energy), and the Coulomb energy E_c^{gn} and E_c^{yn} for the green and yellow excitons, respectively. Thus, the energy E^o for the 12 basis states without strain or exchange will be $E^o = E_c^{yn}$ for the four yellow exciton states and $E_c^{gn} + \Delta$ for the eight green exciton states. These are also listed in Table 3-2.

Table 3-2. Wavefunctions and energies of the 4 yellow and 8 green exciton states in Cu_2O. The energies given do not include the effects of strain or electron-hole exchange. Functions of cartesian coordinates which transform like the wavefunctions are shown to the left of the Γ_4 and Γ_5 wavefunctions.

Exciton (Symmetry)		Wavefunction	Energy E^{0}
Yellow Paraexciton $({}^{1}\Gamma_2^{+})$		$\phi_{12} = \phi_{yn}(1/\sqrt{12})[Y''(\alpha\beta_c + \beta\alpha_c) + 2Y_2^{-1}\beta\beta_c - 2Y_2^{1}\alpha\alpha_c]$	E_c^{yn}
Yellow Orthoexciton $({}^{3}\Gamma_5^{+}$ Electric Quadrupole)	yz	$\phi_5 = \phi_{yn}(-i/\sqrt{12})[Y''(\alpha\alpha_c + \beta\beta_c) + 2Y_2^{-1}\beta\alpha_c - 2Y_2^{1}\alpha\beta_c]$	
	zx	$\phi_3 = \phi_{yn}(1/\sqrt{12})[Y''(\beta\beta_c - \alpha\alpha_c) - 2Y_2^{1}\alpha\beta_c - 2Y_2^{-1}\beta\alpha_c]$	E_c^{yn}
	xy	$\phi_{1c} = \phi_{yn}(-i/\sqrt{12})[Y''(\beta\alpha_c - \alpha\beta_c) - 2Y_2^{1}\alpha\alpha_c - 2Y_2^{-1}\beta\beta_c]$	
Green $({}^{3}\Gamma_4^{+}$ Magnetic Dipole)	x	$\phi_3 = \phi_{gn}(i/\sqrt{8})[Y''(\alpha\alpha_c + \beta\beta_c) + Y_2^{1}(\alpha\beta_c + \beta\alpha_c) - Y_2^{-1}(\beta\alpha_c + \alpha\beta_c)]$	
	y	$\phi_6 = \phi_{gn}(1/\sqrt{8})[Y''(\beta\beta_c - \alpha\alpha_c) + Y_2^{1}(\beta\alpha_c + \alpha\beta_c) + Y_2^{-1}(\beta\alpha_c + \alpha\beta_c)]$	$\Delta + E_c^{gn}$
	z	$\phi_1 = \phi_{gn}(i/\sqrt{2})[Y_2^{-1}\alpha\alpha_c + Y_2^{1}\beta\beta_c]$	
Green $({}^{2}\Gamma_3^{+}$ Electric Quadrupole)		$\phi_2 = \phi_{gn}(-1/\sqrt{2})[Y_2^{-1}\alpha\alpha_c - Y_2^{1}\beta\beta_c]$	$\Delta + E_c^{gn}$
		$\phi_{11} = \phi_{gn}(-1/\sqrt{6})[Y''(\alpha\beta_c + \beta\alpha_c) + Y_2^{1}\alpha\alpha_c - Y_2^{-1}\beta\beta_c]$	
Green $({}^{3}\Gamma_5^{+}$ Electric Quadrupole)	yz	$\phi_4 = \phi_{gn}(-i/\sqrt{24})[Y''(\alpha\alpha_c + \beta\beta_c) + 3(Y_2^{-1}\alpha\beta_c - Y_2^{1}\beta\alpha_c) + Y_2^{1}\alpha\beta_c - Y_2^{-1}\beta\alpha_c]$	
	zx	$\phi_7 = \phi_{g1}(1/\sqrt{24})[Y''(\beta\beta_c - \alpha\alpha_c) - 3(Y_2^{-1}\alpha\beta_c + Y_2^{1}\beta\alpha_c) + Y_2^{-1}\beta\alpha_c + Y_2^{1}\alpha\beta_c]$	
	xy	$\phi_9 = \phi_{gn}(1/\sqrt{6})[Y''(\beta\alpha_c - \alpha\beta_c) + Y_2^{1}\alpha\alpha_c + Y_2^{-1}\beta\beta_c]$	$\Delta + E_c^{gn}$

F. Effects of Stress[44,52]

1. Band Effects

The application of uniaxial stress and the consequent strain lead to a change in the lattice parameter and the symmetry of the solid. The resultant changes in the electronic band structure can be determined by investigating the stress-dependence of the optical spectra. The application of anisotropic strain to a crystal is a unique tool because it has no analog outside of solid state physics. In recent years it has become a powerful technique for revealing degeneracies due to spatial symmetry (except inversion) in a manner similar to the removal of time-invariance symmetry by magnetic fields. Experiments which have studied the stress-induced splittings and shifts of energy levels and oscillator strengths as well as the dependence of the induced fine structure on polarization direction and strain configuration have provided information concerning the intrinsic properties of the undeformed crystal such as symmetries of interband transitions, deformation potentials and the exciton spin-exchange interaction. Comparison between the symmetry assignments so obtained and existing band calculations may be made while the deformation potentials are of value for comparison with theories based on model calculations.

In the absence of strain or spin-orbit splitting the valence-band edge at $\vec{k} = o$ in diamond or zincblende-type materials is a sixfold degenerate p-like multiplet with orbital symmetry Γ_5 (diamond) or Γ_4 (zincblende). The spin-orbit interaction lifts this degeneracy into a fourfold multiplet (J = 3/2) and a twofold level (J = 1/2). The application of a uniaxial stress splits the J = 3/2 multiplet into a pair of degenerate Kramers doublets. In Cu_2O, with point group O_h, the situation is somewhat analogous. As shown in Fig. 2-2, the highest valence band is a sixfold multiplet derived from d orbitals (the remaining d states having been split off by the cubic crystal field). The spin-orbit interaction splits this manifold into a quartet and a doublet with symmetry ${}^4\Gamma_8^+$ and ${}^2\Gamma_7^+$ respectively, using the double-group notation. The lowest conduction band is s-like, having only the Kramers degeneracy. Application of uniaxial stress will split the ${}^4\Gamma_8^+$ band into a pair of Kramers doublets whereas the degeneracies of the ${}^2\Gamma_7^+$ band and the conduction band are unaffected. The situation for Cu_2O is shown in Fig. 3-2 for stresses of two different symmetries.

The effects of strain on the bands may be determined by the orbital-strain Hamiltonian which, for cubic crystals, is written as[44,52,53]

$$H_D = a(\epsilon_{xx} + \epsilon_{yy} + \epsilon_{zz}) - 3b\{(L_z^2 - L^2/3)\epsilon_{zz} + c.p.\}$$
$$- 2\sqrt{3}\,d\,\{(L_xL_y + L_yL_x)\epsilon_{xy} + c.p.\} \qquad (3\text{-}48)$$

where L is the angular momentum operator, the ϵ_{ij} are components of the strain tensor and cp denotes cyclic permutation with respect to x,y,z. The constant a represents the shift of the orbital bands due to the hydrostatic component of the stress. It is related to the stress-induced volume change of the unit cell and affects the magnitude of the band gap. The quantities b and d are orbital uniaxial deformation potentials appropriate to strains of tetragonal and rhombohedral symmetry, respectively. They account for the anisotropy of the strain and therefore relate to the change in symmetry of the unit cell. The anisotropic part of the strain is reflected in general in the lowering of degeneracies (splitting of bands). The form of Eq. (3-48) is determined from the theory of invariants[53,54] and is constructed so that the Hamiltonian transforms like a scalar.

It is a straightforward matter to derive the Hamiltonian for specific stress directions in the cubic crystal. For the case of tetragonal strain ([001] direction) we have

$$\begin{aligned} \epsilon_{xx} &= \epsilon_{yy} = S_{12}X \\ \epsilon_{zz} &= S_{11}X \\ \epsilon_{xy} &= \epsilon_{xz} = \epsilon_{yz} = 0 \end{aligned} \tag{3-49}$$

where S_{ij} are elastic compliance constants and X is the applied stress. Eq. (3-48) becomes

$$H_{D_{001}} = hX + e(L_z^2 - L^2/3)X \tag{3-50}$$

where

$$\begin{aligned} h &= a(S_{11} + 2S_{12}) \\ e &= -3b(S_{11} - S_{12}) \end{aligned} \tag{3-51}$$

FIG. 3-2. Effects of uniaxial stress on the energy bands in cuprous oxide. The center column (for the unstrained crystal) displays the degeneracies and symmetries of the (${}^2\Gamma_6^+$) conduction band and the (spin-orbit split partner) valence bands ${}^4\Gamma_8^+$ and ${}^2\Gamma_7^+$. The effect of a tetragonal (rhombohedral) stress is shown on the right (left). In each column the resultant crystal symmetry is shown on top and the double-group notation is used to classify the resultant bands. For either stress a splitting of the ${}^4\Gamma_8^+$ band occurs while the other bands retain a twofold degeneracy.

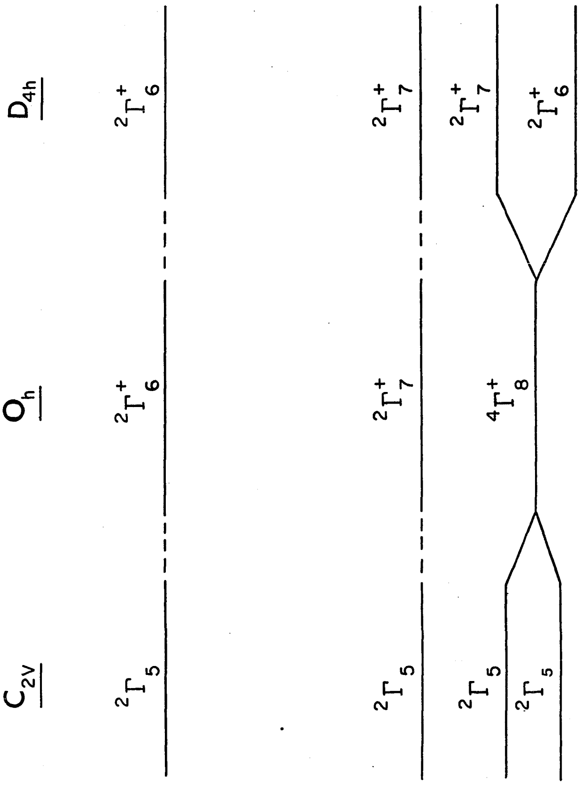
C_{2v}
O_h
D_{4h}
$^2\Gamma_5$
$^2\Gamma_6^+$
$^2\Gamma_6^+$
$^2\Gamma_5$
$^2\Gamma_7^+$
$^2\Gamma_7^+$
$^2\Gamma_5$
$^2\Gamma_5$
$^4\Gamma_8^+$
$^2\Gamma_7^+$
$^2\Gamma_6^+$

For rhombohedral stress ([110] direction) the elements of the strain tensor are

$$\begin{aligned}\epsilon_{xx} &= \epsilon_{yy} = \tfrac{1}{2}(S_{11}+S_{12})X \\ \epsilon_{zz} &= S_{12}X \\ \epsilon_{xy} &= \tfrac{1}{4}S_{44}X \\ \epsilon_{xz} &= \epsilon_{yz} = 0\end{aligned} \tag{3-52}$$

In this case Eq. (3-48) reduces to

$$H_{D_{110}} = hX - \frac{e}{2}(L_z^2 - L^2/3)X + f(L_xL_y + L_yL_x)X \tag{3-53}$$

where

$$f = -\frac{\sqrt{3}\,d}{2}\,S_{44} \tag{3-54}$$

Eqs. (3-50) and (3-53) will be used in section G.

2. Kramers' Theorem[55]

The operation of time reversal requires reversing all velocities and letting time proceed in the reverse direction so that a system runs back through its past history. By considering the time-dependent Schrodinger equation it is easy to see that if one neglects spin, the time reversal operator simply transforms a wavefunction into its complex conjugate. The state ψ^* will evolve into +t exactly the same way as ψ would have evolved in the -t direction. Since probability density is proportional to $|\psi|^2$, it is unaffected by the operation. However, the momentum distribution, being proportional to the imaginary part of $\psi^*\nabla\psi$, is reversed, as it should be. If we consider a stationary state, its energy is unchanged since $H\psi = E\psi$ implies $H\psi^* = E\psi^*$. There will or will not be a degeneracy associated with this symmetry depending on whether the set of ψ^* is or is not linearly independent of the set of ψ corresponding to a given energy. It must be noted that any magnetic field present in the Hamiltonian must be reversed in the time-reversal operation.

When spin is included, the time-reversal operator is not simply the operation of complex conjugation. Rather it can be shown to be a product of the complex conjugation operator with a product of Pauli spin matrices. This has the immediate consequence that the wavefunction for a system containing an odd number of electrons must be orthogonal to the time-reversed wavefunction. Since these wavefunctions must have the same energy, by time-reversal symmetry, a double degeneracy must exist. All energy levels of a system containing an odd number of electrons must be at least doubly degenerate regardless of how low the symmetry is, provided there are no magnetic fields present to remove time-reversal symmetry. This is Kramers' theorem.

A special case of this necessary degeneracy is the inability of a static stress to remove the Kramers degeneracy. The effects of stress on the bands of Cu_2O were illustrated in Fig. 3-2 for stress along two different directions. It is now seen that the resultant twofold degeneracies are a consequence of time-reversal symmetry.

This could have been arrived at more simply as follows.

The strain tensor can be decomposed into parts which transform (under O_h) according to ${}^1\Gamma_1^+$, ${}^2\Gamma_3^+$ and ${}^3\Gamma_5^+$. For example the trace $\sum_i \epsilon_{ii}$, is a scalar and transforms like ${}^1\Gamma_1^+$. Now according to the Wigner-Eckhart theorem, the matrix element of an operator $\langle \Psi' / H / \Psi \rangle$ may fail to vanish (and a splitting can occur) only if the representation Γ^{Ψ} is contained in $\Gamma^{\Psi} \otimes \Gamma^{H}$. Table 3-3 gives the product multiplications for the group O_h. It is seen that the above condition is satisfied (using the strain symmetries discussed above) for wavefunctions with symmetry Γ_8^+ but not for wavefunctions of symmetry Γ_6^+ or Γ_7^+. This corresponds to the Kramers requirement and to the band scheme of Fig. 3-2.

3. Effects of stress on the Exciton Spectrum

In 1961, Gross and Kaplyanskii[8] observed a stress-induced splitting of the 1S state of the yellow exciton in Cu_2O. This effect cannot be explained within the framework of one-electron theory since the bands which form the yellow series are Kramers doublets and therefore cannot split under stress. The behavior was explained by Elliott[9] as an exciton effect involving the two-particle nature of the exciton. The splitting (exchange-strain splitting) will be shown to be a second-order effect in section G. Exciton states deriving from the (Kramers degenerate) ${}^2\Gamma_7^+$ and ${}^2\Gamma_6^+$ bands, that is states of the yellow series,. are coupled by the strain and by the electron-hole exchange interaction to exciton states associated with the ${}^4\Gamma_8^+$ and ${}^2\Gamma_6^+$ bands (green series states) which can be stress-split.

That the splitting is an exciton effect can be seen simply using group theoretical arguments. As previously discussed, the (S-like) yellow exciton states are formed from bands of symmetry ${}^2\Gamma_6^+$ and ${}^2\Gamma_7^+$. It was shown in section F.2 and Fig. 3-2 that these bands do not split under stress. The exciton states formed from these bands, however, are of symmetry ${}^3\Gamma_5^+$ and ${}^1\Gamma_2^+$ where the ${}^3\Gamma_5^+$ (orthoexciton) is optically "active" in the quadrupole approximation. Fig. 3-3 gives the effect of strains of different symmetry on states, using group theoretical compatability. We see that the triple degeneracy may, in principle, be removed by stress even though the associated bands (Fig. 3-2) are not split.

It turns out that states of the green series also have a stress-dependence determined by coupling to the states of the yellow series. However, unlike the yellow series, states of the green series are split in first-order due to the splitting of the ${}^4\Gamma_8^+$ valence band. The exchange-strain splitting of exciton levels in Cu_2O has recently been treated in detail by Kiselev and Zhilich.[24]

The exchange-strain splitting has also been observed in other crystals. Koda and Langer[57] reported a strain-induced splitting of exciton states in wurtzite crystals. The occurence of a splitting in spite of the Kramers degenerate bands was explained by Akimoto and Hasegawa[56] on the basis of the exchange effect.

TABLE 3-3. PRODUCT MULTIPLICATION TABLE FOR THE GROUP O_h

Γ_1	Γ_2	Γ_3	Γ_4	Γ_5	Γ_6	Γ_7	Γ_8	
Γ_1	Γ_2	Γ_3	Γ_4	Γ_5	Γ_6	Γ_7	Γ_8	Γ_1
	Γ_1	Γ_3	Γ_5	Γ_4	Γ_7	Γ_6	Γ_8	Γ_2
		$\Gamma_1+\Gamma_2+\Gamma_3$	$\Gamma_4+\Gamma_5$	$\Gamma_4+\Gamma_5$	Γ_8	Γ_8	$\Gamma_6+\Gamma_7+\Gamma_8$	Γ_3
			$\Gamma_1+\Gamma_3$ $+\Gamma_4+\Gamma_5$	$\Gamma_2+\Gamma_3$ $+\Gamma_4+\Gamma_5$	$\Gamma_6+\Gamma_8$	$\Gamma_7+\Gamma_8$	$\Gamma_6+\Gamma_7+2\Gamma_8$	Γ_4
				$\Gamma_1+\Gamma_3$ $+\Gamma_4+\Gamma_5$	$\Gamma_7+\Gamma_8$	$\Gamma_6+\Gamma_8$	$\Gamma_6+3\Gamma_8$	Γ_5
					$\Gamma_1+\Gamma_4$	$\Gamma_2+\Gamma_5$	$\Gamma_3+\Gamma_4+\Gamma_5$	Γ_6
						$\Gamma_1+\Gamma_4$	$\Gamma_3+\Gamma_4+\Gamma_5$	Γ_7
							$\Gamma_1+\Gamma_2+\Gamma_3$ $+2\Gamma_4+2\Gamma_5$	Γ_8

Table 3-4. Character table and basis functions for the group O_h

	E	$\bar{E}$	$8C_3$	$8\bar{C}_3$	$3C_2$ $3\bar{C}_2$	$6C_4$	$6\bar{C}_4$	$6C_2'$ $6\bar{C}_2'$	I	$\bar{I}$	$8S_6$	$8\bar{S}_6$	$3\sigma_h$ $3\bar{\sigma}_h$	$6S_4$	$6\bar{S}_4$	$6\sigma_d$ $6\bar{\sigma}_d$	Basis Functions
Γ_1^+	1	1	1	1	1	1	1	1	1	1	1	1	1	1	1	1	R
Γ_2^+	1	1	1	1	1	−1	−1	−1	1	1	1	1	1	−1	−1	−1	$(x^2-y^2)(y^2-z^2)(z^2-x^2)$
Γ_3^+	2	2	−1	−1	2	0	0	0	2	2	−1	−1	2	0	0	0	$(2z^2-x^2-y^2), \sqrt{3}(x^2-y^2)$
Γ_4^+	3	3	0	0	−1	1	1	−1	3	3	0	0	−1	1	1	−1	S_x, S_y, S_z
Γ_5^+	3	3	0	0	−1	−1	−1	1	3	3	0	0	−1	−1	−1	1	xy, yz, zx
Γ_1^-	1	1	1	1	1	1	1	1	−1	−1	−1	−1	−1	−1	−1	−1	$\Gamma_2^- \times \Gamma_2^+$
Γ_2^-	1	1	1	1	1	−1	−1	−1	−1	−1	−1	−1	−1	1	1	1	xyz
Γ_3^-	2	2	−1	−1	2	0	0	0	−2	−2	1	1	−2	0	0	0	$\Gamma_3^+ \times \Gamma_2^-$
Γ_4^-	3	3	0	0	−1	1	1	−1	−3	−3	0	0	1	−1	−1	1	x, y, z
Γ_5^-	3	3	0	0	−1	−1	−1	−1	−3	−3	0	0	1	1	1	1	$\Gamma_5^+ \times \Gamma_1^-$
Γ_6^+	2	−2	1	−1	0	2	$-\sqrt{2}$	0	2	−2	1	−1	0	$\sqrt{2}$	$-\sqrt{2}$	0	$\psi(1/2, 1/2), \psi(1/2, -1/2)$
Γ_7^+	2	−2	1	−1	0	−2	$\sqrt{2}$	0	2	−2	1	−1	0	$-\sqrt{2}$	$\sqrt{2}$	0	$\Gamma_6^+ \times \Gamma_2^+$
Γ_8^+	4	−4	−1	1	0	0	0	0	4	−4	−1	1	0	0	0	0	$\{\psi(3/2, 3/2), \psi(3/2, 1/2),$ $\psi(3/2, -1/2), \psi(3/2, -3/2)$
Γ_6^-	2	−2	1	−1	0	2	$-\sqrt{2}$	0	−2	2	−1	1	0	$-\sqrt{2}$	$\sqrt{2}$	0	$\Gamma_6^+ \times \Gamma_1^-$
Γ_7^-	2	−2	1	−1	0	−2	$\sqrt{2}$	0	−2	2	−1	1	0	$\sqrt{2}$	$-\sqrt{2}$	0	$\Gamma_6^+ \times \Gamma_2^-$
Γ_8^-	4	−4	−1	1	0	0	0	0	−4	4	1	−1	0	0	0	0	$\Gamma_8^+ \times \Gamma_1^-$

Table 3-5. Character table and basis functions for the group D_{4h}

	E	$\bar{E}$	$2C_4$	$2\bar{C}_4$	C_2 $\bar{C}_2$	$2C_2'$ $2\bar{C}_2'$	$2C_2''$ $2\bar{C}_2''$	I	$\bar{I}$	$2S_4$	$2\bar{S}_4$	σ_h $\bar{\sigma}_h$	$2\sigma_v$ $2\bar{\sigma}_v$	$2\sigma_d$ $2\bar{\sigma}_d$	Basis Functions
	1	1	1	1	1	1	1	1	1	1	1	1	1	1	R
	1	1	1	1	1	-1	-1	1	1	1	1	1	-1	-1	S_z
	1	1	-1	-1	1	1	-1	1	1	-1	-1	1	1	-1	$(x^2 - y^2)$
	1	1	-1	-1	1	-1	1	1	1	-1	-1	1	-1	1	xy
	2	2	0	0	-2	0	0	2	2	0	0	-2	0	0	S_x, S_y
	1	1	1	1	1	1	1	-1	-1	-1	-1	-1	-1	-1	$(x^2 - y^2)xyz$
	1	1	1	1	1	-1	-1	-1	-1	-1	-1	-1	1	1	z
	1	1	-1	-1	1	1	-1	-1	-1	1	1	-1	-1	1	xyz
	1	1	-1	-1	1	-1	1	-1	-1	1	1	-1	1	-1	$(x^2 - y^2)z$
	2	2	0	0	-2	0	0	-2	-2	0	0	2	0	0	x, y
	2	-2	$\sqrt{2}$	$-\sqrt{2}$	0	0	0	2	-2	$\sqrt{2}$	$\sqrt{2}$	0	0	0	$\psi(\frac{1}{2},\frac{1}{2}), \psi(\frac{1}{2},-\frac{1}{2})$
	2	-2	$-\sqrt{2}$	$\sqrt{2}$	0	0	0	2	-2	$\sqrt{2}$	$\sqrt{2}$	0	0	0	$\Gamma_6^+ \times \Gamma_3^+$
	2	-2	$\sqrt{2}$	$-\sqrt{2}$	0	0	0	-2	2	$\sqrt{2}$	$\sqrt{2}$	0	0	0	$\Gamma_6^+ \times \Gamma_1^-$
	2	-2	$-\sqrt{2}$	$\sqrt{2}$	0	0	0	-2	2	$\sqrt{2}$	$\sqrt{2}$	0	0	0	$\Gamma_6^+ \times \Gamma_3^-$

TABLE 3-6. CHARACTER TABLE AND BASIS FUNCTIONS FOR THE GROUP C_{2V}

	E	$\bar{E}$	C_2 $\bar{C}_2$	σ_v $\bar{\sigma}_v$	σ_v' $\bar{\sigma}_v'$	Basis Functions
Γ_1	1	1	1	1	1	x_3
Γ_2	1	1	−1	1	−1	S_{x_2} or x_1
Γ_3	1	1	1	−1	−1	S_{x_3} or $x_1 x_2$
Γ_4	1	1	−1	−1	1	S_{x_1} or x_2 or $x_2 x_3$
Γ_5	2	−2	0	0	0	$\dot{\psi}(\frac{1}{2},\frac{1}{2})$ $\dot{\psi}(\frac{1}{2},-\frac{1}{2})$

TABLE 3-7. MULTIPLICATION TABLE FOR THE GROUP D_{4h}

Γ_1	Γ_2	Γ_3	Γ_4	Γ_5	Γ_6	Γ_7	
Γ_1	Γ_2	Γ_3	Γ_4	Γ_5	Γ_6	Γ_7	Γ_1
	Γ_1	Γ_4	Γ_3	Γ_5	Γ_6	Γ_7	Γ_2
		Γ_1	Γ_2	Γ_5	Γ_7	Γ_6	Γ_3
			Γ_1	Γ_5	Γ_7	Γ_6	Γ_4
				$\Gamma_1 + \Gamma_2 + \Gamma_3 + \Gamma_4$	$\Gamma_6 + \Gamma_7$	$\Gamma_6 + \Gamma_7$	Γ_5
					$\Gamma_1 + \Gamma_2 + \Gamma_5$	$\Gamma_3 + \Gamma_4 + \Gamma_5$	Γ_6
						$\Gamma_1 + \Gamma_2 + \Gamma_5$	Γ_7

TABLE 3-8. MULTIPLICATION TABLE FOR THE GROUP C_{2V}

Γ_1	Γ_2	Γ_3	Γ_4	Γ_5	
Γ_1	Γ_2	Γ_3	Γ_4	Γ_5	Γ_1
	Γ_1	Γ_4	Γ_3	Γ_5	Γ_2
		Γ_1	Γ_2	Γ_5	Γ_3
			Γ_1	Γ_5	Γ_4
				$\Gamma_1 + \Gamma_2 + \Gamma_3 + \Gamma_4$	Γ_5

TABLE 3-9. O_h Compatibility Table

O_h	Γ_1^+	Γ_2^+	Γ_3^+	Γ_4^+	Γ_5^+	Γ_6^+	Γ_7^+	Γ_8^+	Γ_1^-	Γ_2^-	Γ_3^-	Γ_4^-	Γ_5^-	Γ_6^-	Γ_7^-	Γ_8^-
D_{4h}	Γ_1^+	Γ_3^+	$\Gamma_1^+ + \Gamma_3^+$	$\Gamma_2^+ + \Gamma_5^+$	$\Gamma_4^+ + \Gamma_5^+$	Γ_6^+	Γ_7^+	$\Gamma_6^+ + \Gamma_7^+$	Γ_1^-	Γ_3^-	$\Gamma_1^- + \Gamma_3^-$	$\Gamma_2^- + \Gamma_5^-$	$\Gamma_4^- + \Gamma_5^-$	Γ_6^-	Γ_7^-	$\Gamma_6^- + \Gamma_7^-$
C_{2V}	Γ_1	Γ_2	$\Gamma_1 + \Gamma_2$	$\Gamma_2 + \Gamma_3 + \Gamma_4$	$\Gamma_1 + \Gamma_3 + \Gamma_4$	Γ_5	Γ_5	$2\Gamma_5$	Γ_3	Γ_4	$\Gamma_3 + \Gamma_4$	$\Gamma_1 + \Gamma_2 + \Gamma_4$	$\Gamma_1 + \Gamma_2 + \Gamma_3$	Γ_5	Γ_5	$2\Gamma_5$

4. Group Theoretical Compatibility and Selection Rules

Analysis of the results of experiments in which symmetry-breaking perturbations are applied to the crystal is greatly facilitated by the use of group theory. The transformation properties of energy levels as well as symmetry-related degeneracies may be determined by calculations of a few steps. In addition, the results of lengthy calculations may be checked for consistency with group theoretical predictions.

In the present research, we will be concerned with the point groups O_h, D_{4h} and C_{2v}. The point group symmetry of the unit cell of the unstrained Cu_2O crystal is O_h. Tetragonal and rhombohedral strains lower this symmetry to D_{4h} and C_{2v}, respectively. The properties of these point groups are conveniently summarized in Tables 3-3 through 3-9[51]. Character tables for the three point groups are shown in Tables 3-4, 3-5 and 3-6. Multiplication tables are shown in Tables 3-3, 3-7 and 3-8. Compatibility between O_h and the other point groups is given in Table 3-9.

Group theory has already been used in the preceding sections in connection with the determination of the exciton basis functions in the unstrained crystal and for the discussion of stress-induced splittings. In Section E, the representations according to which the exciton basis functions transform were found by repeated reference to the O_h multiplication table, while the functions themselves were determined from tables of coupling coefficients.[51] In Sections F.1 and F.3 the compatibility table (Table 3.9) was

FIG. 3-3. Effect of stress on the ${}^3\Gamma_5^+$ orthoexciton in Cu_2O. The effects of tetragonal and rhombohedral stress are shown to the right and left, respectively. The point group symmetry of the unit cell is shown as the heading of each column. The symmetry and degeneracy of states is indicated for the point groups C_{2v} and D_{4h} that result from deformation.

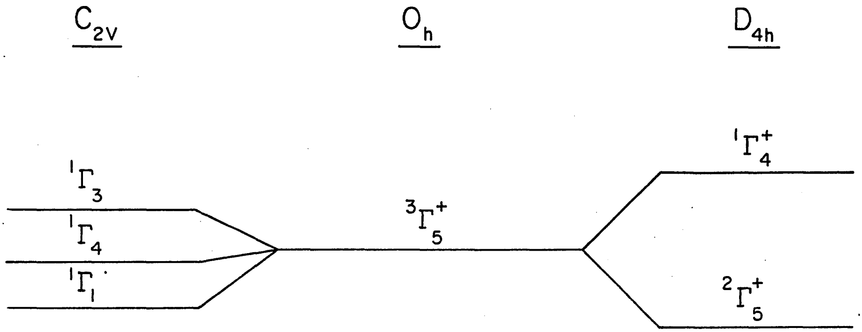
C_{2v}
O_h
D_{4h}
$^1\Gamma_3$
$^1\Gamma_4$
$^1\Gamma_1$
$^3\Gamma_5^+$
$^1\Gamma_4^+$
$^2\Gamma_5^+$

used to determine the possible splittings that could result from the application of stress. This simple analysis will be used as a check on the quantitative calculations of Section G. Group theory can also be used for deducing the polarization selection rules relevant to the quadrupole-dipole resonant Raman scattering process.

A scattering process (involving the 109 cm^{-1} phonon) corresponding to a given configuration of incident and scattered polarizations can proceed if the representation according to which the 109 cm^{-1} phonon transforms is contained in the reduction of the direct product of the representations corresponding to the electric quadrupole and electric dipole operators.

In the unstrained crystal, the ${}^3\Gamma_5^+$ orthoexciton transforms under O_h like xy, yz and zx (Table 3-4). Thus for light incident along $\hat{x}$, it can be excited by both y and z polarizations. The electric dipole operator transforms like x, y, and z (the ${}^3\Gamma_4^-$ representation) and the 109 cm^{-1} phonon transforms according to ${}^2\Gamma_3^-$. Table 3-3 shows that the direct product of ${}^3\Gamma_5^+$ with ${}^3\Gamma_4^-$ contains ${}^2\Gamma_3^-$. The phonon can therefore participate in the scattering process. Since the light is incident along $\hat{x}$, and since the experiments all involved the backscattering geometry, only y and z polarizations are possible. The above argument then implies that participation of the Γ_3^- phonon in quadrupole-dipole scattering is possible for the incident light polarized along y and the scattered light polarized along z or vice versa. The results are consistent with Birman's scattering tensors[26,32] and are displayed in Table 3-10.

Under a uniaxial stress along $\hat{z}$, the crystal symmetry is lowered to D_{4h} and the ${}^3\Gamma_5^+$ orthoexciton splits into ${}^1\Gamma_4^+$ and ${}^2\Gamma_5^+$ which transform as xy and yz, zx respectively. This splitting is obtained from the compatibility table (Table 3-9) and was shown in Fig. 3-3. The transformation properties are shown in the D_{4h} character table (Table 3-5). Reference to the same tables shows that the electric dipole operator splits into ${}^1\Gamma_2^-$, which transforms like z, and ${}^2\Gamma_5^-$ which transforms like x and y. The phonon representation splits into ${}^1\Gamma_1^-$ and ${}^1\Gamma_3^-$. Taking direct products of ${}^1\Gamma_4^+$ and ${}^2\Gamma_5^+$ with ${}^1\Gamma_2^-$ and ${}^2\Gamma_5^-$ shows that only ${}^2\Gamma_5^+ \otimes {}^2\Gamma_5^-$ and ${}^1\Gamma_4^+ \otimes {}^1\Gamma_2^-$ contain the 109 cm^{-1} representations in their reductions. This implies that for incident light polarized along y (corresponding to ${}^1\Gamma_4^+$ and therefore to the exciton state of this symmetry) scattering from the 109 cm^{-1} phonon can occur only in processes which result in scattered light polarized along z. Likewise scattering involving incident light polarized along z (which can excite the ${}^2\Gamma_5^+$ exciton) will produce scattered light polarized along y. The results are shown in Table 3-10. These selection rules, which agree with results obtained by R. Berenson[58], have been used in the present experiments to identify the symmetry of stress-split exciton states.

The case for rhombohedral stress is a bit more complex. Stress is applied along [110] (or $\hat{x} + \hat{y}$ in terms

TABLE 3-10. Selection rules for quadrupole-dipole resonant Raman scattering in Cu_2O. Only scattering from the 109 cm^{-1} ($^2\Gamma_3^-$) phonon is considered. The columns from left to right correspond to unstrained, tetragonally strained and rhombohedrally strained crystals. Square brackets are used for function transformation properties. Parentheses are used for polarization of incident and scattered light.

TABLE 3-10 QUADRUPOLE-DIPOLE RESONANT RAMAN SELECTION RULES

	O_h	D_{4h}	C_{2V}
Electric Quadrupole Operator	${}^3\Gamma_5^+$ [xy, yz, zx]	${}^1\Gamma_4^+$ [xy] ${}^2\Gamma_5^+$ [yz, zx]	${}^1\Gamma_1$ [xy] or $x_3^2 - x_1^2$ ${}^1\Gamma_3$ [yz - zx] or x_1x_2 ${}^1\Gamma_4$ [yz + zx] or x_3x_2
Electric Dipole Operator	${}^3\Gamma_4^-$ [x, y, z]	${}^1\Gamma_2^-$ [z] ${}^2\Gamma_5^-$ [x, y]	${}^1\Gamma_1$ [x + y] or x_3 ${}^1\Gamma_2$ [x - y] or x_1 ${}^1\Gamma_4$ [z] or x_2
109 cm^{-1} phonon	${}^2\Gamma_3^-$	${}^1\Gamma_1^-$ ${}^1\Gamma_3^-$	${}^1\Gamma_3$ ${}^1\Gamma_4$
Reduction of Direct Product for Quadrupole-Dipole Process	${}^3\Gamma_5^+ \otimes {}^3\Gamma_4^- = {}^1\Gamma_2^- + \underline{{}^2\Gamma_3^-} + {}^3\Gamma_4^- + {}^3\Gamma_5^-$	${}^2\Gamma_5^+ \otimes {}^1\Gamma_2^- = {}^2\Gamma_5^-$ ${}^1\Gamma_4^+ \otimes {}^2\Gamma_5^- = {}^2\Gamma_5^-$ $\Gamma_4^+ \otimes {}^1\Gamma_2^- = \underline{{}^1\Gamma_3^-}$ ${}^2\Gamma_5^+ \otimes {}^2\Gamma_5^- = \underline{{}^1\Gamma_1^-} + {}^1\Gamma_2^- + \underline{{}^1\Gamma_3^-} + {}^1\Gamma_4^-$	$\Gamma_4 \otimes \Gamma_1 = \underline{\Gamma_4}$ $\Gamma_3 \otimes \Gamma_2 = \underline{\Gamma_4}$ $\Gamma_1 \otimes \Gamma_4 = \Gamma_4$ $\Gamma_4 \otimes \Gamma_2 = \underline{\Gamma_3}$ $\Gamma_3 \otimes \Gamma_4 = \Gamma_2$ $\Gamma_4 \otimes \Gamma_4 = \Gamma_1$ $\Gamma_1 \otimes \Gamma_1 = \Gamma_1$ $\Gamma_3 \otimes \Gamma_1 = \underline{\Gamma_3}$ $\Gamma_1 \otimes \Gamma_2 = \Gamma_2$
Polarization Selection Rules for Participation of 109 cm^{-1} phonon	$x(yz)\bar{x}$ $x(zy)\bar{x}$	$x(yz)\bar{x}$ for ${}^2\Gamma_5^+$ exciton $x(zy)\bar{x}$ for ${}^1\Gamma_4^+$ exciton	$x_2(x_3x_3)\bar{x}_2$ & $x_2(x_3x_1)\bar{x}_2$ for Γ_4 exciton $x_2(x_1x_3)\bar{x}_2$ & $x_2(x_1x_1)\bar{x}_2$ for Γ_3 exciton See text for Γ_1 exciton

of the crystallographic axes) and the crystal symmetry is lowered to C_{2v}. Let the coordinate axes relevant to the C_{2v} point group be denoted x_1, x_2 and x_3. These are related to the crystallographic axes by[59]

$$\begin{aligned} X_1 &= \frac{1}{\sqrt{2}}(x-y) \\ X_2 &= -z \\ X_3 &= \frac{1}{\sqrt{2}}(x+y) \end{aligned} \qquad (\ 3\text{-}55\ )$$

The compatibility tal$=\frac{1}{\sqrt{2}}(X+y)$t the electric dipole operator ${}^3\Gamma_4^-$ splits into ${}^1\Gamma_1$, ${}^1\Gamma_2$ and ${}^1\Gamma_4$. However, arbitrary linear combinations of the ${}^3\Gamma_4^-$ basis functions will not be eigenfunctions in the (rhombohedrally) strained crystal. The compatibility between the ${}^3\Gamma_4^-$ basis functions and the (C_{2v}) functions ${}^1\Gamma_1$, ${}^1\Gamma_2$ and ${}^1\Gamma_4$ is obtained as follows. The C_{2v} character table shows that ${}^1\Gamma_1$ transforms like x_3 while Eq. (3-55) shows that $x_3 = (1/\sqrt{2})(x+y)$. Therefore the electric dipole basis functions appropriate to the strained crystal can be obtained from those in the unstrained crystal by taking the linear combinations given on the right-hand side of Eq. (3-55). In the same way, the linear combinations of ${}^3\Gamma_5^+$ electric quadrupole basis functions which are compatible with C_{2v} symmetry are xy, yz+zx, and yz−zx. The analogous linear combinations are required for all of the basis functions discussed in Section E.

With this in mind the selection rules for the rhombohedrally-stressed crystal can be discussed. As for the tetragonal (D_{4h}) case, the compatibility is determined from Table 3-9. The results are shown in Table 3-10 where transformation properties are given both in the x_1, x_2, x_3 coordinate system and in terms of the crystallographic axes. Selection rules are again obtained by taking direct products between electric quadrupole representations ($'\Gamma_1$, $'\Gamma_3$ and $'\Gamma_4$), and electric dipole representations (Γ_1, Γ_2, and Γ_4) to see which products contain phonon representations. The results are shown in terms of x_1, x_2 and x_3. Crystals used in the experiment were cut so that stress was applied along $\hat{x}_3$ ($= \hat{x} + \hat{y} = [110]$) and backscattering experiments were done with light incident along $\hat{x}_2$ ($= -\hat{z} = [00\bar{1}]$). Subject to these constraints, it is seen from the table that the Γ_4 exciton may be excited by light polarized along x_3 (parallel to the stress) and that scattering from the 109 cm^{-1} phonon results in both x_3 and x_1 polarized scattered light. The Γ_3 exciton is excited by x_1 polarization (perpendicular to the stress) and results in x_2 and x_1 polarizations for the scattered light. In such backscattering experiments, then, resonant Raman scattering involving the $'\Gamma_3$ exciton or $'\Gamma_4$ exciton may be distinguished by the polarization of the incident light.

Coupling to the $'\Gamma_1$ exciton is more difficult. It transforms like $x_3^2 - x_1^2$ and therefore requires the wavevector and polarization of the incident light both to have components along $\hat{x}_1$ and $\hat{x}_3$. It is obvious that the backscattering experiments discussed above do not permit this. Ideally, the wavevector should be parallel to $\hat{x}_1 - \hat{x}_3$

while the polarization should be along $\hat{x}_1 + \hat{x}_3$. However, this could be achieved only by cutting a "V"-shaped notch into the $(1\bar{1}0)$ face which would weaken the crystal significantly. In addition, determination of the applied stress would be quite difficult. A practical solution to the problem is to cut the crystal with an extra face with normal parallel to $\hat{x}_1 + \hat{x}_2$ (the $[1\bar{1}\sqrt{2}]$ direction). This geometry allows the wavevector and electric vector to both have components along x_1. In addition, the extra cut does not affect sample strength or stress determination. Using this geometry Gross[8] showed that absorption to the Γ_1 component of the stress-split 1S state of the yellow series, with the wavevector confined to the x_1 x_2 plane was maximized for the wavevector along $\hat{x}_1 + \hat{x}_2$.

G. Effective Hamiltonian Formalism

1. Tetragonal Stress

The dependence of the energy of exciton levels on stress may be calculated using the effective Hamiltonian formalism of Pikus[70]. The following treatment is based on similar analyses by Kiselev and Zhilich[24], by Langer, Euwema, Era and Koda[71] and by Cho[60].

The starting point for the calculation is the effective mass approximation in which exciton wavefunctions are given by

$$\Psi = \phi_n(\vec{r}_e - \vec{r}_h)\,\psi_v(\vec{r}_h)\,\psi_c(\vec{r}_e) \qquad (3\text{-}56)$$

i.e. an envelope function ϕ of the relative electron-hole motion multiplying a pair of zone-center Bloch band functions. The 12 exciton states comprising the yellow and green series have been given in Table 3-2.

The effective exciton Hamiltonian is $H = H^o + H'$ where H^o includes the electron-hole Coulomb interaction H_c and the spin-orbit interaction

$$H_{so} = \frac{2}{3} \Delta \vec{L} \cdot \vec{\sigma} \tag{3-57}$$

where Δ is the spin-orbit energy and L and σ are orbital and spin angular momentum operators which act on valence band wavefunctions. H_{so} splits the valence band into Γ_7^+ and Γ_8^+ and thus separates the yellow and green exciton series. The perturbation Hamiltonian is taken to be

$$H' = H_D + H_{EX} \tag{3-58}$$

where H_D describes the effects of deformation on the valence and conduction bands, and H_{EX} represents the valence hole-conduction electron exchange interaction. The deformation Hamiltonian for tetragonal stress was discussed in Section F.1 where it was shown

$$H_{D_{001}} = hX + e(L_z^2 - L^2/3)X \tag{3-59}$$

where X is the applied stress and h and e are deformation parameters. The first term in Eq. (3-59) represents the effect of the hydrostatic component of the strain on the band gap while the second term produces the strain splitting of the ${}^4\Gamma_8^+$ valence band as well as band mixing effects.

The exchange part of the Hamiltonian can be written

$$H_{EX} = \frac{1}{2} F J^{A} \vec{\sigma}_e \cdot \vec{\sigma}_h \qquad (3\text{-}60)$$

where J^A is an atomic exchange constant, $\vec{\sigma}_e$ and $\vec{\sigma}_h$ operate on conduction electron and valence hole spin functions respectively, and F is a factor which gives the probability that the electron and hole are in the same cell.

$$F = |\phi(0)|^2 \qquad (3\text{-}61)$$

The exchange interaction discussed in Section B.3, is $\frac{1}{2} FJ^A$ and will depend both on the valence band involved and on the principle quantum number n of the exciton state since $|\phi(\vec{r}_e - \vec{r}_n = 0)|^2 \sim n^{-3}$. For a given n, the matrix elements of H_{ex} are

$$\langle \phi_i | H_{EX} | \phi_j \rangle = \frac{1}{2} J_{ij} \langle i | \vec{\sigma}_e \cdot \vec{\sigma}_h | j \rangle \qquad (3\text{-}62)$$

where $\langle i|$ and $|j\rangle$ refer to the spin part of the wavefunctions in Table 3-2 and J_{ij} is:

$$\begin{aligned} J_{yg} &= \sqrt{J_y^A J_g^A}\,\left(\phi_{ny}^*(0)\, \phi_{ng}(0) \right) \equiv J \\ J_{yy} &= J_y^A\, |\phi_{ny}(0)|^2 \equiv J_y \\ J_{gg} &= J_g^A\, |\phi_{ng}(0)|^2 \equiv J_g \end{aligned} \qquad (3\text{-}63)$$

The matrix of the effective Hamiltonian in the 12 state basis of Table 3-2 is given in Table 3-11. In computing the matrix elements of the deformation potential H_D, envelope function factors of the form $\int \phi_i^* \phi_j \, d^3r$ occur. For yellow-yellow or green-green matrix elements these are equal to unity by definition. For matrix elements between yellow and green states they turn out to be nearly equal to unity as well and have thus not been included explicitly in Table 3-11.

Several aspects of the energy matrix should be noted:

(1) The exchange interaction is very nearly diagonal. The only non-diagonal terms are between yellow and green Γ_5 excitons of the same symmetry; ($G\Gamma^5_{yz}$ and $Y\Gamma^5_{yz}$, $G\Gamma^5_{xz}$ and $Y\Gamma^5_{xz}$, $G\Gamma^5_{xy}$ and $Y\Gamma^5_{xy}$).

(2) The sole effect of the hydrostatic deformation term hX is to shift all the diagonal energies linearly.

(3) Terms linear in eX occur in the diagonal elements of the green excitons giving rise to linear splitting due to splitting of the Γ_8 valence band. However, no such terms occur in the energies of the yellow excitons (E_5, E_8, E_{10}, E_{12}) showing that these states are not split by the strain to first order. Splittings must therefore come about in second order due to the non-diagonal matrix elements of eX between yellow and green states.

(4) The matrix only includes yellow and green excitons of a particular orbital quantum state (e.g., 3S). No interactions between states of different quantum numbers have been included, nor have possible interactions with other valence or conduction.bands, such as the blue or violet exciton series.

The Hamiltonian matrix can be diagonalized numerically for different values of the parameters and compared directly with the experimental data. However, it is useful first to solve approximately for the energy eigenvalues using second-order perturbation theory

$$E_n = H^o_{nn} + H'_{nn} + \sum_{k \neq n} \frac{|H_{nk}|^2}{E^o_n - E^o_k} \qquad (3\text{-}64)$$

Since ϕ_3 and ϕ_4 are degenerate in H_0, the exchange part of H' has also been included in the energy denominator for this pair (i.e., $E_3{}^0 - E_4{}^0 = 4J_g/3$) and similarly for ϕ_6 and ϕ_7. Finally, the yellow exciton Coulomb energy E_c^y was subtracted from the resulting energy eigenvalues and the combination $\Delta + E_c{}^g - E_c{}^y$ represented by Δ' (which now depends on the particular exciton state). The final energies shown in Table 3-12 are thus measured from the energy of the specific yellow exciton without exchange and strain.

Note that the yellow triplet orthoexciton is thus predicted to split into a doublet and a singlet under applied uniaxial stress. This was shown schematically in Fig. 3-3. The linear splitting term comes from the cross term in the squared off-diagonal matrix element $\left[\frac{4J}{3\sqrt{2}} + \frac{eX}{\sqrt{2}}\right]$ and is thus seen to arise from the simultaneous effects of exchange and strain as stated earlier.

2. Rhombohedral Stress

The rhombohedral stress is applied along [110] . It is of lower symmetry than the tetragonal stress and is capable of splitting the ${}^3\Gamma_5^+$ exciton into three nondegenerate levels as discussed in Section F.3 and summarized in Fig. 3-3.

TABLE 3-11

Matrix of the effective Hamiltonian $H = H^0 + H'$ in the 12-state basis of Table 3-2

$H^0 = \Delta + E_c$; $H' = \frac{1}{2}J_{ij}\vec{\sigma}_e\cdot\vec{\sigma}_h + hX + e\left(L_z^2 - \frac{1}{3}L^2\right)X$ (Tetragonal stress)

	ϕ_1 green $\Gamma_4(z)$	ϕ_2 green Γ_3	ϕ_3 green $\Gamma_4(x)$	ϕ_4 green $\Gamma_5(yz)$	ϕ_5 yellow $\Gamma_5(yz)$
ϕ_1	$\Delta + E_c^g + \frac{1}{2}J_g + hX - eX$	0	0	0	0
ϕ_2	0	$\Delta + E_c^g + \frac{1}{2}J_g + hX - eX$	0	0	0
ϕ_3	0	0	$\Delta + E_c^g + \frac{1}{2}J_g + hX + \frac{1}{2}eX$	$-\frac{\sqrt{3}}{2}eX$	$-\sqrt{\frac{3}{2}}\,eX$
ϕ_4	0	0	$-\frac{\sqrt{3}}{2}\,eX$	$\Delta + E_c^g - \frac{5}{6}J_g + hX - \frac{1}{2}eX$	$\frac{4J}{3\sqrt{2}} + \frac{eX}{\sqrt{2}}$
ϕ_5	0	0	$-\sqrt{\frac{3}{2}}\,eX$	$\frac{4J}{3\sqrt{2}} + \frac{eX}{\sqrt{2}}$	$E_c^y - \frac{1}{6}J_y + hX$
ϕ_6	0	0	0	0	0
ϕ_7	0	0	0	0	0
ϕ_8	0	0	0	0	0
ϕ_9	0	0	0	0	0
ϕ_{10}	0	0	0	0	0
ϕ_{11}	0	0	0	0	0
ϕ_{12}	0	0	0	0	0

TABLE 3-11 Continued

ϕ_6 green $\Gamma_4(y)$	ϕ_7 green $\Gamma_5(xz)$	ϕ_8 yellow $\Gamma_5(xz)$	ϕ_9 green $\Gamma_5(xy)$	ϕ_{10} yellow $\Gamma_5(xy)$	ϕ_{11} green Γ_3	ϕ_{12} yellow Γ_3	
0	0	0	0	0	0	0	ϕ_1
0	0	0	0	0	0	0	ϕ_2
0	0	0	0	0	0	0	ϕ_3
0	0	0	0	0	0	0	ϕ_4
0	0	0	0	0	0	0	ϕ_5
$\Delta + E_c^g + \frac{1}{2}J_g + hX + \frac{1}{2}eX$	$\frac{\sqrt{3}}{2}\, eX$	$\sqrt{\frac{3}{2}}\, eX$	0	0	0	0	ϕ_6
$\frac{\sqrt{3}}{2}\, eX$	$\Delta + E_c^g - \frac{5}{6}J_g + hX - \frac{1}{2}eX$	$\frac{4J}{3\sqrt{2}} + \frac{eX}{\sqrt{2}}$	0	0	0	0	ϕ_7
$\sqrt{\frac{3}{2}}\, eX$	$\frac{4J}{3\sqrt{2}} + \frac{eX}{\sqrt{2}}$	$E_c^y - \frac{1}{6}J_y + hX$	0	0	0	0	ϕ_8
0	0	0	$\Delta + E_c^g - \frac{5}{6}J_g + hX + eX$	$\frac{4J}{3\sqrt{2}} - e\sqrt{2}X$	0	0	ϕ_9
0	0	0	$\frac{4J}{3\sqrt{2}} - e\sqrt{2}X$	$E_c^y - \frac{1}{6}J_y + hX$	0	0	ϕ_{10}
0	0	0	0	0	$\Delta + E_c^g + \frac{1}{2}J_g + hX + eX$	$-\sqrt{2}\, eX$	ϕ_{11}
0	0	0	0	0	$-\sqrt{2}\, eX$	$E_c^y + \frac{1}{2}J_y + hX$	ϕ_{12}

TABLE 3-12

Eigenvalues of the energy matrix (Table 3-11) from second-order perturbation theory (tetragonal stress)

<u>Energy</u> ($\underline{O_h}$ <u>Symmetry</u> // $\underline{D_{4h}}$ <u>Symmetry</u>)

Yellow Γ_5 Triplet Orthoexciton

$$E_{\phi_5} = E_{\phi_8} = -\frac{1}{6}Jy - \frac{8J^2}{9\Delta'} + hX - \frac{4eJX}{3\Delta'} - \frac{2e^2}{\Delta'}X^2 \qquad (\Gamma_{5_{yz}}, \Gamma_{5_{xz}} \,//\, {}^2\Gamma_5^+)$$

$$E_{\phi_{10}} = -\frac{1}{6}Jy - \frac{8J^2}{9\Delta'} + hX + \frac{8eJX}{3\Delta'} - \frac{2e^2X^2}{\Delta'} \qquad (\Gamma_{5_{xy}} \,//\, {}^1\Gamma_4^+)$$

Yellow Γ_2 Singlet Paraexciton

$$E_{\phi_{12}} = \tfrac{1}{2}Jy + hX - \frac{2e^2X^2}{\Delta'}$$

Green Γ_5 Triplet

$$E_{\phi_7} = E_{\phi_4} = \Delta' - \frac{5}{6}Jg + \frac{8J^2}{9\Delta'} + hX + \left(\frac{4J}{3\Delta'} - \frac{1}{2}\right)eX + \left(\frac{1}{2\Delta'} - \frac{9}{16J_g}\right)e^2X^2$$

$$(\Gamma_{5_{yz}}, \Gamma_{5_{xz}} \,//\, {}^2\Gamma_5^+)$$

$$E_{\phi_9} = \Delta' - \frac{5}{6}Jg + \frac{8J^2}{9\Delta'} + hX - \left(\frac{8J}{3\Delta'} - 1\right)eX + \frac{2e^2X^2}{\Delta'}$$

$$(\Gamma_{5_{xy}} \,//\, {}^1\Gamma_4^+)$$

Green Γ_4 Triplet

$$E_{\phi_3} = E_{\phi_6} = \Delta' + \tfrac{1}{2}Jg + hX + \tfrac{1}{2}eX + \left(\frac{9}{16Jg} + \frac{3}{2\Delta'}\right)e^2X^2$$

$$E_{\phi_1} = \Delta' + \tfrac{1}{2}Jg + hX + eX \qquad (\Gamma_{4_z} \,//\, {}^1\Gamma_2) \qquad (\Gamma_{4_x}, \Gamma_{4_y} \,//\, {}^2\Gamma_5)$$

Green Γ_3 Doublet

$$E = \Delta' + \tfrac{1}{2}Jg + hX - eX$$

$$E = \Delta' + \tfrac{1}{2}Jg + hX + eX + \frac{2e^2X^2}{\Delta'}$$

The effective Hamiltonian for this case differs from that of the last section only in the deformation part which now becomes

$$H_{D_{110}} = hX - \frac{e}{2}(L_z^2 - L^2/3)X + f(L_xL_y + L_yL_x)X \qquad (3\text{-}65)$$

as was shown in Section F.1. Eq. (3-65) involves an additional deformation parameter (f) that did not occur in Eq. (3-59) for the tetragonal case.

Although the only formal difference between the tetragonal and rhombohedral cases involves the deformation Hamiltonian, it is desirable to proceed with the present calculation using a different linear combination of the exciton basis functions given in Table 3-2.

For stress parallel to [110] , the crystal is not uniaxial as it was for tetragonal stress[72]. The stress couples the valence bands which leads to a breakdown of m_j as a good quantum number (Table 3-1). The unperturbed exciton basis functions of Table 3-2 would be mixed by the stress. This mixing can be seen by comparing the first and third columns of Table 3-10 which give the representations appropriate to basis functions in the unstressed and the rhombohedrally-stressed crystal. It is also seen that the mixing will not occur if the unperturbed (O_h) basis functions are chosen so that functions transforming as x and y are replaced by their symmetric and antisymmetric combinations and similarly for functions transforming as yz and zx.

The linear combinations to be used as basis functions for the calculation for rhombohedral stress are given in Table 3-13. The matrix of the effective Hamiltonian in the 12 state basis of Table 3-13 is given in Table 3-14. The comments of the last section concerning the unperturbed eigenvalues apply here as well.

Approximate energy eigenvalues can again be determined using second-order perturbation theory. The results are shown in Table 3-15. In contrast to the tetragonal case, the yellow triplet orthoexciton is now predicted to split into three distinct levels. This result was anticipated by the group-theoretical arguments of Sections F.3 and F.4.

TABLE 3-13

Exciton Wavefunctions for Rhombohedral Stress (in terms of wavefunctions of Table 3-2)

$\psi_1 = -\phi_1$

$\psi_2 = \phi_2$

$\psi_3 = \frac{1}{\sqrt{2}}(\phi_3 + \phi_6)$

$\psi_4 = -\frac{1}{\sqrt{2}}(\phi_4 + \phi_7)$

$\psi_5 = -\frac{1}{\sqrt{2}}(\phi_5 + \phi_8)$

$\psi_6 = \frac{1}{\sqrt{2}}(\phi_3 - \phi_6)$

$\psi_7 = \frac{1}{\sqrt{2}}(\phi_4 - \phi_7)$

$\psi_8 = \frac{1}{\sqrt{2}}(\phi_5 - \phi_8)$

$\psi_9 = \phi_9$

$\psi_{10} = \phi_{10}$

$\psi_{11} = \phi_{11}$

$\psi_{12} = \phi_{12}$

TABLE 3-14

Matrix of the effective Hamiltonian $H = H^{o} + H'$ in the 12-state basis of Table 3-13

$H^{o} = \Delta + E_c$; $H' = \frac{1}{2}J_{ij}\vec{\sigma}_e\cdot\vec{\sigma}_h + hX - \frac{1}{2}e\left(L_z^2 - \frac{1}{3}L^2\right)X + f\left(L_xL_y + L_yL_x\right)X$ (Rhombohedral stress)

	ψ_1	ψ_2	ψ_3	ψ_4	ψ_5	ψ_6
ψ_1	$\Delta + E_c^g + \frac{1}{2}J_g + hX + \frac{1}{2}eX$	0	0	0	0	0
ψ_2	0	$\Delta + E_c^g + \frac{1}{2}J_g + hX + \frac{1}{2}eX$	0	0	0	0
ψ_3	0	0	$\Delta + E_c^g + \frac{1}{2}J_g + hX - \frac{1}{4}eX - \frac{3}{2}fX$	0	$-\frac{\sqrt{6}}{8}fX$	0
ψ_4	0	0	0	$\Delta + E_c^g - \frac{5}{6}J_g + hX + \frac{1}{4}eX - \frac{3}{2}fX$	$\frac{4J}{3\sqrt{2}} - \frac{eX}{2\sqrt{2}} + \frac{3fX}{2\sqrt{2}}$	$-\frac{\sqrt{3}eX}{4} - \frac{\sqrt{3}fX}{2}$
ψ_5	0	0	$-\frac{\sqrt{6}}{8}fX$	$\frac{4J}{3\sqrt{2}} - \frac{eX}{2\sqrt{2}} + \frac{3fX}{2\sqrt{2}}$	$E_c^y - \frac{1}{6}J_y + hX$	$-\frac{\sqrt{3}eX}{2\sqrt{2}} - \frac{3\sqrt{6}fX}{8}$
ψ_6	0	0	0	$-\frac{\sqrt{3}eX}{4} - \frac{\sqrt{3}fX}{2}$	$-\frac{\sqrt{3}eX}{2\sqrt{2}} - \frac{3\sqrt{6}fX}{8}$	$\Delta + E_c^g + \frac{1}{2}J_g + hX - \frac{1}{4}eX + \frac{3}{2}fX$
ψ_7	0	0	$\frac{\sqrt{3}eX}{4} - \frac{\sqrt{3}fX}{2}$	0	0	0
ψ_8	0	0	$\frac{\sqrt{3}eX}{2\sqrt{2}} - \frac{3\sqrt{6}fX}{8}$	0	0	$\frac{\sqrt{6}fX}{8}$
ψ_9	0	$\sqrt{3}fX$	0	0	0	0
ψ_{10}	0	$\sqrt{6}fX$	0	0	0	0
ψ_{11}	$-\sqrt{3}fX$	0	0	0	0	0
ψ_{12}	$\sqrt{6}fX$	0	0	0	0	0

TABLE 3-14 Continued

	ψ_7	ψ_8	ψ_9	ψ_{10}	ψ_{11}	ψ_{12}
ψ_1	0	0	0	0	$-\sqrt{3}fX$	$\sqrt{6}fX$
ψ_2	0	0	$\sqrt{3}fX$	$\sqrt{6}fX$	0	0
ψ_3	$\frac{\sqrt{3}eX}{4}-\frac{\sqrt{3}fX}{2}$	$\frac{\sqrt{3}eX}{2\sqrt{2}}-\frac{3\sqrt{6}fX}{8}$	0	0	0	0
ψ_4	0	0	0	0	0	0
ψ_5	0	0	0	0	0	0
ψ_6	0	$\frac{\sqrt{6}fX}{8}$	0	0	0	0
ψ_7	$\Delta+E_c^g-\frac{5}{6}J_g+hX$ $+\frac{1}{4}eX+\frac{3}{2}fX$	$\frac{4J}{3\sqrt{2}}-\frac{eX}{2\sqrt{2}}-\frac{3fX}{2\sqrt{2}}$	0	0	0	0
ψ_8	$\frac{4J}{3\sqrt{2}}-\frac{eX}{2\sqrt{2}}-\frac{3fX}{2\sqrt{2}}$	$E_c^y-\frac{1}{6}J_y+hX$	0	0	0	0
ψ_9	0	0	$\Delta+E_c^g-\frac{5}{6}J_g$ $+hX-\frac{1}{2}eX$	$\frac{4J}{3\sqrt{2}}+\frac{1}{\sqrt{2}}eX$	0	0
ψ_{10}	0	0	$\frac{4J}{3\sqrt{2}}+\frac{1}{\sqrt{2}}eX$	$E_c^y-\frac{1}{6}J_y+hX$	0	0
ψ_{11}	0	0	0	0	$\Delta+E_c^g+\frac{1}{2}J_g$ $+hX-\frac{1}{2}eX$	$\frac{1}{\sqrt{2}}eX$
ψ_{12}	0	0	0	0	$\frac{1}{\sqrt{2}}eX$	$E_c^y+\frac{1}{2}J_y+hX$

TABLE 3-15

Eigenvalues of the energy matrix (Table 3-14) from second-order perturbation theory (rhombohedral stress)

Yellow Γ_5 Triplet Orthoexciton

$$\Gamma_3'(C_{2v}):\ E_{\psi_5} = -\frac{1}{6}Jy - \frac{8J^2}{9\Delta'} + hX + \left(\frac{2eJ}{3\Delta'} - \frac{2fJ}{\Delta'}\right)X - \left(\frac{e^2}{2\Delta'} + \frac{33f^2}{16\Delta'} + \frac{3ef}{8\Delta'}\right)X^2$$

$$\Gamma_4'(C_{2v}):\ E_{\psi_8} = -\frac{1}{6}Jy - \frac{8J^2}{9\Delta'} + hX + \left(\frac{2eJ}{3\Delta'} + \frac{2fJ}{\Delta'}\right)X - \left(\frac{e^2}{2\Delta'} + \frac{33f^2}{16\Delta'} - \frac{3ef}{8\Delta'}\right)X^2$$

$$\Gamma_1'(C_{2v}):\ E_{\psi_{10}} = -\frac{1}{6}Jy - \frac{8J^2}{9\Delta'} + hX - \frac{4eJ}{3\Delta'}X - \left(\frac{e^2}{2\Delta'} + \frac{6f^2}{\Delta'}\right)X^2$$

Yellow Γ_2 Singlet Paraexciton

$$E_{\psi_{12}} = \tfrac{1}{2}Jy + hX - \left(\frac{e^2}{2\Delta'} + \frac{6f^2}{\Delta'}\right)X^2$$

Green Γ_5 Triplet

$$E_{\psi_4} = \Delta' - \frac{5}{6}Jg + \frac{8J^2}{9\Delta'} + hX + \left(\frac{1}{4}e - \frac{3}{2}f - \frac{2eJ}{3\Delta'} + \frac{2fJ}{\Delta'} - \frac{3ef}{4\Delta}\right)X + \left(\frac{e^2}{8\Delta'} + \frac{9f^2}{8\Delta'} - \frac{9e^2}{64Jg} - \frac{9f^2}{16Jg} - \frac{9ef}{16Jg}\right)X^2$$

$$E_{\psi_7} = \Delta' - \frac{5}{6}Jg + \frac{8J^2}{9\Delta'} + hX + \left(\frac{1}{4}e + \frac{3}{2}f - \frac{2eJ}{3\Delta'} - \frac{2fJ}{\Delta'} + \frac{3ef}{4\Delta'}\right)X + \left(\frac{e^2}{8\Delta'} + \frac{9f^2}{8\Delta'} - \frac{9e^2}{64Jg} - \frac{9f^2}{16Jg} + \frac{9ef}{16Jg}\right)X^2$$

$$E_{\psi_9} = \Delta' - \frac{5}{6}Jg + \frac{8J^2}{9\Delta'} + hX + \left(\frac{4eJ}{3\Delta'} - \frac{1}{2}e\right)X + \left(\frac{e^2}{2\Delta'} - \frac{4f^2}{Jg}\right)X^2$$

TABLE 3-15 Continued

Green Γ_4 Triplet

$$E_{\psi_3} = \Delta' + \frac{1}{2}Jg + hX - \frac{1}{4}eX - \frac{3}{2}fX + \left(\frac{3e^2}{8\Delta'} - \frac{9ef}{8\Delta'} + \frac{15f^2}{16\Delta'} + \frac{9e^2}{64Jg} - \frac{9ef}{16Jg} + \frac{9f^2}{16Jg}\right)X^2$$

$$E_{\psi_6} = \Delta' + \frac{1}{2}Jg + hX - \frac{1}{4}eX + \frac{3}{2}fX + \left(\frac{3e^2}{8\Delta'} + \frac{9ef}{8\Delta'} + \frac{15f^2}{16\Delta'} + \frac{9e^2}{64Jg} + \frac{9ef}{16Jg} + \frac{9f^2}{16Jg}\right)X^2$$

$$E_{\psi_1} = \Delta' + \frac{1}{2}Jg + hX + \frac{1}{2}eX + \sqrt{3}fX + \frac{6f^2}{\Delta'}X^2$$

Green Γ_3 Doublet

$$E_{\psi_{11}} = \Delta' + \frac{1}{2}Jg + hX - \frac{1}{2}eX - \sqrt{3}fX + \frac{e^2}{2\Delta'}X^2$$

$$E_{\psi_2} = \Delta' + \frac{1}{2}Jg + hX + \frac{1}{2}eX + \frac{6f^2X^2}{\Delta'} + \frac{9f^2X^2}{4Jg}$$

CHAPTER IV.

EXPERIMENT

A. Introduction

Laser Raman spectroscopy involves the following experimental arrangement. A beam of laser light is focussed into a small volume of the sample to be studied. Light scattered from the sample contains a number of frequency components. This scattered light is collected and frequency analyzed with a tandem grating spectrometer. Elastic scattering produces the most intense component which is centered at the frequency of the laser light. Inelastic components occur at frequencies shifted with respect to the laser frequency. These result from interactions with various excitations of the sample. Of interest in Raman scattering experiments are the frequency shifts and the intensities of the shifted components.

B. Experimental Setup

The experimental arrangement used in the present study is shown in Fig. 4-1. An Argon ion laser was used to pump a cw dye laser in order to obtain tunable output radiation. The output of the dye laser, was passed through a single-grating spectrometer to reduce the intensity of the broad-band background fluorescence which accompanies the main output frequency of the dye laser. The light was then passed through a polarization rotator to obtain the desired polarization before being focussed onto the sample. The sample was mounted in a stress apparatus which in turn was mounted in a helium dewar. The sample was cut, polished and mounted to permit application of stress along the desired direction while allowing a light scattering geometry appropriate to the symmetry of the strained crystal. The latter involves conditions upon the wavevector and polarization components of the incident and scattered light with respect to the crystallographic axes. The conditions are determined from group theoretical considerations. Typical sample dimensions were 1mm x 1mm x 10mm. Light scattered by the sample was collected by a collimating lens. The parallel light so obtained was reflected from a system of two mirrors. This arrangement served the dual purpose of aligning the collected light with the spectrometer and rendering the image of the scattering plane parallel to the spectrometer slits. The light reflected from the mirrors was then focussed onto the spectrometer slits. The speed of the lens used was chosen to match that of the spectrometer. A polarization analyzer and a polarization scrambler were placed in front of the spectrometer entrance slit. The scrambler was used to compensate for the dependence of spectrometer throughput on the polarization of incident light.

Light leaving the spectrometer was focussed onto the cathode of a photomultiplier tube whose output was processed with photon counting electronics and recorded on a stripchart recorder. The stripchart record provided a curve of the intensity of scattered light as a function of frequency.

C. Apparatus

A summary of the apparatus used in these experiments is given in Table 4-1. Brief descriptions of the main components follow.

Argon Laser

A Spectra Physics model 165 Argon ion laser was used as pump laser in all experiments. The output was approximately 3.5 watts in all lines.

Dye Laser

The output of the Argon laser was used to pump a Coherent Radiation model 590 dye laser to obtain a source of continuously tunable coherent light. The dye medium was a methyl alcohol solution of the dye rhodamine 6G, which absorbs in the band 4800 A to 5300 A and emits at longer wavelengths 5400 A to 6300 A through fluorescence. Selection of monochromatic radiation from the broad dye fluorescence bandwidth is achieved through the use of a quartz birefringent filter consisting of three quartz plates of different thicknesses placed in the cavity at Brewster's angle. The resultant "monochromatic" output has a width of about 1.5 cm^{-1}. Tuning of the output frequency is accomplished by rotating the birefringent filter about the surface normal.

The filter can be rotated by using a system in which the linear travel of a micrometer barrel is transferred to angular travel of the birefringent filter mount. An improved tuning procedure was developed. This involved

FIG. 4-1. Schematic of experimental arrangement. L_1, L_2 and L_3 are sample focussing, sample collecting and spectrometer focussing lenses respectively. Focal lengths of these lenses were 6 cm, 8.5 cm and 20.9 cm, respectively.

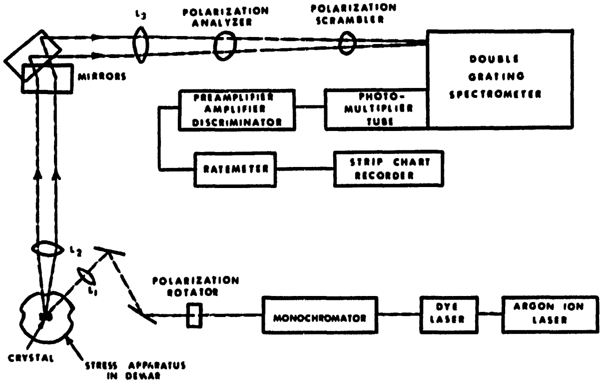
L3
POLARIZATION ANALYZER
POLARIZATION SCRAMBLER
DOUBLE GRATING SPECTROMETER
MIRRORS
PREAMPLIFIER AMPLIFIER DISCRIMINATOR
PHOTO-MULTIPLIER TUBE
RATEMETER
STRIP CHART RECORDER
L2
L1
POLARIZATION ROTATOR
MONOCHROMATOR
DYE LASER
ARGON ION LASER
CRYSTAL
STRESS APPARATUS IN DEWAR

mechanical coupling of the micrometer shaft to a synchronous stepping motor (Superior Electric, Co. model M062-FD03). Through the use of an oscillator and other external circuitry, it was possible to control the stepping rate as well as the total number of pulses (steps) delivered to the motor. This arrangement was convenient in that the laser tuning could be controlled from a panel also containing other controls. The method was also versatile in that it permitted choosing between rapid coarse tuning or precision tuning. These correspond to tuning between spectral ranges well separated in frequency (for probing different exciton states) and tuning through a small spectral range (for studying a particular state) respectively. The precision in the tuning allowed tuning the dye laser in increments of about 1.5 cm^{-1} with a repeatability of 0.1 cm^{-1}.

Monochromator

Reduction of the fluorescence background was accomplished by passing the dye laser beam through a small single-grating spectrometer (Spex "Minimate", model 1670). A 4 cm focal length cylindrical lens was used to elongate the beam so that most of the light would pass through a 0.5 mm wide entrance slit. Another cylindrical lens was placed after the 0.5 mm exit slit to obtain collimated light. The throughput of this spectrometer was about 30%. This resulted in the about 40 mw of dye laser power at the sample. The tuning drive was coupled to a stepping motor which permitted convenient tuning of the spectrometer

TABLE 4-1. LIST OF APPARATUS

Apparatus	Manufacturer	Model
Argon Laser	Spectra Physics	165
Dye Laser	Coherent Radiation	590
Single-grating spectrometer	Spex	1670
Polarization rotator	Spectra Physics	310
Helium Dewar	Janis	Supervaritemp Model 8DT
Ge thermometer	Scientific Instruments	2
Stress Apparatus	Homemade by F. Pollak	
Stepping motors	Superior Electric	M062-FD03
Polarization analyzer	Spex	1430-2
Polarization scrambler	Spex	1430-1C
Double-grating spectrometer	Spex	1401
Photomultiplier tube	ITT	FW130
Refrigeration unit for P.M. tube	Products for Research	TE-104
Power supply	Power Designs, Inc.	AK-20
Nim Bin	Berkeley Nucleonics	AP.1
Preamplifier, Amplifier, Discriminator	Canberra	813
Ratemeter	Ortec	441
Stripchart recorder	Honeywell	194

whenever the laser was tuned.

Stress Apparatus

The stress apparatus, designed by F. H. Pollak[44], was of a type that has been used in similar experiments for a number of years. The sample, of millimeter dimensions, was prepared so that the long dimension (~ 1 cm) corresponded to the intended stress direction. The sample ends were ground flat, parallel to each other and normal to the long dimension. The ends were epoxied into mounts made of beryllium copper. One of the mounts was rigidly affixed to the stress frame (to be described) while the other was seated inside a cylindrical sleeve which could move relative to the stress frame. This sleeve was attached to a pullrod. Tension on the pullrod resulted in compression on the sample by virtue of the arrangement described above. The sleeve was designed to slide over guides - both parts being machined to high tolerance to insure parallelism between the applied force and the sample.

The upper end of the pullrod was mechanically coupled to a stiff spring through a lever arrangement shown in Fig. 4-2. The spring was physically attached to a threaded shaft. Force was applied by manually turning the shaft with respect to a matching female thread. As the shaft was screwed into the threaded part, the spring became elongated ultimately producing compression at the sample. The applied force was measured by determining the elongation of the spring. This was done by using two linear differential voltage transformers (LDVT). An a.c. voltage applied to the primary of either of these produces a voltage in the secondary which depends on the overlap between the coils. One LDVT was mounted so that the position of the secondary relative to the primary was determined by the spring elongation. The other LDVT allowed manual adjustment of the secondary with respect to the primary. A common a.c. voltage was applied to both primaries while the voltages on the secondaries served as input to a bridge circuit. For a given spring elongation, the secondary on the external LDVT was varied until its output voltage matched that of the secondary on the LDVT attached to the spring. This condition was indicated as a null reading on a voltmeter which measured the output of the bridge. The amount of overlap between primary and secondary of the external LDVT (which is equal to the amount of spring elongation) was then read directly from a micrometer barrel attached to the secondary. The spring constant had been determined previously. With this information and the measured cross-sectional area of the sample, the applied stress could be calculated.

The method outlined above allowed determination of the spring elongation to within 0.010". This accuracy in combination with the 5% accuracy in the determination of the sample area, limited the accuracy of measurement of the applied stress to 10% at 0.2 Kbar and 2% at 1.0 Kbar.

The stress apparatus was designed to adapt to the

FIG. 4-2. Uniaxial Stress Apparatus

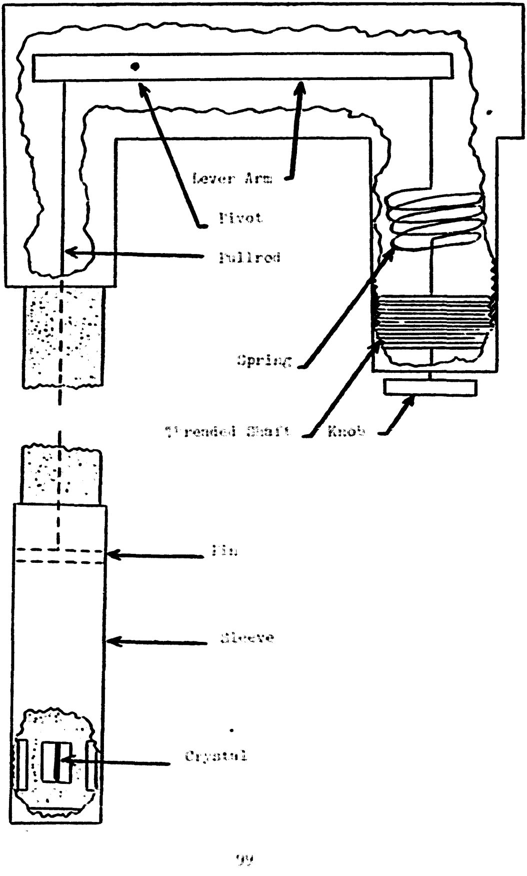
Lever Arm
Pivot
Pullrod
Spring
Threaded Shaft
Knob
Pin
Sleeve
Crystal

dewar described below.

Cryogenic System

With the sample in place, the stress rig was placed in a Janis "Supervaritemp" liquid helium dewar (model 8 DT). Optical access to the sample was provided by fused quartz windows on the dewar and by cutouts on the stress rig. Cooling of the sample was achieved by liquid helium flow over the copper sample mounts and by conduction between the sample and the mounts. Temperature was measured using a germanium resistance thermometer (Scientific Instruments, model 2) which was in thermal contact with the sample mounts. All experiments were performed at ~ 4°K.

Double Grating Spectrometer

Light scattered from the crystal was analyzed using a 3/4 meter Spex model 1401 Czerny-Turner double grating spectrometer, which functioned as a filter of extremely high contrast. The tandem feature was required to prevent the internally scattered intense Rayleigh light from masking the weak Raman components.

Photomultiplier Tube

The light leaving the spectrometer was focussed onto the cathode of an ITT FW130 photomultiplier tube. The tube was maintained at -20° C by a model TE-104 thermoelectric refrigeration unit manufactured by Products for Research. The dark count of the cooled tube was about 3 counts/second. A Power Designs, Inc. model AK-20 power supply provided 1700 volts to the photomultiplier tube.

Photon-Counting Electronics

The photon-counting electronics comprised a "PAD" (Canberra, model 813) which combines a preamplifier, amplifier and discriminator in a single nim bin module. The output of the discriminator was fed to a ratemeter (Ortec, model 441)and recorded on a stripchart recorder (Honeywell, model 194).

D. Experimental Procedure

The experiments conducted in this *program* were of two kinds. The first involved measurements of first order Raman intensity as a function of laser frequency in the region of the yellow exciton series. The other involved comparison of scattering intensities for several polarization configurations with the laser tuned to a particular frequency.

The Raman measurements were carried out in the following way. The dye laser was tuned to a frequency near but below a known exciton state of Cu_2O. A precise measurement of the laser frequency was obtained by scanning the spectrometer at a slow speed over the elastic component of the light scattered from the crystal. The slow scan (15 $cm^{-1}min^{-1}$) allowed the experimenter to mark the stripchart record in 1 cm^{-1} intervals by visual comparison with the spectrometer wavenumber indicator. (Although the spectrometer had a built-in wavenumber marker, the standard 10 cm^{-1} intervals that it marks were too coarse for the precision required). Subsequent interpolation between the

1 cm^{-1} marks (during data analysis) allowed the laser frequency to be determined to the nearest 0.1 cm^{-1}. Measurements made in this way were reproduceable to better than 0.4 cm^{-1}. Due to the lack of precision temperature control with the consequent drift in the spectrometer calibration, it was necessary to follow each scan over the Rayleigh line with a scan over a Hg calibration line. Once the laser frequency was measured, the spectrometer was set at a frequency about 100 cm^{-1} below the laser frequency. The spectrometer was then set to scan (towards lower frequency) a range of about 20 cm^{-1}. This range included the 109 cm^{-1} (Γ_3^-) phonon. The dye laser and monochromator were then tuned 3 cm^{-1} higher using the stepping motor arrangement. The laser frequency was not directly measured at this point. The spectrometer was reset to scan over the Γ_3^- Raman feature again. This process of tuning and scanning was repeated until an enhancement of the Γ_3^- feature was observed. The process was continued with the tuning increments reduced to about 1.5 cm^{-1}. At each setting of the incident frequency, the spectrometer scan over the Γ_3^- feature produced an intensity vs frequency curve centered 109 cm^{-1} below the laser frequency. The intensity of the Raman feature grew and then decreased as the laser was tuned through the exciton state. Tuning ended, when the laser was well away from resonance. At this point, precision scans over the Rayleigh line and the Hg line were again carried out as described above. This served as a check on the mechanical

tuning procedure. The total tuning range of the laser while studying each exciton state was about 10 cm^{-1}.

The results for a particular state, as obtained on the stripchart recorder, are shown in Fig. 4-3. The Raman features shown are all centered 109 cm^{-1} below the dye laser frequency and correspond to the Raman scattered light from the Γ_1^- phonon. The Raman feature to the extreme left is an intensity vs frequency curve of light scattered from the sample obtained by scanning the spectrometer over a frequency range from 100 to 120 cm^{-1} below the laser frequency with the latter held fixed. Following this scan, the dye laser and monochromator were tuned 1.5 cm^{-1} higher, using stepping motors, and the scattered light was scanned over again with the scan beginning 1.5 cm^{-1} higher (i.e. the spectrometer was made to "follow" the dye laser frequency so as to always yield scans centered 109 cm^{-1} below the laser as the laser was tuned). This second scan is shown as the second feature in the figure. The growth in intensity is apparent. The remaining five Raman features in the figure resulted from continuing this process of tuning and scanning. The features in Fig. 4-3, therefore, are all scans over the scattered light and are all centered 109 cm^{-1} below the laser frequency. Each feature, however, involves incident laser light at a frequency 1.5 cm^{-1} higher than for the previous feature.

The frequency of the dye laser for the first and last features was measured by scanning over the Rayleigh scattered light and the Hg calibration line as described above. These scans are not shown. The laser frequency for the other features was obtained from the Rayleigh measurements and from the assumption of equal tuning increments. This was verified by using the stepping motor calibration which had been done prior to the experiment. The calibration gives the increment in laser frequency that results from application of a given number of pulses to the stepping motors.

According to the theory of Chapter III, the most intense Raman scattering should occur when the laser is exactly in resonance with an exciton state. Since the experiments were done with tuning in discrete steps, however, the following was found to be a convenient way of establishing the energy of the exciton state associated with the resonant enhancement. Associated with each Raman feature in Fig. 4-3 is an intensity (as shown on the vertical scale) and a dye laser frequency (determined as discussed above). This information can be used to construct a plot of incident laser frequency vs Raman intensity wherein the "features" are represented by points. A smooth curve drawn through the points may be bisected in order to yield an estimate of the energy of the exciton state. Five examples of such curves (for the 1S state) are shown in Fig. 5-1.

After an exciton state had been studied as described above, the laser and monochromator were coarsely tuned to a frequency near the next exciton state to be studied and the

FIG. 4-3. Stripchart recorder output for resonant Raman scattering from the 109 cm^{-1} phonon. The results are for a Cu_2O crystal with stress (2.2 Kbar) applied parallel to 110 and with the dye laser tuned through the 4S state of the yellow exciton series. Each Raman feature (centered 109 cm^{-1} below the laser frequency) results from Raman scattering with the incident frequency 1.5 cm^{-1} higher than for the feature to its left as discussed in the text. The incident light was polarized parallel to 110 while the scattered light was unpolarized. The laser frequency for the first (last) feature was 17445.6 cm^{-1} (17454.8 cm^{-1}).

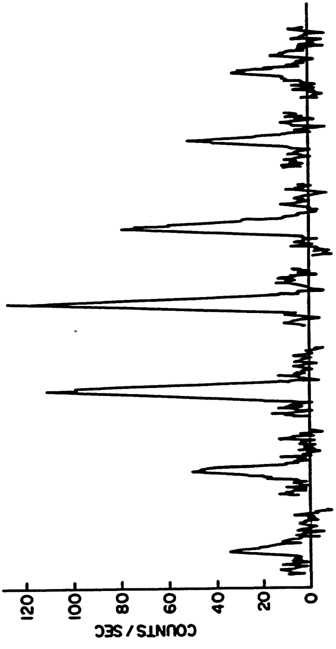
COUNTS / SEC
0
20
40
60
80
100
120

FIG. 4-4. Polarization study of Raman-scattered light with the dye laser tuned to the frequency of the high-energy stress-split component of the 4S state of the yellow exciton series (the same state responsible for the enhancement in Fig. 4-3). Backscattering was from [001] (x_2) and the stress was rhombohedral. The polarization of incident and scattered light is indicated on the figure. Each feature is a frequency scan over the 109 cm^{-1} phonon. The ordinate and abscissa correspond to intensity and frequency respectively, and the noise level is shown as a dashed line. Comparison with Table 3-8 shows that the state has Γ_4 symmetry.

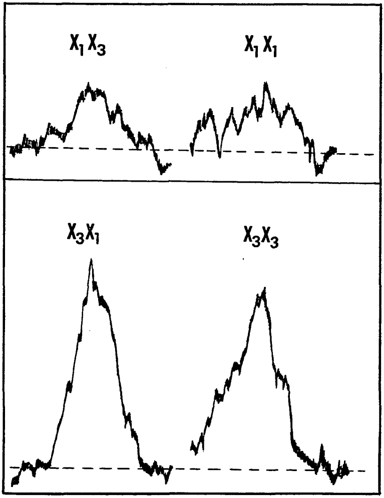
X1 X3
X1 X1
X3X1
X3X3

entire procedure of laser frequency measurement followed by tuning and scanning followed by laser frequency measurement was repeated.

The above discussion applies to studies of features in the spectral region of the excited states of the yellow exciton. The same technique was applied in studying the 1S state of the yellow exciton except that, due to its width, the tuning increments and tuning widths were halved.

It must also be mentioned that in this part of the experiment the polarization analyzer and polarization scrambler were not used and the polarization rotator was used only when necessary to rotate the polarization vector of the incident laser light to satisfy the selection rules derived in the theory section. These elements were used only when needed to establish polarization selection rules. The important consideration for the experiments under discussion was signal optimization which benefitted from the absence of unnecessary optics.

The experiment as described so far has been for measurements of enhancements in the Raman intensity with the laser tuned to exciton states of interest. Conducting experiments on the strained crystal involved repetition of the above measurements for the relevant states with stress applied and measured as previously described. The result of the induced strain was to produce a splitting of the exciton states in most cases. That is to say that tuning the laser produced several enhancements of the Γ_3^- feature in place of the single feature observed in the unstrained crystal. The several new features exhibited different polarization selection rules in terms of the polarization of the incident and scattered light. One feature (the 3D, state) displayed no splitting although a stress-dependent frequency shift was observed.

Due to the intense scattering at the 1S state, this state was studied first. This proved to be a convenient choice for another reason. The 1S state, unlike the higher states, produces a fluorescence feature (due to direct electron-hole recombination) which is readily observable in the spectrum when the Cu_2O sample is excited at any one of a number of frequencies lying higher than the 1S. The feature occurs at the frequency corresponding to the 1S state. This is the same frequency at which a peak in the resonant enhancement occurs (i.e. with the laser tuned to the exciton state rather than above it as in the case of fluorescence). Since the two processes presumably result from interactions involving the same state the stress dependence of the 1S state should be obtainable from either. The stress splitting of the enhancements should be the same as the splitting of the fluorescence feature. Observation of this correspondence (which has been performed) provided a check on the consistency of our methods and allowed an estimate of the extent to which stress inhomogeneities were present in the crystal.

Having studied the stress-dependence of the 1S state and having established consistency between the resonant Raman and the fluorescence techniques allowed us to exploit the occurrence of the 1S fluorescence feature when studying the excited states in the following way. With the laser tuned in the region of the excited states and with the crystal in the strained configuration the 1S fluorescence feature displays a splitting which is characteristic of the applied stress. Observation of the fluorescence feature is possible with the laser tuned anywhere in the region of the excited states. One simply "looks" at it by scanning the spectrometer through the 1S region. Since no laser tuning is required and since only one scan is needed, this provided a fast and convenient method for checking the magnitude of the applied stress when studying the higher states.

Two problems associated with the application of stress require discussion. The first has to do with friction in the stress apparatus causing the device to "stick". The problem manifests itself either as the lack of observed splittings below some finite "applied" stress or as an apparent crossing of stress-split components at a finite stress. This situation was evident during the preliminary experiments when the apparatus was new but ceased to be a problem thereafter. The other problem involves stress inhomogeneity. This results from the unavoidable bonding of the sample ends in the mounts which constrains the expansion of the ends in a direction perpendicular to the stress. No such constraint exists for the volume of the crystal not near the ends.

The force is thus applied over a smaller area at the crystal ends than elsewhere in the sample. The problem shows up as a stress-splitting which depends upon the portion of the crystal being optically probed. It existed in all the samples used to a greater or lesser degree. It was sample-dependent and was less objectionable for long slender crystals (1mm x 1mm x 10mm). The effect was more serious in crystals with dimensions 2mm x 2mm x 8mm.

The second type of experiment involved the study of polarization selection rules, as mentioned earlier. Once a splitting in an enhancement had been observed, the laser was tuned into resonance with each state in turn. With the laser tuned to one of these particular frequencies, polarization studies were carried out as follows. The polarization scrambler, analyzer and rotator were placed in the optical path. The latter two were set at angles corresponding to polarization of light parallel to specific crystallographic directions. This was done to compare group theoretical predictions with observed selection rules. The spectrometer was set to scan over the Γ_3'(109 cm^{-1}) feature. The experiment was repeated using a variety of incident and scattered polarization configurations. As discussed in the theory section, this permitted identification of the stress-split state responsible for a particular resonance. In some cases the addition of the optics discussed reduced the output signal to the extent that reliable measurements could not be made by the usual method. This could be overcome by increasing the time constant of the ratemeter while reducing the spectrometer scan rate to 5 cm^{-1} min^{-1}.

The data in Fig. 4-3 were taken for the 4S state in a crystal with stress applied parallel to [110] (rhombohedral stress). According to the discussion of Chapter III and Table 3-8, a stress of this symmetry reduces the crystal symmetry to C_{2v} and can split a triplet exciton state into three nondegenerate states transforming as Γ_1, Γ_3 and Γ_4 under the operations of the C_{2v} point group. In order to determine which of Γ_1, Γ_3 or Γ_4 were responsible for the enhancement of Fig. 4-3, the laser frequency was tuned back into resonance. A polarization rotator was then introduced to enable variation of the electric vector of the incident light while a polarization analyzer (and compensating scrambler) was placed in the path of the scattered light. Backscattering was from [001] ($\hat{x}_2$ in the notation of Table 3-8) and the stress was parallel to [110] ($\hat{x}_3$). The spectrometer was then used to scan over the Raman-scattered light for four different configurations of incident and scattered polarizations. These were $x_2\,(x_1x_1)\,\bar{x}_2$, $x_2(x_1x_3)\bar{x}_2$, $x_2\,(x_3x_1)\bar{x}_2$ and $x_2\,(x_3x_3)\,x_2$. The reduction in the intensity of the scattered light received by the spectrometer due to the additional optics necessitated the use of slower scans (and longer time constants) than were used for the enhancements.

The results of the polarization study are shown in Fig. 4-4. It is seen that the intensity is greater for incident polarization parallel to $\hat{x}_3$ while it is fairly independent of the polarization of the scattered light. Table 3-8 shows that the Γ_4 exciton state can be excited by light polarized along $\hat{x}_3$ but not along $\hat{x}_1$. The exciton state is thus identified as having Γ_4 symmetry. This same method was used in all the polarization studies used for state identification.

Cu_2O samples were cut as parallelepipeds (~1mm x 1mm x 10mm). In one set of experiments (tetragonal strain) the crystal was cut with [100] directions as principle axes. Backscattering measurements were made from a (100) surface with stress applied perpendicular to the scattering plane along [001] . In another set of experiments (rhombohedral stress) the crystal was cut with principle axes along [001] , [110] , and [110] . Stress was applied along [110] and backscattering measurements were made along [001] . A $(1\bar{1}\sqrt{2})$ surface was also cut for the purpose of conducting additional backscattering experiments. These measurements were not made as the crystal fractured before they became possible.

E. Sample Preparation

Cu_2O crystals used in these experiments were obtained from Brower and Parker[45] at the National Bureau of Standards. One of the crystals was zone-refined at City College; the rest were zone-refined at NBS. The annealing process was likewise carried out at NBS. X-ray analysis and orientation and all cutting, grinding, polishing and etching operations were conducted at City College. These processes will now be described in detail.

1. Crystal Growth

The first step in the process of obtaining quality crystals of cuprous oxide is the oxidation of copper rods in an oven at 1050° C for 100 hours. The rods, typically 6.3 mm in diameter, were made of oxygen-free high conductivity copper containing, by weight $< 0.01\%$ Ag and Mg and $< 0.001\%$ Fe, Mn and Si. This was followed by a pre-growth anneal at 900° C and 0.05 Torr for 16 hours. This brought the composition close to stoichiometric Cu_2O. The polycrystalline rods of Cu_2O so obtained were then zone-refined using the floating-zone technique. The apparatus used was the Plasma-Beam Zone Refiner model PBZ-99 manufactured by Materials Research Corp. In this process, carried out at 1200° C and in an O_2 atmosphere at 0.2 Torr pressure, a rod is held in a vertical position while a small element of the volume is heated to the melting point through electron bombardment. The current source is a hollow cathode which surrounds the rod to be zoned and is coaxial with it. The cathode is capable of vertical motion to enable scanning of the Cu_2O rod. The scan speed is continuously variable. The solidified portions of the rod above and below the "molten zone" rotate with respect to each other to insure temperature and composition uniformity. Achieving and maintaining a stable zone requires constant attention and a certain degree of experience. The existence of the zone relies on surface tension. If the temperature becomes too high, the molten material will flow and detach from the solid rod. If the zone cools, solidification will result in fracture of the rod due to the relative rotation discussed above. A good working voltage for rods of 6.3 mm diameter was found to be 1.6 Kvolt, although this did not guarantee success.

The purpose of zone-refining is to optimize density and stoichiometry. In addition, the process was found to result in a small number of columnar grains. The size of the grains, while an improvement over the small grains encountered in the unzoned material was marginal at best for the purpose of the current research. Cooling of the crystals, following zone-refining, resulted in formation of a thin film of CuO. This was easily removed by concentrated HCL followed by concentrated HNO_3 to remove the copper formed by the HCL.

Large single crystals can in principle be obtained by rezoning the zoned material as described above except that the rod is initially melted onto a small single crystal. It turns out that Cu_2O has no preferred growth direction and that, more often than not, the result of this procedure is another rod with a small number of columnar grains. Such was the case for all growth runs connected with this research.

Following the zone-refining stages, the Cu_2O crystals were post-annealed in a controlled atmosphere tube furnace. The crystals were heated to 1000° C in a pressure of the order 0.01 Torr. Oxygen was then admitted through a controlled leak and heating was continued in an oxygen atmosphere at a pressure of 0.7 Torr for 16 hours. Temperature and pressure were then simultaneously programmed downward so as to maintain the crystal within the stability field of Cu_2O. A P-T diagram for the system $Cu-O_2$ is shown in Fig. 4-5.

2. X-Ray Analysis and Orientation

Since only crystals of near-critical size for our experiments were available, the process of x-ray analysis to find a crystal of appriate orientation and dimensions turned out to be the most time-consuming part of the crystal preparation operation. A General Electric X-ray diffraction unit was used for all x-ray analysis. The Laue back-reflection method was used.

The first step was to x-ray one of the larger grains at a number of places to insure that it was in fact a single crystal. Next, the crystal was rotated about a point a number of times to determine its orientation through a succession of Laue photographs. At first, a Molybdenum X-ray tube was used as it produces Laue patterns of Cu_2O which permit ready identification of the important crystallographic directions. After some experience had been gained, the patterns could also be recognized using a copper tube even though the characteristic radiation contributes to the pattern. This tube had the advantage of allowing useful Laue pictures to be taken with short exposure times.

Once the orientation had been determined, the goniometer on which the crystal was mounted was transferred

FIG. 4-5. P-T diagram for the system Cu-O_2. (A) initial oxidation of copper in air; (B) pre-growth anneal; (C) post-growth anneal of crystals where dashed line indicates pressure-temperature path during cooling.

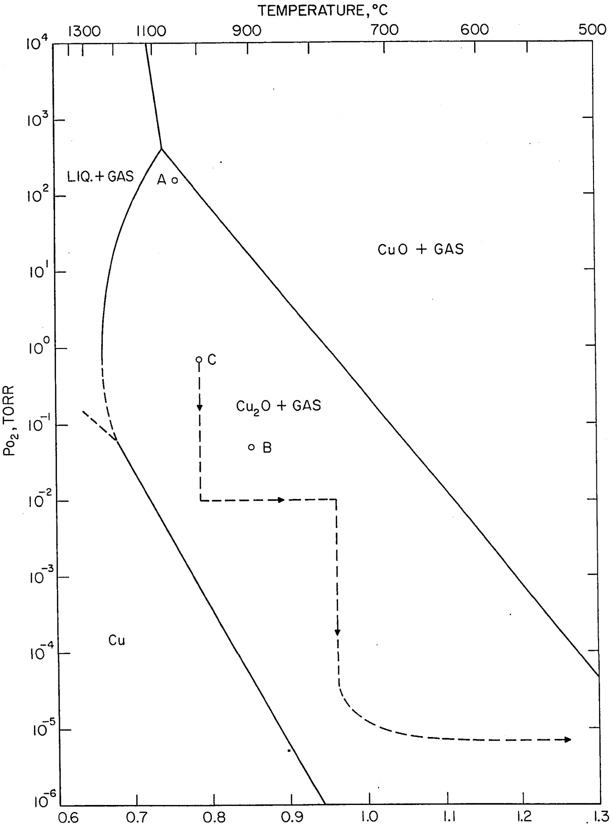
TEMPERATURE, °C
1300
1100
900
700
600
500
10^4
10^3
10^2
10^1
10^0
10^{-1}
10^{-2}
10^{-3}
10^{-4}
10^{-5}
10^{-6}
P_{O_2}, TORR
LIQ. + GAS
A
CuO + GAS
C
Cu_2O + GAS
B
Cu
0.6
0.7
0.8
0.9
1.0
1.1
1.2
1.3
10^3/T, K

to a diamond saw. The arrangement allowed cuts to be made on the crystal along planes which had been determined from x-rays. The crystal was further cut and ground with a coarse grit so that its dimensions were near to those intended for the experiment, and with mutually perpendicular surfaces defining the crystallographic axes relevant to the experiment. Specifically these were the [100] directions for crystals stressed tetragonally while the directions were [110], [110] and [001] for rhombohedrally-stressed crystals. The crystal so cut was x-rayed again to study parts of the crystal which were previously inaccessible (to verify the single-crystal nature of the sample). X-rays were also taken to insure that no misalignment occurred during cutting and grinding. Upon completion of this examination, final grinding and polishing could begin.

3. Polishing and Etching

Polishing and grinding of the crystal was done with the use of a hand-held device to which the crystal was cemented with glycol thallate. The device allowed manual pressure to be applied during polishing and had a flat base which preserved the orientation of the crystal with respect to the polishing surface. The following procedure was used to produce a good optical polish:

a) The crystal was ground on a glass plate using a slurry of 10μ silicon carbide polishing grit and water.

b) A slurry of 5μ silicon carbide grit and water was used to grind the crystal on a glass plate.

c) A slurry of 1μ silicon carbide grit and water was used as above.

d) Polishing began with the use of a slurry of 1μ silicon carbide and ethylene glycol on a glass plate covered with a pellon pad. This was the first stage at which the crystal surface appeared polished although fine scratches remained.

e) The residual scratches were removed using a slurry of 0.3μaluminum oxide (Linde A) and ethylene glycol on a glass plate covered with a pellon pad.

Different glass plates and pellon pads were used for each step. Care was taken to remove all polishing grit from the sample and its holder before proceeding to the next finer grit. This was necessary to avoid contamination of the glass plate with consequent scratching of the crystal.

After polishing the crystal was thoroughly cleaned, etched in concentrated nitric acid for 10 seconds, and rinsed in distilled water. Etching is required to remove the damaged surface layer which results from mechanical polishing. It was found during the experiments that the intensity of the Raman scattered light depended critically on the etch and that in several cases repolishing and re-etching were necessary.

CHAPTER V

RESULTS

A. Introduction

This chapter contains the results of experiments conducted in the course of the present research. As discussed in Chapter IV, the experiments were of two types. The first used resonant Raman scattering as a quadrupole spectrometer to locate exciton states of electric quadrupole symmetry (i.e. Raman scattering with the laser tuned to such states produces an enhancement in Raman scattering from odd-parity phonons and in particular from the 109 cm^{-1} phonon). The second type of experiment was designed to identify the symmetry and degeneracy of particular exciton states in the strained Cu_2O crystal. This was done by tuning the laser to a particular state, observing how the Raman intensity depended upon the polarization of the incident and scattered light, and comparing with Table 3-8.

Four exciton states were studied. These were the states assigned as the 1S, 3S, $3D_1$ and 4S states of the yellow exciton series according to Refs. 23 and 28. The accepted energies of these states were shown in Fig. 2 - 4 and were reexamined during the present experiments.

Experiments were performed using two different stress configurations: tetragonal (stress parallel to [001]) and rhombohedral (stress parallel to [110]). Features common to both were discussed in Chapter IV. Specific results for the tetragonal stress and the rhombohedral stress are discussed in Sections B and C respectively.

B. Tetragonal Stress

The experiments involved application of stress along [001] and backscattering from [100]. The polarization of the incident light was either along [001]($\hat{z}$) or [010]($\hat{y}$) and scattered light was either unanalyzed (for enhancement experiments) or was along $\hat{z}$ or $\hat{y}$ (for polarization studies). Resonant Raman studies were carried out as described in Chapter IV. Fig. 5 - 1 gives the Raman intensity vs incident laser frequency with the laser tuned through the 1S state of the yellow series. It is seen that in the strained crystal, resonant enhancement occurs at two different frequencies whereas in the unstrained crystal it occurs only with the laser frequency tuned to 16399 cm^{-1}. This splitting is attributed to the splitting of the exciton state (${}^3\Gamma_5^+ \rightarrow {}^2\Gamma_5^+ + {}^1\Gamma_4^+$) produced by the stress (which lowers the crystal symmetry from O_h to D_{4h}). This was shown schematically in Fig. 3 - 3.

Scattering with the laser tuned to the state which shifts to lower energy was most intense for the polarization configuration x (zy) $\bar{x}$. For the higher state it occurred for x (yz) $\bar{x}$. Reference to Table 3-8 shows that these are the states of symmetry ${}^2\Gamma_5^+$ and ${}^1\Gamma_4^+$, respectively.

The frequencies at which maxima in the Raman scattering enhancements occur (presumably the energies of the stress-split exciton states) have been plotted in Fig. 5 - 2 as a function of applied stress. The figure gives results for all of the exciton states studied. Table 5-1 gives the results of polarization studies conducted for all of the states.

The stress-dependence of the energies of the exciton states studied may be described, to terms quadratic in the stress by,

$$E = E_o + BX + CX^2 \tag{5-1}$$

where E_o is the energy of the state in the unstrained crystal and X is the magnitude of the applied stress. A least-squares fit of the curves in Fig. 5 - 2 to Eq. (5-1) was carried out by computer. The best-fit coefficients are shown in Table 5-2. These results will facilitate the discussions to be taken up in the next chapter.

C. Rhombohedral Stress

This set of experiments was done with stress applied parallel to [110] and with backscattering from [001] . These are $\hat{x}_3$ and $\hat{x}_2$ in the notation of Table 3-8. The experiments were otherwise conducted as for the tetragonal case.

The discussion of Chapter III showed that a stress of this symmetry reduces the crystal symmetry to C_{2v} and splits the quadrupole-allowed exciton states according to ${}^3\Gamma_5^+ \rightarrow {}^1\Gamma_1 + {}^1\Gamma_3 + {}^1\Gamma_4$. This was shown in Fig. 3 - 3.

Table 3-8 shows that backscattering along $\hat{x}_2$ can excite only states with ${}^1\Gamma_3$ or ${}^1\Gamma_4$ symmetry. As discussed in Chapter III, the ${}^1\Gamma_1$ state may be excited by backscattering from $(1\bar{1}\sqrt{2})$. Although the crystal in these experiments was

FIG. 5 - 1. Raman intensity for the Γ_3^- (109 cm^{-1}) phonon vs incident laser frequency for incident frequencies near the 1S state of the yellow exciton series in Cu_2O crystals subject to stress parallel to [001] (tetragonal stress). Shown are the results for two finite stresses as well as for the zero-stress case. The occurrence of pairs of resonant peaks for a given stress is evident. The polarization configuration which gives the most intense scattering is denoted by yz (solid line) or zy (dashed line).

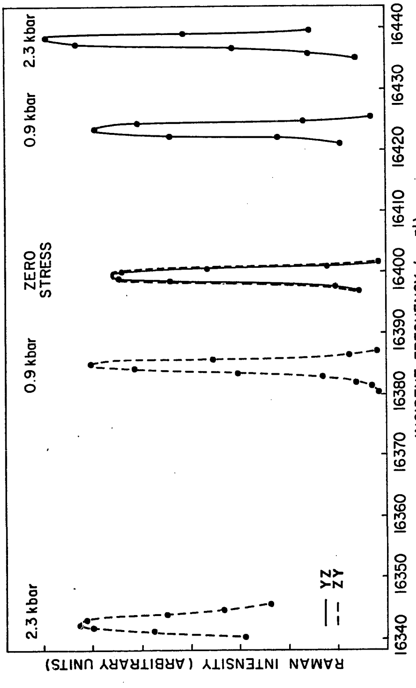
2.3 kbar
0.9 kbar
ZERO STRESS
0.9 kbar
2.3 kbar
— YZ
-- ZY
16340
16350
16360
16370
16380
16390
16400
16410
16420
16430
16440
INCIDENT FREQUENCY (cm^{-1})
RAMAN INTENSITY (ARBITRARY UNITS)

FIG. 5 - 2. Energy of resonant Raman scattering maxima vs applied stress in Cu_2O for tetragonal stress. The data points give the energies of quadrupole-allowed exciton states. Polarization selection rules (Table 5-1) allow identification of ${}^2\Gamma_5^+$ levels (circles) and ${}^1\Gamma_4^+$ levels (triangles) into which states split under stress. No splitting was resolved for the $3D_1$ state.

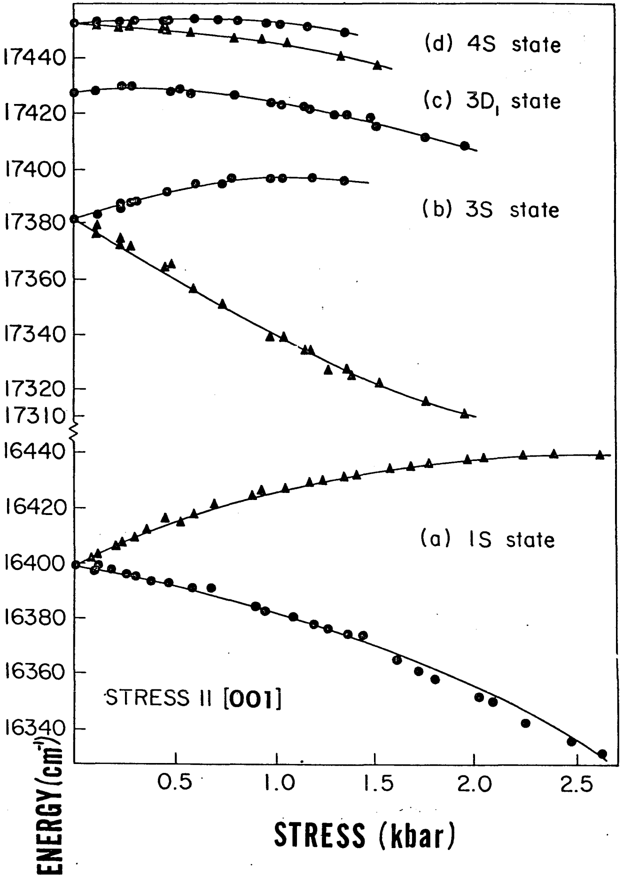
(d) 4S state
(c) 3D$_1$ state
(b) 3S state
(a) 1S state
STRESS ∥ [001]
ENERGY (cm^{-1})
STRESS (kbar)
17440
17420
17400
17380
17360
17340
17320
17310
16440
16420
16400
16380
16360
16340
0.5
1.0
1.5
2.0
2.5

prepared with a $(1\bar{1}\sqrt{2})$ polished face, optical access required rotation of the crystal in its mounts which resulted in its fracture. Most of the data, therefore, is for the stress-split levels of ${}'\Gamma_3$ and ${}'\Gamma_4$ symmetry. It was possible, however, to study the ${}'\Gamma_1$ component of the 1S state. This was due to the very intense scattering generally associated with the 1S state combined with slight sample misalignment. The Raman intensity with the laser tuned to resonance with the ${}'\Gamma_1$ state was reduced by a factor $\sim 10^{-4}$ relative to the Raman intensities for the ${}'\Gamma_3$ and ${}'\Gamma_4$ states.

The stress-induced splittings of the exciton states were smaller for this case than for the tetragonal case. It was therefore more illustrative to display the results for each exciton state in a separate figure. Figs. 5 - 3, 5 - 4, and 5 - 5 show the stress dependence of the 1S, 3S and the two higher states respectively.

The results of polarization studies of the stress-split components are given in Table 5-3. The best-fit coefficients for a computer-aided least-squares fit of the curves in Figs. 5 - 3, 5 - 4 and 5 - 5 to Eq. (5 - 1) are given in Table 5-4.

TABLE 5-1

Symmetry Identification of Stress-Split Exciton States (Tetragonal Stress)

Exciton State	Intensity of polarized Raman scattering			
	$x(zz)\bar{x}$	$x(zy)\bar{x}$	$x(yy)\bar{x}$	$x(yz)\bar{x}$
1S (high energy)	20	<1	10	720
1S (low energy)	6	170	12	1
3S (high energy)	<7	50	<4	<7
3S (low energy)	<5	<5	<4	55
$3D_1$	<2	28	<2	28
4S (high energy)	<2	25	<2	11
4S (low energy)	<3	<3	<2	60
Theoretical predictions (See Table 3-8)				
${}^2\Gamma_5^+$	—	yes	—	—
${}^1\Gamma_4^+$	—	—	—	yes

TABLE 5-2. Stress Dependence of Exciton State Energies (Tetragonal Stress)

Best-fit values to $E = E_0 + BX + CX^2$

Exciton state	B ($\mathrm{cm^{-1}kbar^{-1}}$)	C ($\mathrm{cm^{-1}kbar^{-2}}$)	Δ'($\mathrm{cm^{-1}}$)
1S $^1\Gamma_4^+$	31.4 ± 0.1	-6.5 ± 0.1	618
1S $^2\Gamma_5^+$	-11.4 ± 0.1	-6.2 ± 0.1	
3S $^1\Gamma_4^+$	-50.5 ± 1.4	6.3 ± 0.8	1015
3S $^2\Gamma_5^+$	28.2 ± 1.9	-12.8 ± 1.2	
3D$_1$	0.3 ± 1.5	-5.7 ± 0.8	1015
4S $^1\Gamma_4^+$	-1.6 ± 2.2	-4.9 ± 1.5	1037
4S $^2\Gamma_5^+$	7.7 ± 1.2	-6.8 ± 1.2	

FIG. 5 - 3. Energy of resonant Raman scattering maxima vs applied stress in Cu_2O for rhombohedral stress with incident laser frequencies in the region of the 1S state of the yellow exciton series. Data points give the energies of the stress-split levels of symmetry ${}'\Gamma_1$, ${}'\Gamma_3$ and ${}'\Gamma_4$. Symmetry identifications resulted from polarization studies (see Table 5-3).

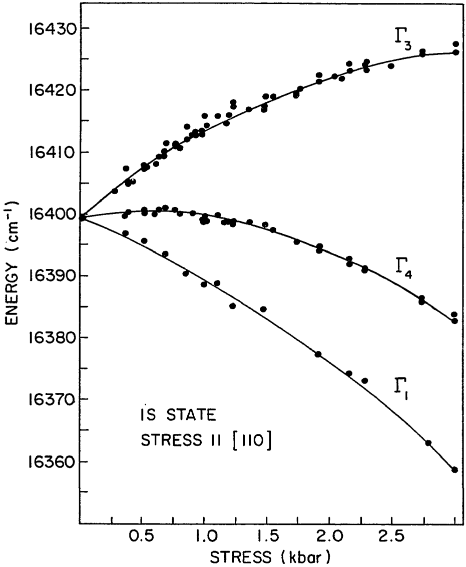
16430
16420
16410
16400
16390
16380
16370
16360
ENERGY (cm^{-1})
0.5
1.0
1.5
2.0
2.5
STRESS (kbar)
Γ_3
Γ_4
Γ_1
1S STATE
STRESS ∥ [110]

FIG. 5 - 4. Energy of resonant Raman scattering maxima vs applied stress in Cu_2O for rhombohedral stress with incident laser frequencies in the region of the 3S state of the yellow exciton series. Energies for stress-split levels of Γ_3 and Γ_4 symmetry are shown. Scattering from the Γ_1 state was not observed. See Table 5-3 for symmetry identifications.

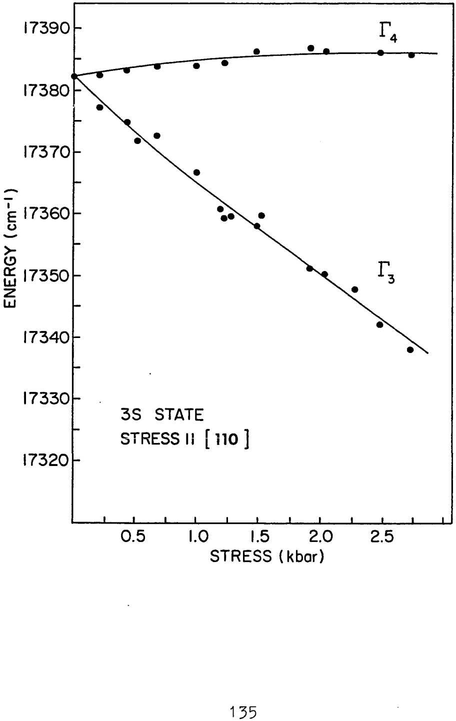
17390
17380
17370
17360
17350
17340
17330
17320
ENERGY (cm^{-1})
0.5
1.0
1.5
2.0
2.5
STRESS (kbar)
Γ_4
Γ_3
3S STATE
STRESS ∥ [110]

FIG. 5 - 5. Energy of resonant Raman scattering maxima vs applied stress in Cu_2O for rhombohedral stress with incident laser frequencies in the region of the 3D, and 4S states of the yellow exciton series. Energies for stress-split levels of Γ_3 and Γ_4 symmetry are shown. Scattering from the Γ_1 state was not observed. See Table 5-3 for symmetry identifications.

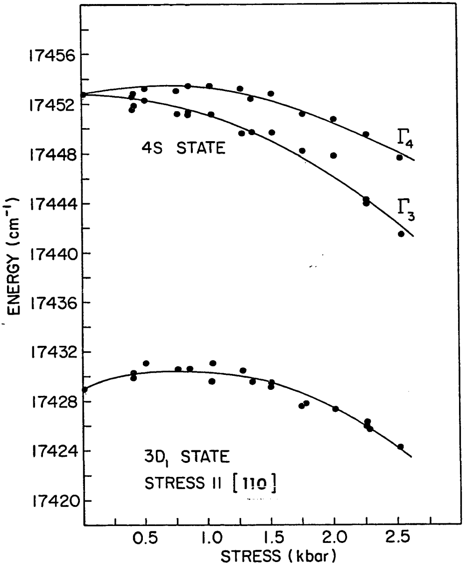
ENERGY (cm^{-1})
17456
17452
17448
17444
17440
17436
17432
17428
17424
17420
4S STATE
Γ_4
Γ_3
3D$_1$ STATE
STRESS II [110]
0.5
1.0
1.5
2.0
2.5
STRESS (kbar)

TABLE 5-3

Symmetry Identification of Stress-Split Exciton States (Rhombohedral Stress)

Exciton State	Intensity of polarized Raman scattering			
	$x_2(x_3x_3)\bar{x}_2$	$x_2(x_3x_1)\bar{x}_2$	$x_2(x_1x_3)\bar{x}_2$	$x_2(x_1x_1)\bar{x}_2$
1S(high energy)	32	9	1600	620
1S(intermediate)	620	1320	20	50
1S(low energy)	See text			
3S(high energy)	14	15	<6	<2
3S(low energy)	<2	<2	11	4
$3D_1$	27	54	21	23
4S(high energy)	28	30	9	<6
4S(low energy)	<6	11	22	19
Theoretical predictions (See Table 3-8)				
Γ_3	—	—	yes	yes
Γ_4	yes	yes	—	—
Γ_1	See text			

TABLE 5-4. Stress Dependence of Exciton State Energies (Rhombohedral Stess)

Best-fit Values to $E = E_o + BX + CX^2$

Exciton state	B $(cm^{-1}kbar^{-1})$	C $(cm^{-1}kbar^{-2})$	$\Delta'(cm^{-1})$
1S ${}^1\Gamma_1$	-7.7 ± 1.2	-1.9 ± 0.4	618
1S ${}^1\Gamma_3$	16.2 ± 0.9	-2.5 ± 0.3	
1S ${}^1\Gamma_4$	2.8 ± 0.4	-2.8 ± 0.1	
3S ${}^1\Gamma_3$	-16.8 ± 1.1	0.5 ± 0.4	1015
3S ${}^1\Gamma_4$	3.4 ± 1.3	-0.7 ± 0.5	
$3D_1$	3.2 ± 2.3	-2.0 ± 0.8	1015
4S ${}^1\Gamma_3$	1.1 ± 1.1	-2.0 ± 0.2	1037
4S ${}^1\Gamma_4$	2.8 ± 1.1	-1.8 ± 0.2	

CHAPTER VI .

ANALYSIS AND DISCUSSION

A. Introduction

In this chapter, the results of Chapter V will be compared with the theory of Chapter III. In Section B is given a qualitative discussion of the most significant aspects of the observed stress behavior of all of the exciton states studied. The results of a detailed numerical analysis of the 1S state of the yellow series is presented in Section C. Conclusions drawn from the analyses are given in Section D.

B. Qualitative Discussion of Observed Stress Behavior

In Chapter III, a second-order perturbation treatment applied to the energy matrix of Table 3-11 yielded approximate eigenvalues for exciton states of a particular principal quantum number. The eigenvalues were displayed in Table 3-12. The (orthoexciton) S states of the yellow exciton series are predicted to split, under tetragonal stress, into a doublet and a singlet whose energies, relative to their zero stress values, are

$$E_{\text{DOUBLET}}(X) = hX - \left(\frac{4eJ}{3\Delta'}\right)X - \left(\frac{2e^2}{\Delta'}\right)X^2$$

$$E_{\text{SINGLET}}(X) = hX + \left(\frac{8eJ}{3\Delta'}\right)X - \left(\frac{2e^2}{\Delta'}\right)X^2 \qquad (6\text{-}1)$$

where h and e are deformation parameters, J is the exchange parameter, X is the applied stress and Δ' gives the energy difference between yellow and green exciton states (for a particular principal quantum number). is determined by the valence band spin-orbit splitting and by the difference in the Coulomb energy for yellow and green states (which is a function of n).

The experimental data shown in Fig. 5 - 2 were least-squares fit to the function $E = aX + bX^2$ and the resulting linear and quadratic coefficients were listed in Table 5-2. (The doublet and singlet were distinguished experimentally by polarization selection as indicated in Table 5-1). The state assignments follow those of the Strasbourg group with the $3D_1$ assumed to be partially quadrupole through hybridization with the nearby 4S.[28,29]

Comparison of the data with Eqs. (6-1) is complicated by the n dependence of Δ' which is not directly measurable since the energies of the green S exciton states are uncertain. A reasonable approximation to $\Delta'(n)$ is obtained by taking the difference of the energies given by the Rydberg equations for the p states[28,41]

$$\begin{aligned} E_g &= 18{,}588 - \frac{1242}{n^2} \quad \text{cm}^{-1} \\ E_y &= 17{,}523 - \frac{795}{n^2} \quad \text{cm}^{-1} \end{aligned} \qquad (6\text{-}2)$$

and assuming that the central cell corrections and/or quantum defects which shift S states relative to these values will be similar for the yellow and green series. The resulting Δ' is 618 cm^{-1} for n = 1 and increases monotonically with n towards the ionization limit $\Delta'(\infty) =$ 1065 cm^{-1} which is just the spin-orbit energy Δ . These values of $\Delta'(n)$ are also listed in Table 5 - 2.

Since Δ' is positive for all n and $J \propto n^{-3}$ while the deformation parameters h and e are assumed to be independent of n, the sense of the linear splitting is predicted by Eqs. (6-1) to be the same for all yellow exciton states, while its magnitude should decrease faster than n^{-3}. This prediction is seen to be in clear disagreement with the data since the sense of the splitting of the 1S state (singlet moves up, doublet moves down) is inverted in the higher states. Furthermore, the magnitude of the splitting is larger for the 3S state than for the 1S as previously noted by Agekyan and Stepanov.[40] Note also that no splitting was resolved for the $3D_1$ state.

Equations (6-1) also predict that the quadratic coefficient b should be negative for all states, with equal magnitude for the doublet and singlet of a given n, and should decrease with increasing n as $1/\Delta'$. Although the 1S states exhibit negative and approximately equal values of b, the 3S state is again seen to behave anomalously. (The positive curvature of the 3S ${}^1\Gamma_4^+$ is also evident in the data of Fig. 5 - 2).

It is thus seen that comparison of the theory with the experimental results leads to gross inconsistencies. Putting aside the interpretation of the stress behavior of the excited states for now, it is seen that the behavior of the 1S state by itself does not contradict the theory. The multiplicity of the splitting agrees with the theoretical prediction, the quadratic coefficients describing the nonlinear stress behavior of the doublet and the singlet are negative and roughly equal, and the relative magnitude of the linear coefficients is not unreasonable.

Although detailed calculations are reserved for the next section, it is necessary at this point to determine approximate values for the linear terms in Eqs. (6-1). Comparison of Eqs. (6-1) with Table 5 - 2 show that the observed splitting is characterized by parameters approximately satisfying

$$h \cong 3 \text{ cm}^{-1} \text{ kbar}^{-1}$$

$$\frac{4eJ}{3\Delta'} \cong 14 \text{ cm}^{-1} \text{ Kbar}^{-1} \qquad (6\text{-}3)$$

It is interesting to study also the behavior of the 1S state under rhombohedral stress. The results for this case were shown in Fig. 5 - 3 where it was seen that the multiplicity of the splitting agrees with the results of group theory (Fig. 3 - 3) and with the predictions of the perturbation treatment namely that the energies of the split states, relative to their zero stress values, are

$$\begin{aligned} E_{\Gamma_4}(X) &= hX + \left(\frac{2eJ}{3\Delta'} + \frac{2fJ}{\Delta'}\right)X - \left(\frac{e^2}{2\Delta'} + \frac{33f^2}{16\Delta'} - \frac{3ef}{8\Delta'}\right)X^2 \\ E_{\Gamma_3}(X) &= hX + \left(\frac{2eJ}{3\Delta'} - \frac{2fJ}{\Delta'}\right)X - \left(\frac{e^2}{2\Delta'} + \frac{33f^2}{16\Delta'} + \frac{3ef}{8\Delta'}\right)X^2 \\ E_{\Gamma_1}(X) &= hX - \left(\frac{4eJ}{3\Delta'}\right)X - \left(\frac{e^2}{2\Delta'} + \frac{6f^2}{\Delta'}\right)X^2 \end{aligned} \qquad (6\text{-}4)$$

from Table 3 - 15. The consistency of the rhombohedral splitting with the tetragonal case may now be tested. We first observe from Eqs. (6-1) and (6-4) that the linear coefficient for the Γ_1 stress behavior should be the same as is obtained for the doublet in the tetragonal case. These numbers are respectively -7.7 and -11.4 cm^{-1} $Kbar^{-1}$ from Tables 5 - 4 and 5 - 2. Thus the signs are in agreement while the magnitudes differ by 50%. We observe also that the average of the slopes for the Γ_3 and Γ_4 states in the rhombohedral case is, from Eqs. 6 - 4

$$h + \frac{2eJ}{3\Delta'} \qquad (6\text{-}5)$$

The value predicted using the parameters in Eqs. (6-3) (which were derived from the tetragonal results) is 10 cm^{-1} $Kbar^{-1}$. The observed value is $\frac{1}{2}$ (16.2 + 2.8) = 9.5 cm^{-1} $Kbar^{-1}$, from Table 5 - 4.

Finally comparing the linear terms in Eq. (6-4) with the observed values in Table 5 - 4 it is possible to approximately determine the ratio f/e which turns out to be about-6/21. Substituting this and Eqs. (6-3) into Eqs. (6-4) the quadratic coefficients for the Γ_1 , Γ_3 and Γ_4 states are predicted to be -3.2, -1.8 and -2.5 cm^{-1} $Kbar^{-2}$ respectively. These values may be compared with the observed values of -1.9, -2.5 and -2.8. The agreement is reasonable, at least for the Γ_3 and Γ_4 states.

In the present approximation then, the observed stress behavior of the 1S for tetragonal stress and for rhombohedral stress are consistent with the theory of Chapter III and with each other.

C. Analysis of The Stress Behavior of the 1S State

In view of the errors inherent in the perturbation approximation, further analysis was performed by diagonalization of the energy matrix (Table 3-11) for a sequence of values of the stress in the range 0 to 2.75Kbars. The diagonalization was performed as a subroutine of a non-linear least squares fitting program which varied the parameters Δ', J, e and h to produce a best fit of the predicted yellow exciton energies $E_{5,8}$ and E_{10} to the experimental values.

The three exchange parameters J, J_y and J_g which appear in the energy matrix (Table 3-11) are related by Eqs. (3-63). The atomic exchange factors J_y^A and J_g^A may be different since the Bloch functions may involve somewhat different distributions within the unit cell. Neglecting this effect (which should in any case be small) one has only the difference in $|\phi(0)|^2$ which is proportional to $(R/n)^3$ where R is the Rydberg constant and n is the principle quantum number. Since the ratio of green to yellow Rydberg constants (Eq. 6 - 2) is very close to $(4)^{1/3}$, we then have:

$$\begin{aligned} J &= J_o/n^3 \\ J_y &= \tfrac{1}{2} J = J_o/2n^3 \\ J_g &= 2J = 2J_o/n^3 \end{aligned} \qquad (6\text{-}6)$$

The constant J_o is proportional to the atomic exchange constant and should, on very general grounds, be negative. This would cause an exchange splitting between a spin singlet and a spin triplet, with the triplet lying below the singlet (Hund's rule).

The ortho and para yellow excitons are not triplet and singlet spin states however, as noted in Chapter III.

The singlet Γ_2 paraexciton is pure spin triplet, while the triplet Γ_5 orthoexciton is mixed spin singlet and triplet. Consequently, the exchange splitting produced by negative J puts the singlet below the triplet in the unstressed crystal by:

$$E_{TRIPLET} - E_{SINGLET} = -\frac{1}{6} J_y - \frac{8}{9} \frac{J^2}{\Delta'} - \frac{1}{2} J_y$$

$$= -\frac{2}{3} J_y - \frac{8}{9} \frac{J^2}{\Delta'} = -\frac{J}{3} - \frac{8}{9} \frac{J^2}{\Delta'} = \frac{|J|}{3} - \frac{8}{9} \frac{J^2}{\Delta'} \qquad (\ 6\text{-}7\ )$$

in agreement with recent experimental observations of the singlet 1S paraexciton approximately 100 cm^{-1} below the 1S triplet.[38,39,43]

Using Eq. (6-6) to express J_y and J_g in terms of J, the non-linear least squares analysis described above was applied to the data for the 1S state as follows. The parameters Δ', J, e and h were initialized and the program proceeded to compute eigenvalues of the energy matrix (for a given stress), compare the eigenvalues corresponding to the 1S yellow state to the data for the same stress and compute the sum of the squares of the differences. The procedure was repeated for each stress corresponding to experimental data and the sum of squares of differences between the entire set of experimental values and predicted eigenvalues was generated. The program then varied the parameters, repeated the above calculation and computed the set of parameters (Δ', J, e, h) which minimized the above sum.

The analysis was carried out for a variety of initial parameter sets. In each case it was found that the final value of Δ' differed little from the starting value. The program was run thereafter with Δ' held constant while J, e and h were varied to produce a best-fit. Successive runs of the program were conducted with different values of Δ' in order to determine its effect on the fit.

The results showed that the fit became noticeably improved for values of Δ' greater than 3200 cm^{-1}.

As stated earlier, Δ' can reasonably be expected to assume values near 600 cm^{-1} but in any case no greater than 1065 cm^{-1}. It is not possible to reconcile the value of Δ' resulting from the data analysis with the predictions based on our understanding of the (p states of the) exciton series in Cu_2O. Plots of the theoretical stress behavior of the 1S state for two values of Δ' are compared with the experimental data in Fig. 6 - 1.

FIG. 6 - 1. Comparison of the experimental data for the 1S state (tetragonal stress) with theoretical predictions resulting from diagonalization of the energy matrix (Table 3-11). The dashed line gives the best fit that can be obtained with $\Delta' = 600\ \mathrm{cm}^{-1}$ in which case $J = -183\ \mathrm{cm}^{-1}$, $e = 47\ \mathrm{cm}^{-1}\mathrm{kbar}^{-1}$ and $h = -4\ \mathrm{cm}^{-1}\mathrm{kbar}^{-1}$. The solid curve shows the best overall fit which obtains for $\Delta' = 3600\ \mathrm{cm}^{-1}$, $J = -357\ \mathrm{cm}^{-1}$, $e = 123\ \mathrm{cm}^{-1}\mathrm{kbar}^{-1}$ and $h = -5\ \mathrm{cm}^{-1}\mathrm{kbar}^{-1}$.

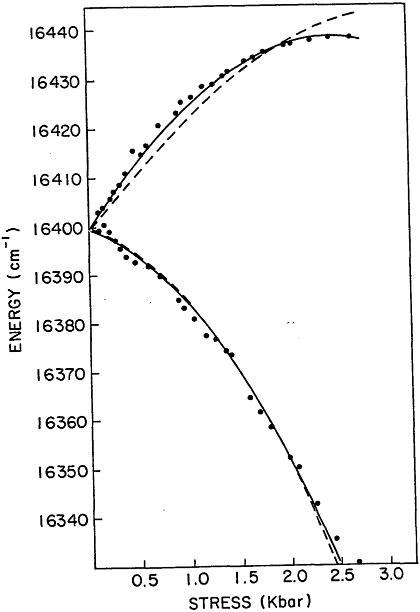
16440
16430
16420
16410
16400
16390
16380
16370
16360
16350
16340
ENERGY (cm^{-1})
0.5
1.0
1.5
2.0
2.5
3.0
STRESS (Kbar)

The diagonalization procedure was also applied to the energy matrix for the rhombohedral stress (Table 3-14). To test consistency with the results for tetragonal stress, the set of parameters Δ', J, e and h used were those corresponding to a best-fit for the tetragonal case. This set of parameters was held constant during each run while the parameter f was varied to yield the best fit. Results of this procedure are shown in Fig. 6-2. For positive f the fit was extremely poor regardless of the value of Δ' chosen. This is consistent with the discussion of the preceding section wherein a negative f was anticipated. With f taken to be negative, the fit for $\Delta' = 600\ \mathrm{cm}^{-1}$ was reasonable while the fit for $\Delta' = 3600\ \mathrm{cm}^{-1}$ was quite poor.

The above result seems to contradict the results for the tetragonal case. It should be noted, though, that the fit obtained for the tetragonal case with $\Delta' = 600$ was not unreasonable and that this value of Δ' gives fairly good fits for both the tetragonal and the rhombohedral splittings. A discussion of the limitations associated with this calculation will be taken up in the next section.

D. Discussion and Conclusions

The discussion in Sections B and C led to several conclusions which may be summarized as follows.

The stress behavior of the 1S state of the yellow exciton series has been observed to be consistent with group theoretical predictions concerning the expected multiplicities of stress-induced splittings and the

FIG. 6 - 2. Comparison of the experimental data for the 1S state (rhombohedral stress) with theoretical predictions resulting from diagonalization of the energy matrix (Table 3-14). The heavy solid line shows the best fit possible for $\Delta' = 3600\ \mathrm{cm}^{-1}$, $J = -357\ \mathrm{cm}^{-1}$, $e = 123\ \mathrm{cm}^{-1}\mathrm{kbar}^{-1}$ and $h = -5\ \mathrm{cm}^{-1}\mathrm{kbar}^{-1}$ in which case $f = -25\ \mathrm{cm}^{-1}\mathrm{kbar}^{-1}$. The best fit for $\Delta' = 600\ \mathrm{cm}^{-1}$, $J = -183\ \mathrm{cm}^{-1}$, $e = 47\ \mathrm{cm}^{-1}\mathrm{kbar}^{-1}$, and $h = -4\ \mathrm{cm}^{-1}\mathrm{kbar}^{-1}$ obtains for $f = -27\ \mathrm{cm}^{-1}\mathrm{kbar}^{-1}$ and is shown as the heavy dashed line.

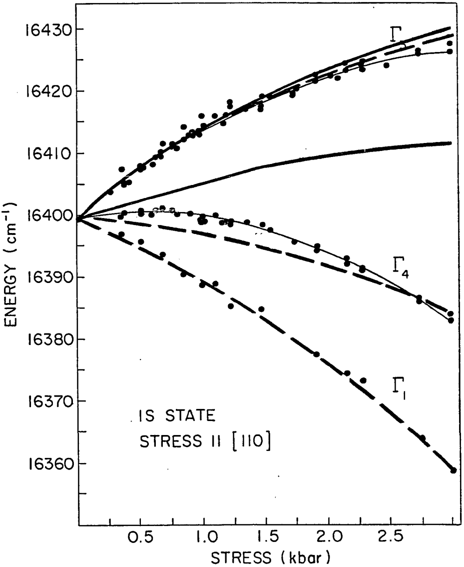
16430
16420
16410
16400
16390
16380
16370
16360
ENERGY (cm^{-1})
0.5
1.0
1.5
2.0
2.5
STRESS (kbar)
Γ
Γ_4
Γ_1
1S STATE
STRESS ll [110]

expected polarization selection rules of the stress-split levels. The gross features of the stress behavior were seen to be in agreement with the results of the effective Hamiltonian formalism in which the 1S yellow exciton states and the 1S green exciton states are taken together to form a 12-state basis and in which the splitting of the 1S yellow state is seen to arise from the simultaneous effects of (electron-hole) exchange and strain. The quantitative agreement was fair at best. The disparity is most likely due to the limitations of the effective Hamiltonian formalism.

The observed stress behavior of the excited states of the yellow exciton series was not consistent with the theory which predicts that the sense of the linear splitting should be the same for all yellow exciton states while its magnitude should decrease faster than n^{-3}. Instead, the magnitude of the splitting for the 3S state was actually larger than for the 1S state and the sense of the splitting was inverted. The sense of the splitting for the 4S state was likewise inverted although the magnitude was smaller than for either the 3S or 1S states. The $3D_1$ state did not exhibit a splitting. The 3S $^1\Gamma_4$ state displayed a positive curvature in contrast to all other stress-split exciton states studied. It is interesting to note that the quadratic coefficient for the 3S $^1\Gamma_4$ is approximately equal and opposite to the quadratic coefficient for the 1S state (see Table 5-2) while one component of the 1S state of the green exciton series is predicted to exhibit such behavior (see

TABLE 6-3

Derived Deformation Potentials for Cu_2O

	Deformation Potentials		
	a	b	d
Cu_2O ($\Delta' = 600\ cm^{-1}$)	-1.8 eV	-0.3 eV	0.5 eV
Cu_2O ($\Delta' = 3600\ cm^{-1}$)	-2.1 eV	-0.8 eV	0.4 eV
CuCl*[78]	——	-0.4 eV	0.7 eV

Table 3-12: green Γ_5 triplet). Thus the data suggests that the state assigned as the 3S yellow may in fact be the 1S state of the green series. Further indication of this is the clear difference between the quadratic coefficients of the two stress-split components of the 3S state (see Table 5-2) which is also consistent with the predictions of Table 3-12 for the 1S (Γ_5) state of the green series. It should be noted, however, that the observed linear splitting for the "3S" state is inconsistent with that predicted for the 1S (Γ_5) green state.

It was seen in Table 5-2 that the 3S ${}^1\Gamma_4$ is the only state exhibiting a positive quadratic coefficient. In fact, the ${}^1\Gamma_4$ and ${}^2\Gamma_5$ components of the 1S, $3D_1$, and 4S states had quadratic coefficients which were very nearly the same. The nonlinear stress behavior for exciton states of the yellow series (which is independent of the exchange constant as can be seen from Table 3-12) should be about the same for all states of the yellow series. In this regard then, the behavior of the 1S, $3D_1$, and 4S states is consistent with predictions for yellow exciton states while that for the 3S state is not.

The inversion in the sense of the splitting for the higher states is not in agreement with the theory, as has been stated. Perhaps a complicated dependence of the exchange interaction on principal quantum number is responsible.

It should also be pointed out that the $3D_1$ state behaves like an nS state of the yellow series with $n \gtrsim 3$ since, according to the theory, the magnitude of the splittings should be proportional to n^{-3} and could thus be too small to resolve for such states. Furthermore, the zero stress energy of the $3D_1$ state very nearly coincides with the predicted energy of the 3S state of the yellow series based on a quantum defect calculation.[41] It is difficult, however, to understand why only one of the excited states should conform to the theory.

It is useful to examine the deformation potentials that are derived from the analysis of the preceding section. The parameters obtained there are related to the deformation potentials a, b, and d of Eqs. 3-51 and 3-54. The results, obtained from the measured elastic compliance constants,[77] are given in Table 6-1 for two values of Δ'. Also shown are the deformation potentials for CuCl.[78] Cu_2O and CuCl should have comparable deformation potentials since the crystal structures are similar. It is seen that the agreement is better for the case $\Delta' = 600\ cm^{-1}$.

The limitations of the effective Hamiltonian formalism bear repeating. It was pointed out earlier that the calculation has involved only two exciton series (derived from the lowest conduction band and the two highest valence bands). Interactions with other series have been ignored. Also, the effective Hamiltonian treats yellow and green exciton states of a particular quantum state. Cho[60] has pointed out that the limit of applicability of this formalism may be reached if other exciton states happen to couple very strongly to the 12-fold exciton states treated in this way. Finally, there is a stress-dependent part of the spin-orbit interaction which has not been accounted for[44] although the effect is expected to be small.

BIBLIOGRAPHY

1. M. Hayashi and K. Katsuki, J. Phys. Soc. Jpn. 5,(1950).
2. M. Grossman, in Polarons and Excitons, edited by C. G. Kuper and C. D. Whitfield (Plenum, New York, 1963), p. 373.
3. M. Hayashi and K. Katsuki, J. Phys. Soc. Jpn. 7, 599 (1952).
4. E. F. Gross and N. A. Karryeff, Dokl. Adad. Nauk, SSR 84, 261 (1952).
5. E. F. Gross, Adv. Phys. Sci (USSR) 63, 782 (1957).
6. R. J. Elliott, Phys. Rev. 108, 1384 (1957).
7. E. F. Gross and A. A. Kaplyanskii, Sov. Phys. - Solid State 2, 353 (1960).
8. E. F. Gross and A. A. Kaplyanskii, Sov. Phys. - Solid State 2, 2637 (1961).
9. R. J. Elliott, Phys. Rev. 124, 340 (1961).
10. E. F. Gross, A. A. Kaplyanskii and V. T. Agekyan, Soc. Phys. - Solid State 4, 744 (1962).
11. E. F. Gross, Soc. Phys. Usp. 5, 195 (1962).
12. S. Nikitine, in Progress in Semiconductors edited by A. Gibson (John Wiley and Sons, Inc., New York, 1962) Vol. 6, p. 269.
13. S. Nikitine, J. B. Grun and M. Certier, Phys. Kondens. Mater. 1, 214 (1963).
14. R. J. Elliott, in Polarons and Excitons, edited by C. G. Kuper and C. D. Whitfield (Plenum, New York, 1963) p. 269.

15. V. T. Agekyan, E. F. Gross and A. A. Kaplyanskii, Sov. Phys. - Solid State 7, 623 (1965).

16. A. G. Zhilich, J. Halpern and B. P. Zakharchanya, Phys. Rev. 188, 1294 (1969).

17. S. Nikitine, in Optical Properties of Solids, edited by S. Nudelman and S. S. Mitra (Plenum, New York, 1969), p. 269.

18. W. S. Brower, Jr. and H. S. Parker, J. Cryst. Growth 8, 227 (1971).

19. J. L. Diess, A. Daunois and S. Nikitine, Solid State Commun. 9, 217 (1971).

20. J. L. Diess, A. Daunois and S. Nikitine, Phys. Status Solidi B47, 185 (1971).

21. A. Compaan and H. Z. Cummins, Phys. Rev. B6, 4753 (1972).

22. A. Daunois, J. C. Merle, J. L. Diess and S. Nikitine, Phys. Status Solidi B50, 691 (1972).

23. A. Daunois, J. L. Diess, J. C. Merle, C. Wecker and S. Nikitine, in Eleventh International Conference on the Physics of Semiconductors, Warsaw, 1972 (State Publishing House, Warsaw 1973), p. 1402.

24. V. A. Kiselev and A. G. Zhilich, Sov. Phys. - Solid State 13, 2008 (1972).

25. P. Y. Yu, Y. R. Shen, Y. Petroff and L. M. Falicov, Phys. Rev. Lett. 30, 283 (1973).

26. J. L. Birman, Solid State Commun. 13, 1189 (1973).

27. A. Compaan and H. Z. Cummins, Phys. Rev. Lett. 31, 41 (1973).

28. J. L. Diess and A. Daunois, Surf. Sci. 37, 804 (1973).

29. J. C. Merle, C. Wecker, A. Daunois, J. L. Diess and S. Nikitine, Surf. Sci. 37, 347 (1973).

30. V. T. Agekyan, B. S. Monozon and I. P. Shiryapov, Phys. Status Solidi B66, 359 (1974).

31. M. M. Denisov and V. P. Makarov, Optics Commun. 12, 105 (1974).

32. J. L. Birman, Phys. Rev. B9, 4518 (1974).

33. P. Y. Yu and Y. R. Shen, Phys. Rev. Lett. 32, 373 (1964).

34. F. I. Kreingold and V. L. Makarov, JETP Lett., 20, 201 (1974).

35. P. Y. Yu and Y. R. Shen, Phys. Rev. B12, 2488 (1975).

36. A. Z. Genack, H. Z. Cummins, M. A. Washington and A. Compaan, Phys. Rev. B12, 2478 (1975).

37. T. Itoh and S. Narita, J. Phys. Soc. Jpn. 39, 132(1975).

38. F. I. Kreingold and V. L. Makarov, Sov. Phys. - Semiconductors 8, 962 (1975).

39. J. C. Merle and M. Robino, Optics Commun. 14, 240 (1975).

40. V. T. Agekyan and Yu. A. Stepanov, Sov. Phys. - Solid State 17, 1041 (1975).

41. M. A. Washington, A. Z. Genack, H. Z. Cummins, R. H. Bruce, A. Compaan and R. A. Forman, Phys. Rev. B15, 2145 (1977).

42. V. T. Agekyan and T. I. Braulova, Sov. Phys. - Solid State 19, 599 (1977).

43. G. Kuwabara, M. Tanaka and H. Fukutani, Solid State Commun. 21, 599 (1977).

44. F. H. Pollak, Surf. Sci. 37, 863 (1973).

45. W. S. Brower, Jr. and H. S. Parker, J. Cryst. Growth 8, 227 (1971).

46. Cheng-Hsido Wu and J. L. Birman, Solid State Commun. 14, 465 (1974).

47. C. V. Raman and K. S. Krishman, Indian J. Phys. 2, 387 (1928).

48. G. Landsberg and L. Mandelstam, Naturwiss 16, 57 (1928).

49. R. Loudon, Proc. Royal Soc. (London) A 275, 218 (1963).

50. R. Loudon, Adv. Phys. 13, 423 (1964).

51. G. F. Koster, J. O. Dimmock, R. G. Wheeler and H. Statz, Properties of the Thirty-Two Point Groups (M.I.T. Press, Cambridge, Mass. 1963).

52. M. Cardona, in Modulation Spectroscopy, edited by F. Seitz, D. Turnbull and H. Ehrenreich (Academic Press, New York, 1969).

53. G. E. Pikus and G. L. Bir, Fiz. Tverd. Tela 1, 1642 (1959) Sov. Phys. - Solid State 1, 1502 (1959).

54. G. L. Bir and G. E. Pikus, Fiz. Tverd. Tela 3, 3050(1961). Sov. Phys. - Solid State 3, 2221 (1962) .

55. Michael Tinkham, Group Theory and Quantum Mechanics, (McGraw-Hill, New York, 1964).

56. O. Akimoto and H. Hasegawa, Phys. Rev. Lett. 20, 916 (1968).

57. T. Koda and D. W. Langer, Phys. Rev. Lett. 20, 50 (1968).

58. R. Berenson, unpublished.

59. K. Suzuki and J. C. Hensel, Phys. Rev. B9, 4184 (1974).

60. K. Cho, Phys. Rev. B14, 4463 (1976).

61. R. S. Knox, Theory of Excitons, Suppl. No. 5 of Solid State Physics (Academic Press, New York, 1963).

62. E. F. Gross, Sov. Phys. Usp. 5, 195 (1962).

63. R. W. Wyckoff, Crystal Structures (Interscience, New York, 1960) Vol. 1, p. 331.

64. P. Dawson, M. M. Hargreave and G. R. Wilkinson, J. Phys. Chem. Solids 34, 2201 (1973).

65. Y. Petroff, P. Y. Yu, and Y. R. Shen, Phys. Rev. B12, 2488 (1975).

66. M. M. Beg and S. M. Shapiro, Phys. Rev. B13, 1728(1976).

67. M. Washington, Doctoral thesis, N.Y.U. (1976).

68. J. P. Dahl and Switendick, J. Phys. Chem. Solids 27, 931 (1966).

69. C. Carabatos, Phys. Stat. Solidi 37, 773 (1970).

70. G. E. Pikus, Fiz. Tverd. Tela. 6, 324 (1964) Sov. Phys. - Solid State 6, 261 (1964) .

71. D. W. Langer, R. N. Euwema, K. Era and T. Koda, Phys. Rev. B2, 4005 (1970).

72. L. D. Laude, F. H. Pollak and M. Cardona, Phys. Rev. B3, 2623 (1971).

73. P. Y. Yu, Y. R. Shen, Y. Petroff, L. M. Falicov, Phys. Rev. Lett. 30, 283 (1973).

74. Peter Yu and Y. R. Shen, Phys. Rev. Lett. 32, 373(1974).

75. Peter Yu and Y. R. Shen, Phys. Rev. Lett. 32, 939(1974).

76. Peter Yu and Y. R. Shen, Phys. Rev. B12, 1377 (1975).

77. M.H. Manghani, W.S. Brower and H.S. Parker, Phys. Stat. Solidi (a) 25, 69 (1974)

78. T. Koda, T. Murahashi, T. Mitani, S. Sakoda, and Y. Onodera, Phys. Rev. B5, 705 (1972)